UNIVERSITÀ DEGLI STUDI DI BARI

DIPARTIMENTO INTERATENEO DI FISICA

"Michelangelo Merlin"

Corso di Laurea Magistrale in Fisica Teorica

AXION EMISSION AND DETECTION FROM A GALACTIC SUPERNOVA

Laureando: Pierluca CARENZA

Relatore: Prof. Alessandro MIRIZZI

Correlatore: Prof. Giampaolo CO'

ANNO ACCADEMICO 2017-2018

Introduction

The *SN 1987A* explosion was a milestone event in astroparticle physics. In particular, three hours before the visible light from SN 1987A reached the Earth, a neutrino burst was detected in three neutrino observatories: namely 11 neutrinos at Kamiokande II in Japan; 8 at Irvine-Michigan-Brookhaven in USA and 5 at Baksan in the Soviet Union. The neutrino burst lasted less than 13 s. These 24 events were the first (and until now unique) direct detection of supernova (SN) neutrinos and marked the birth of *neutrino astronomy*. Despite the exiguous number of events detected, neutrinos from SN 1987A were extremely useful to constrain neutrino properties (mass, charge, interactions). Furthermore, the detection of the neutrino burst was also important to constrain properties of *weakly interacting slim particles* (WISPs, with a mass $m <$ eV), which would be efficiently produced in the hot SN core, causing an additional energy loss that would have shortened the neutrino burst. Since SN 1987A neutrino data were roughly in agreement with theoretical predictions, strong bounds were placed on the properties of these exotic particles. One of the most studied WISP candidate studied in the context of the SN 1987A is the *axion*. This is an hypothetical particle postulated to solve a puzzle of Quantum Chromodynamics: the *strong CP problem*. Furthermore, it has been realized that axions are also good candidates for the *dark matter*. Thus their discovery is very desirable since it would allow one to "kill two birds with the same stone".

In this Thesis we will revise and improve the seminal works on axions done in the context of SN 1987A. In particular the main aim of this Thesis is to study the detectability of a SN axion signal in a future Mton-class water Cherenkov detector, such as the proposed Hyper-Kamiokande project in Japan. In this detector, the main detection channel for axions is the oxygen absorption. The oxygen de-excitation lead a gamma signal that would be potentially detectable. In order to estimate this signal, it is necessary to perform a re-evaluation of the axion-oxygen cross section estimated in a seminal paper of Engel *et al.* [Eng90]. This calculation based on advanced methods of nuclear physics is the main result of this Thesis.

The work is organized as follows:

In Chapter 1 we present an introduction to the axion models, experimental bounds and current searches on this particle. In Chapter 2 we revise the mechanism of SN explosion, discuss the expected neutrino signal and characterize the axion emissivity from a SN using the state-of-the-art SN simulations. In Chapter 3 we calculate the axion-oxygen absorption cross section using the Random Phase Approximation (RPA) technique. Then we evaluate the gamma branching ratio by means of a statistical method based on the SMARAGD Hauser-Feshbach reaction code. In Chapter 4 we characterize the axion signal in a Mton class Cherenkov detector and discuss its detectability. Finally, in Chapter 5 we summarize these results and give the conclusions.

Contents

Chapter 1

The strong CP problem and the axion

In this Chapter we introduce the *strong CP problem*, an unsolved puzzle of Quantum Chromodynamics (QCD), and its possible solution in terms of *axions* through the Peccei-Quinn mechanism. In this context, Section 1.1 deals with anomalies in Quantum Field Theory (QFT) following the Fujikawa's method [Kak93]. In Section 1.2 we use this concept to rigorously explain the strong CP problem. The Peccei-Quinn mechanism is presented in Section 1.3. This solution implies the existence of a new particle, the *axion*. In Section 1.4 we discuss the current constraints on the axion parameter space.

1.1 Anomalies in QFT

Let we consider a $SU(N)$ gauge theory of massless fermions described by the following Lagrangian

$$\mathcal{L} = i\bar{\Psi}(x)\not{D}\Psi(x) \; ; \tag{1.1}$$

where $D_\mu = \partial_\mu - igA_\mu$ is the usual covariant derivative, A_μ is the gauge field and $\not{D} = \gamma^\mu D_\mu$. This theory has an exact axial (or chiral) global symmetry

$$\begin{aligned} \Psi(x) &\to e^{\frac{i}{2}\theta\gamma^5}\Psi(x) \simeq \left(1 + \frac{i}{2}\theta\gamma^5\right)\Psi(x) \; ; \\ \bar{\Psi}(x) &\to \bar{\Psi}(x)e^{\frac{i}{2}\theta\gamma^5} \simeq \bar{\Psi}(x)\left(1 + \frac{i}{2}\theta\gamma^5\right) \; ; \end{aligned} \tag{1.2}$$

where θ is a constant. Although Eq. (1.2) is an exact symmetry of the classical theory, we will check whether Eq. (1.2) remains a symmetry after quantization. In a classical field theory the action determines the physics of the system considered. In QFT this role is played by the partition function

$$Z = \int D\bar{\Psi} D\Psi e^{i\int d^4x\,(\mathcal{L}+\bar{\Psi}\eta+\bar{\eta}\Psi)} \;. \tag{1.3}$$

We will compute the transformation of the partition function under Eq. (1.2) with a more general, possibly non constant, parameter $\theta(x)$. The action becomes

$$S = \int d^4x\,\bar{\Psi}(x) i\not{D}\Psi(x) \to S' = \int d^4x\,\bar{\Psi}(x) i\not{D}\Psi(x) + \frac{1}{2}\int d^4x\,\theta(x)\partial_\mu J_5^\mu(x) \;; \tag{1.4}$$

where

$$J_5^\mu(x) = \bar{\Psi}(x)\gamma^\mu\gamma^5\Psi(x) \;. \tag{1.5}$$

Varying $\theta(x)$ in Eq. (1.4) we have $\partial_\mu J_5^\mu = 0$, the classical conservation law arising from the Noether's theorem. In order to study how the functional measure changes, let we consider the eigenfunctions of the Dirac operator

$$\not{D}\psi_n(x) = \lambda_n \psi_n(x) \;; \tag{1.6}$$

without loss of generality we considered only discrete eigenvalues. The Dirac spinors can be decomposed as

$$\begin{aligned} \Psi(x) &= \sum_n a_n \psi_n(x) \;; \\ \bar{\Psi}(x) &= \sum_n \psi_n^\dagger(x) \bar{b}_n \;; \end{aligned} \tag{1.7}$$

with a_n and $\bar{b}_n$ constant coefficients (Grassmann numbers). The functional measure can be explicited as

$$D\bar{\Psi} D\Psi \to \prod_{nm} da_n d\bar{b}_n \;. \tag{1.8}$$

In this basis the transformation in Eq. (1.2) can be written as

$$e^{\frac{i}{2}\theta(x)\gamma^5}\Psi(x) \to \sum_n a'_n \psi_n(x) = e^{\frac{i}{2}\theta(x)\gamma^5}\sum_m a_m \psi_m(x) \;; \tag{1.9}$$

and using the orthonormality of the eigenfunctions

$$\begin{aligned} a'_n &= \sum_m C_{nm} a_m \;; \\ C_{nm} &= \int d^4x\,\psi_n^\dagger(x) e^{\frac{i}{2}\theta\gamma^5}\psi_m(x) \;. \end{aligned} \tag{1.10}$$

Therefore the functional measure changes as

$$\prod_m da'_m = \det(C_{nm})^{-1} \prod_n da_n \ . \tag{1.11}$$

For small $\theta(x)$, since $\det M = e^{\mathrm{tr}(\ln M)}$,

$$\begin{aligned} \det(C_{nm})^{-1} &= \det\left(\delta_{nm} + \frac{i}{2}\int d^4x\, \theta(x)\psi_n^\dagger \gamma^5 \psi_m(x)\right)^{-1} = \\ &= e^{-\frac{i}{2}\int d^4x\, \theta(x) A(x)} \ ; \end{aligned} \tag{1.12}$$

where

$$A(x) = \sum_n \psi_n^\dagger(x)\gamma^5\psi_n(x) \ . \tag{1.13}$$

Considering also an equal contribution from $D\bar{\Psi}$, the functional measure changes as

$$D\bar{\Psi}D\Psi \to e^{-i\int d^4x\, \theta(x)A(x)} D\bar{\Psi}D\Psi \ . \tag{1.14}$$

The integral in Eq. (1.14) is divergent under a global transformation and must be regularized. A possible regularization is obtained by inserting a term $\exp(-(\lambda_n/M)^2)$ and taking the limit $M \to \infty$:

$$\begin{aligned} A(x) &= \lim_{M\to\infty} \sum_n \psi_n^\dagger(x)\gamma^5 e^{-(\lambda_n/M)^2}\psi_n(x) = \\ &= \lim_{M\to\infty} \sum_n \psi_n^\dagger(x)\gamma^5 e^{-\left(\not{D}/M\right)^2}\psi_n(x) \ . \end{aligned} \tag{1.15}$$

We can perform a change of basis

$$\psi_n(x) = \langle x|n\rangle = \int \frac{d^4k}{(2\pi)^2} e^{-ikx}\langle k|n\rangle \ ; \tag{1.16}$$

and write the trace of a matrix $\mathcal{M}$ as

$$\begin{aligned} \mathrm{tr}(\mathcal{M}) &= \sum \psi_n^\dagger(x)\mathcal{M}(x)\psi_n(x) = \\ &= \sum_n \langle n|x\rangle \mathcal{M}(x)\langle x|n\rangle = \\ &= \sum_n \int \frac{d^4k}{(2\pi)^2}\frac{d^4k'}{(2\pi)^2} e^{ikx}\langle n|k\rangle \mathcal{M}(x) e^{-ik'x}\langle k'|n\rangle = \\ &= \int \frac{d^4k}{(2\pi)^4} e^{ikx}\mathcal{M}(x)e^{-ikx} \ . \end{aligned} \tag{1.17}$$

Using Eq. (1.15) and Eq. (1.17) we obtain that

$$\begin{aligned} A(x) &= \lim_{M\to\infty} \operatorname{tr} \int \frac{d^4k}{(2\pi)^4} e^{ikx} \gamma^5 e^{-\left(\not{D}/M\right)^2} e^{-ikx} = \\ &= \lim_{M\to\infty} \operatorname{tr} \int \frac{d^4k}{(2\pi)^4} e^{ikx} \gamma^5 e^{-\frac{1}{M^2}\left(-\frac{ig}{2}\gamma^\mu\gamma^\nu F_{\mu\nu} + D^2\right)} e^{-ikx} \ ; \end{aligned} \tag{1.18}$$

where $F_{\mu\nu} = \frac{i}{g}[D_\mu, D_\nu]$. The ∂^2 term diverges as

$$\int \frac{d^4k}{(2\pi)^4} e^{k^2/M^2} = \frac{iM^4}{16\pi^2} \ ; \tag{1.19}$$

then only the second order terms in the exponential contribute to the trace. From Eq. (1.18) we obtain

$$\begin{aligned} A(x) &= \lim_{M\to\infty} -\frac{g^2}{2!}\frac{1}{4M^4} \operatorname{tr} \gamma^5 (\gamma^\mu\gamma^\nu F_{\mu\nu})^2 \int \frac{d^4k}{(2\pi)^4} e^{k^2/M^2} = \\ &= \frac{g^2}{16\pi^2} \operatorname{tr} \tilde{F}^{\mu\nu} F_{\mu\nu} \ ; \end{aligned} \tag{1.20}$$

where

$$\tilde{F}^{\mu\nu} = \frac{1}{2}\epsilon^{\mu\nu\alpha\beta} F_{\alpha\beta} \ ; \tag{1.21}$$

is the dual field and we used

$$\operatorname{tr}(\gamma^5\gamma^\mu\gamma^\nu\gamma^\alpha\gamma^\beta) = 4i\epsilon^{\mu\nu\alpha\beta} \ ; \tag{1.22}$$

where $\epsilon^{\mu\nu\alpha\beta}$ is the Levi-Civita symbol. Using Eq. (1.4) and Eq. (1.20) we can calculate the variation of the partition function:

$$\begin{aligned} Z &= \int D\bar{\Psi} D\Psi e^{i\int d^4x\,\mathcal{L}} \to \\ & \qquad Z = \int D\bar{\Psi} D\Psi e^{i\int d^4x\,\mathcal{L}} e^{i\int d^4x\,\theta(x)\left(\partial_\mu J_5^\mu(x) - \frac{g^2}{16\pi^2}\operatorname{tr}\tilde{F}^{\mu\nu}F_{\mu\nu}\right)} \ . \end{aligned} \tag{1.23}$$

Varying $\theta(x)$ we arrive at the following constraint

$$\partial_\mu J_5^\mu = \frac{g^2}{16\pi^2} \operatorname{tr} \tilde{F}^{\mu\nu} F_{\mu\nu} \ . \tag{1.24}$$

The functional measure is modified by the transformation in Eq. (1.2), therefore the classical symmetry is lost. This phenomenon is called *anomaly.* One can prove that this non conservation of the axial current is given exactly by the "triangle diagram" [Pes95]

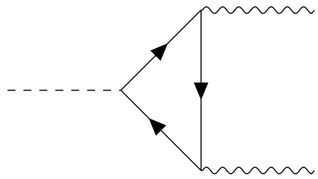

where the incoming line is a pseudoscalar, the loop is given by fermions and the outgoing lines are two gauge bosons. This diagram must be taken in account for the calculation of the decay rate of $\pi^0 \to \gamma\gamma$. Analyzing the Quantum Electrodynamics (QED) one can obtain some important and general results about anomalies. In this case Eq. (1.24) is written as [Pes95]

$$\partial_\mu J_5^\mu = \frac{e^2}{16\pi^2} \tilde{F}^{\mu\nu} F_{\mu\nu} = \frac{e^2}{8\pi^2} \partial_\mu (\epsilon^{\mu\nu\alpha\beta} A_\nu \partial_\alpha A_\beta) \ . \tag{1.25}$$

Eq. (1.25) shows that the anomaly can be written as a total divergence. Moreover, integrating over d^3x we can interpret the anomaly as a non conservation of the number of left minus right-handed fields [Pes95]:

$$\begin{aligned} \partial_0 (N_L - N_R) &= \frac{e^2}{4\pi^2} \int d^3x \, \mathbf{E} \cdot \mathbf{B} \ ; \\ N_L - N_R &= \int d^3x \, (\psi_L^\dagger \psi_L - \psi_R^\dagger \psi_R) \ . \end{aligned} \tag{1.26}$$

All this conclusions for QED are still valid in non-abelian gauge theories with slight modifications due to group factors.

1.2 The $U(1)_A$ problem

The QCD is a $SU(3)_c$ gauge theory described by the following Lagrangian [Kak93, Pes95]

$$\begin{aligned} \mathcal{L}_{QCD} &= \sum_a \bar{Q}_a (i\not{D} - m) Q_a - \frac{1}{2} \operatorname{tr} G^{\mu\nu} G_{\mu\nu} \ ; \\ Q_a &= \begin{pmatrix} q_{a,1} \\ q_{a,2} \\ q_{a,3} \end{pmatrix} \ ; \\ (D_\mu)_{ij} &= \delta_{ij} \partial_\mu - ig (A_\mu)_{ij} \ ; \\ A_\mu &= A_\mu^a \frac{\lambda^a}{2} \ ; \end{aligned} \tag{1.27}$$

where a is the flavor index, i and j are the colour indices and λ^a are the Gell-Mann matrices. At low energy, neglecting the masses of up and down quarks, the QCD Lagrangian [Eq. (1.27)] for these quarks has $SU(2)_V \otimes SU(2)_A \otimes U(1)_V \otimes U(1)_A$ as group of global symmetry in the flavor space. In fact the $SU(2)_V \otimes U(1)_V$ symmetry corresponds to the conservation of isospin and baryon number. This symmetry is more evident because of the occurrence of isospin multiplets in the hadrons spectrum. The other $SU(2)_A \otimes U(1)_A$ symmetry does not correspond to any multiplets. This absence can be explained via spontaneous symmetry breaking [Pec77a, Pec77b, Pec06]. In QCD quark-antiquark pairs have attractive interactions and the energy cost to create a pair is zero if they are massless. Therefore the vacuum will contain a quark-antiquark condensate with zero angular momentum and momentum [Pes95]:

$$\begin{aligned} &\langle \bar{q}^a_R q^b_L \rangle = -\Lambda^3_{\mathrm{QCD}} \delta^{ab} \; ; \\ &\Lambda_{\mathrm{QCD}} = 250\,\mathrm{MeV} \; . \end{aligned} \tag{1.28}$$

Λ_{QCD} is the scale of symmetry breaking: no bound states of quarks exist for energies above Λ_{QCD}.

This condensate mixes the two helicities, then quarks appear massive and the mass term breaks dynamically the $SU(2)_A \otimes U(1)_A$ symmetry. When a global continuous symmetry is spontaneously broken, a massless spin-0 field arises for each generator of the broken symmetry group. This is the Goldstone theorem and this scalar field is called Goldstone boson. For the $SU(2)_A \otimes U(1)_A$ symmetry, the Goldstone theorem predicts four massless particles. Three of them can be identified with pions, that are relatively light. Pions are odd-parity particles and correspond to the generators of $SU(2)_A$. Therefore they are created by the axial isospin current, and the matrix element of production can be parametrized as [Pes95]

$$\begin{aligned} \langle 0 | \bar{q} \gamma^\mu \gamma^5 \tau^a q | \pi^b(p) \rangle &= -i p^\mu f_\pi \delta^{ab} e^{-ipx} \; ; \\ q &= \begin{pmatrix} u \\ d \end{pmatrix} \; ; \end{aligned} \tag{1.29}$$

where

$$f_\pi = 93\,\mathrm{MeV} \; ;$$

is the pion decay constant.

The absence of the fourth light state forces us to conclude that $U(1)_A$ is not a true symmetry of QCD. The chiral anomaly in Eq. (1.24) seems to solve this problem. In fact under $U(1)_A$ global transformations the action is not invariant

$$
\begin{aligned}
S = \sum_b \int d^4x\, \bar{Q}_b(x) i\not{D} Q_b(x) \rightarrow \\
S' = \sum_b \int d^4x\, \bar{Q}_b(x) i\not{D} Q_b(x) + \theta \frac{g^2 N}{16\pi^2} \int d^4x \,\operatorname{tr} \tilde{G}^{\mu\nu} G_{\mu\nu} \;;
\end{aligned}
\tag{1.30}
$$

where N is the number of flavors [Eq. (1.25)]. At first sight Eq. (1.30) shows that $U(1)_A$ is not a symmetry of QCD, but the added term is the divergence of the so called Bardeen current [Eq. (1.25)] [Pec06]

$$
\begin{aligned}
&\operatorname{tr} \tilde{G}^{\mu\nu} G_{\mu\nu} = 4\partial_\mu K^\mu \;; \\
&K^\mu = \epsilon^{\mu\alpha\beta\gamma} \operatorname{tr} \left(\frac{1}{2} A_\alpha \partial_\beta A_\gamma - i\frac{g}{3} A_\alpha A_\beta A_\gamma \right) \;.
\end{aligned}
\tag{1.31}
$$

Then from Eq. (1.30)

$$
\delta S = \theta \frac{g^2 N}{4\pi^2} \int d^4x\, \partial_\mu K^\mu = \theta \frac{g^2 N}{4\pi^2} \int dS_\mu K^\mu \;; \tag{1.32}
$$

and using the simple boundary condition $A^\mu = 0$, one recovers that $U(1)_A$ is a symmetry. However, thanks to the gauge invariance, the boundary condition for vacuum configurations can be either $A^\mu = 0$ or $A^\mu = -i/g(\partial^\mu U)U^{-1}$, identifying different vacua. In general, every field configuration that approach asymptotically to different vacua is called *instanton*. We will study the $SU(2)$ QCD in the radiation gauge ($A_0^\mu = 0$) [Pec06]. The gauge transformation operators can have different boundary conditions:

$$
\lim_{\mathbf{r}\to\infty} U_n = e^{2\pi i n} \quad n \in \mathbb{Z} \;; \tag{1.33}
$$

where the number n, the *winding number*, is given by [Pec06]

$$
\begin{aligned}
n &= \frac{ig^3}{24\pi^2} \int d^3x\, \epsilon^{ijk} \operatorname{tr}(A_i A_j A_k) \;; \\
A_i &= -\frac{i}{g} (\partial_i U_n) U_n^{-1} \;.
\end{aligned}
\tag{1.34}
$$

In the radiation gauge, Eq. (1.34) is linked to the only non zero component of the Bardeen current

$$
\begin{aligned}
K^0 &= -i\frac{g}{3} \epsilon^{ijk} \operatorname{tr}(A_i A_j A_k) \;; \\
n &= -\frac{g^2}{8\pi^2} \int d^3x\, K^0 = \\
&= -\frac{g^2}{32\pi^2} \int d^4x \,\operatorname{tr}(\tilde{G}_{\mu\nu} G^{\mu\nu}) \;.
\end{aligned}
\tag{1.35}
$$

Therefore for some vacuum configurations the integral in Eq. (1.32) is non zero:

$$\delta S = \theta \frac{g^2 N}{4\pi^2} \int dS_0 K^0 = -2Nn \; ; \tag{1.36}$$

thus $U(1)_A$ is not a true symmetry of QCD. The vacua can be classified according to the winding number of the gauge fields therein, we will call them $|n\rangle$ n-vacua. The true vacuum is a superposition of this n-vacua

$$|\theta\rangle = \sum_n e^{-in\theta} |n\rangle \; ; \tag{1.37}$$

and it is called θ-vacuum. A transformation U_k generates a shift in the vacua:

$$\begin{aligned} U_k |n\rangle &= |n+k\rangle \; ; \\ U_1 |\theta\rangle &= e^{-i\theta} |\theta\rangle \; . \end{aligned} \tag{1.38}$$

The vacuum to vacuum amplitude will be

$$\begin{aligned} \langle n| e^{-iHt} |m\rangle &= \int DA_\mu e^{-i \int d^4x \, \mathcal{L}} \, \delta \left(\nu + \frac{g^2}{32\pi^2} \int d^4x \; \mathrm{tr} \, \tilde{G}_{\mu\nu} G^{\mu\nu} \right) \; ; \\ \nu &= n - m \; ; \end{aligned} \tag{1.39}$$

considering only field configurations with winding number ν that can account for the transition. The amplitude between two θ vacua contains a phase factor:

$$\begin{aligned} \langle \theta | e^{-iHt} |\theta\rangle &= \sum_{mn} e^{i(n-m)\theta} \langle n| e^{-iHt} |m\rangle = \\ &= \sum_\nu e^{i\nu\theta} \sum_m \langle m+\nu | e^{-iHt} |m\rangle = \\ &= \sum_\nu e^{i\nu\theta} \int DA_\mu e^{-i \int d^4x \, \mathcal{L}} \, \delta \left(\nu + \frac{g^2}{32\pi^2} \int d^4x \; \mathrm{tr} \, \tilde{G}_{\mu\nu} G^{\mu\nu} \right) \; . \end{aligned} \tag{1.40}$$

Therefore the effective QCD Lagrangian will be [Pec06]

$$\mathcal{L}_{\mathrm{eff}} = \mathcal{L}_{\mathrm{QCD}} - \theta_{\mathrm{QCD}} \frac{g^2}{32\pi^2} \, \mathrm{tr} \, \tilde{G}_{\mu\nu} G^{\mu\nu} \; ; \tag{1.41}$$

where we introduced the parameter θ_{QCD}. Eq. (1.41) states that the complex structure of the QCD vacuum can be seen as an extra self interaction of the gluon field. In general the quark mass matrix M is complex and non diagonal, but it can be made real and diagonal with a quark fields redefinition. The chiral transformation used to redefine quark fields, adds an extra term to the Lagrangian in Eq. (1.41) equivalent to the following shift [Pec06]

$$\theta_{\rm QCD} \to \bar{\theta}_{\rm QCD} = \theta_{\rm QCD} + \arg\det M \ . \tag{1.42}$$

The extra term in Eq. (1.41) violates CP. However, the measure of the neutron electric dipole moment puts a severe constraint on $\bar{\theta}_{\rm QCD}$ [Pat16]:

$$\begin{aligned} |d_n| &< 0.30 \times 10^{-25} e\,\mathrm{cm} \ ; \\ |\bar{\theta}_{\rm QCD}| &< 10^{-10} \ . \end{aligned} \tag{1.43}$$

This number is very small although it derives from two unrelated quantities [Eq. (1.42)]. Therefore its cancellation introduces a naturalness problem: the *strong CP problem.* Clearly it might be possible that for anthropic reasons $\bar{\theta}_{\rm QCD}$ has a so small value, but it is an unsatisfactory explanation and a Universe where CP is strongly violated also seems to be habitable. Maybe CP is spontaneously broken, but experiments support an explicit violation of CP [Pec06].

1.3 Axions

The most elegant solution to the strong CP problem, given by Peccei and Quinn [Pec77a, Pec77b, Wei78, Wil78], is to postulate a new extra symmetry group: $U(1)_{\rm PQ}$. This is an axial global symmetry, then it must be anomalous. Furthermore this symmetry must be spontaneously broken because we do not experience it. The Goldstone boson of the theory is called *axion*, a pseudoscalar. Under a $U(1)_{\rm PQ}$ transformation with parameter α, the axion field transforms as

$$a(x) \to a(x) + \alpha f_a \ ;$$

where f_a is the scale of spontaneous symmetry breaking. The Standard Model (SM) Lagrangian will become [Pec77a, Pec77b]

$$\begin{aligned} \mathcal{L}_{\rm tot} = \mathcal{L}_{\rm SM} + \bar{\theta}_{\rm QCD} \frac{g^2}{32\pi^2} \tilde{G}^a_{\mu\nu} G^{\mu\nu a} - \frac{1}{2}\partial_\mu a \partial^\mu a + \\ + \mathcal{L}_{\rm int}[a, \Psi] + \xi \frac{a}{f_a} \frac{g^2}{32\pi^2} \tilde{G}^a_{\mu\nu} G^{\mu\nu a} + \xi_\gamma \frac{a}{f_a} \frac{e^2}{16\pi^2} \tilde{F}_{\mu\nu} F^{\mu\nu} \ ; \end{aligned} \tag{1.44}$$

where $\mathcal{L}_{\rm SM}$ is the SM Lagrangian, $G^a_{\mu\nu}$ is the gluon field strenght tensor, $F_{\mu\nu}$ is the photon field strenght tensor, ξ and ξ_γ are the axion-gluon and axion-photon coupling constants, $\mathcal{L}_{\rm int}[a, \Psi]$ is an axion-fermion interaction term and the last two terms ensure the anomaly of the PQ current given by strong and electromagnetic interactions:

$$\partial_\mu J^\mu_{\mathrm{PQ}} = \xi \frac{g^2}{32\pi^2} \tilde{G}^a_{\mu\nu} G^{\mu\nu a} + \xi_\gamma \frac{e^2}{16\pi^2} \tilde{F}_{\mu\nu} F^{\mu\nu} \ . \tag{1.45}$$

Axions couple to photons and gluons through these anomaly induced interaction terms

$$\mathcal{L}_{a\gamma} = -\frac{g_{a\gamma}}{4} a \ F_{\mu\nu} \tilde{F}^{\mu\nu} = g_{a\gamma} a \ \mathbf{E} \cdot \mathbf{B} \ ; \tag{1.46}$$

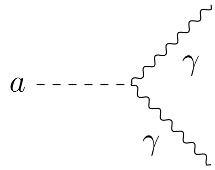

$$\mathcal{L}_{ag} = -\frac{1}{4} g_{ag} a \ \tilde{G}^a_{\mu\nu} G^{\mu\nu a} \ . \tag{1.47}$$

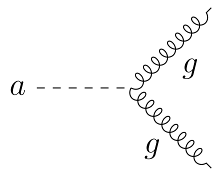

This effective potential has a minimum when

$$\left. \frac{\partial V_{\mathrm{eff}}}{\partial a} \right|_{a_0} = -\frac{\xi}{f_a} \frac{g^2}{32\pi^2} \tilde{G}^a_{\mu\nu} G^{\mu\nu a} \Big|_{a_0} = 0 \ . \tag{1.48}$$

This condition gives $a_0 = -\bar{\theta}_{\mathrm{QCD}} f_a / \xi$. The Lagrangian written in terms of the physical field $a_{\mathrm{phys}} = a - a_0$ has no more a CP violating term. This cancellation solves the strong CP problem: the CP odd term is driven to zero by the axion field dynamics [Pec06]. The axion-gluon interaction generates a mass term for the axion field and allows the mixing of π^0 and a as shown in Fig. (1.1). Axions pick up an effective mass approximately given by [Raf96]

$$m_a f_a \approx m_\pi f_\pi \ ;$$

that arises from the expansion around the minimum of the gluon-axion interaction potential.

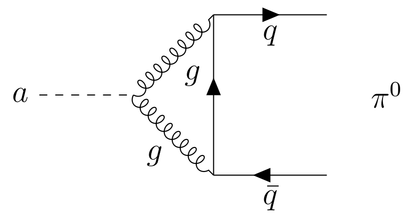

Figure 1.1: $a - \pi^0$ mixing.

1.3.1 Axion models

Here we present some of the possible axion models.

Peccei-Quinn-Weinberg-Wilczek model (PQWW)

In the PQWW model [Pec77b, Pec77a, Wei78, Wil78] the axion degree of freedom is hidden in the Higgs field. This model introduces an extra Higgs doublet, H_u, to the SM Higgs, H_d: one gives mass to u-type and the other to d-type quarks. Lepton masses are given by one of these fields, or by a third Higgs field. The interaction Lagrangian

$$\begin{aligned} &\mathcal{L} = -G_u \bar{Q}_L H_u u_R - G_d \bar{Q}_L H_d d_R - G_l \bar{L}_L H_d e_R \ ; \\ &Q_L = \begin{pmatrix} u_L \\ d_L \end{pmatrix} \ ; \\ &L_L = \begin{pmatrix} \nu_L \\ e_L \end{pmatrix} \ ; \end{aligned} \tag{1.49}$$

must be $U(1)_{\mathrm{PQ}}$ invariant. This condition fixes the $U(1)_{\mathrm{PQ}}$ charges of the fermion fields. Both the Higgs fields have a symmetry breaking potential

$$V(H_u, H_d) = \frac{\lambda_u}{4}\left(|H_u|^2 - \frac{v_u^2}{2}\right)^2 + \frac{\lambda_d}{4}\left(|H_d|^2 - \frac{v_d^2}{2}\right)^2 \ ; \tag{1.50}$$

where the two $U(1)$ symmetries, one for each Higgs doublet, represent the hypercharge and the PQ symmetry. After the symmetry breaking, the two Higgs fields take the values

$$\begin{aligned} &H_u = \frac{v_u}{\sqrt{2}} \begin{pmatrix} 1 \\ 0 \end{pmatrix} e^{iax/v} \ ; \\ &H_d = \frac{v_d}{\sqrt{2}} \begin{pmatrix} 0 \\ 1 \end{pmatrix} e^{ia/xv} \ ; \\ &x = \frac{v_u}{v_d} \ ; \\ &v = \sqrt{v_u^2 + v_d^2} \ . \end{aligned} \tag{1.51}$$

Then the Lagrangian becomes

$$\mathcal{L} = -G_u \frac{v_u}{\sqrt{2}} e^{iax/v} \bar{u}_L u_R - G_d \frac{v_d}{\sqrt{2}} e^{ia/xv} \bar{d}_L d_R - G_l \frac{v_d}{\sqrt{2}} e^{ia/xv} \bar{e}_L e_R \, . \tag{1.52}$$

Expanding the exponentials we can see that the axion couplings to SM particles are suppressed by a factor m/v. The Peccei-Quinn scale is close to the electroweak scale because it is connected to the u-type quarks masses. However, high energy experiments exclude models with a Peccei-Quinn scale near the electroweak scale [Kim86]. In fact the Yukawa coupling of axions with quarks allows the decay of K, J/Ψ and Υ meson to a lighter meson plus an axion. For instance, the decay $K^+ \to \pi^+ a$ is allowed by axion-π^0 oscillations.

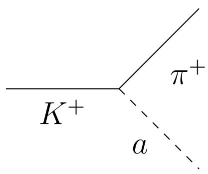

This decay is not observed giving a bound on g_{au} and g_{ad}, the axion-up and axion-down coupling constants [Kim86]

$$\begin{aligned} &\mathrm{BR}(K^+ \to \pi^+ a) < 3.8 \times 10^{-8} \, ; \\ &g_{au}^2, \, g_{ad}^2 < 4 \times 10^{-10} \, . \end{aligned} \tag{1.53}$$

Another possible decay is $J/\Psi \to \gamma a$, with a low background. The axion-charm coupling constant g_{ac} has the following bound [Kim86]

$$\begin{aligned} &\frac{\mathrm{BR}(J/\Psi \to \gamma a)}{\mathrm{BR}(J/\Psi \to \mu^+ \mu^-)} = \frac{g_{ac}^2}{2\pi\alpha} \, ; \\ &g_{ac}^2 < 10^{-6} \, . \end{aligned} \tag{1.54}$$

A similar limit can be extracted from $\Upsilon \to \gamma a$ for the axion-bottom coupling constant g_{ab} and gives [Kim86]

$$g_{ab}^2 < 10^{-4} \, . \tag{1.55}$$

The connection between the values of f_a and g_{aq}, where q is the quark flavor, is model dependent. However, neglecting the model dependent factors, $g_{aq} \sim \mathrm{GeV}/f_a$. Therefore the PQWW model, in which $f_a \sim 100\,\mathrm{GeV}$, is surely ruled out. This type of experiments can only probe a limited energy range near the electroweak scale. When f_a is high enough, the production rates and the detection probabilities fall down, making impossible to test axions with high energy experiments. The only viable models, in which $f_a \gg v$, are called *invisible axion models*. This new energy scale gives very light, weakly interacting and long-lived axions.

1.3.2 Invisible axion models

Kim-Shifman-Vainshtein-Zakharov model (KSVZ)

This model [Shi80] needs a heavy quark doublet, Q, that is a $SU(3)_c$ singlet. The scalar field φ, unlike the previous model, is a SM singlet that gives mass only to the heavy quark:

$$
\begin{aligned}
\mathcal{L} &= -G_Q \varphi \bar{Q}_L Q_R \ ; \\
Q &= \begin{pmatrix} Q_L \\ Q_R \end{pmatrix} \ ;
\end{aligned}
\tag{1.56}
$$

to make this term invariant, φ has charge two. Explicitly

$$
\begin{aligned}
\varphi &\to e^{i\alpha}\varphi \ ; \\
Q &\to e^{-i\gamma^5 \frac{\alpha}{2}} Q \ ;
\end{aligned}
\tag{1.57}
$$

and this symmetry ensures the absence of a mass term for the heavy quark. The usual symmetry breaking potential [Eq. (1.50)] has f_a as free parameter and we choose $f_a \gg v$. After the symmetry breaking,

$$
\varphi \to \frac{f_a}{\sqrt{2}} e^{i\frac{a}{f_a}} \ ; \tag{1.58}
$$

and the heavy quark gets a very large mass term

$$
\mathcal{L} = -G_Q \frac{f_a}{\sqrt{2}} e^{i\frac{a}{f_a}} \bar{Q}_L Q_R \ . \tag{1.59}
$$

The pseudoscalar field a, the axion field, interacts with heavy quarks with the interaction in Eq. (1.59) and with SM particles via the anomaly induced interactions. The mass of the heavy quark doublet is $m_Q \simeq G_Q f_a$. Since the quark doublet is very massive, at low energy the only important interaction is with two gluons and two photons. In this model axions do not interact with SM fermions at the tree level and the two gluons vertex makes possible an interaction with hadrons at the loop level, therefore these axions are called *hadronic axions*.

Dine-Fischler-Srednicki-Zhitnitsky model (DFSZ)

The DFSZ axion [Din81] requires a Higgs sector formed by two Higgs doublet H_u and H_d similar to the PQWW model. There is also a complex scalar SM singlet φ. The interaction Lagrangian is

$$
\mathcal{L} = -\lambda_H \varphi^2 H_u H_d \ ; \tag{1.60}
$$

invariant for opposite charges of φ and $H_{u/d}$. The observed SM Higgs forces λ_H to be small enough to have a Higgs boson with a mass of 125 GeV. The Higgs fields couple also to the SM fermions with the usual Yukawa coupling. At low energy the fermions kinetic term generates a coupling between fermions and axions at the tree level

$$\bar{q}\not{D}q \to \frac{C_f}{2f_a}\bar{q}\gamma^\mu\gamma_5 q\partial_\mu a \ . \tag{1.61}$$

1.4 Axion bounds

Axion parameter space can be constrained by three classes of arguments summarized in Fig. (1.2):

- Cosmological,
- Astrophysical,
- Laboratory experiments.

Axions can behave as cold or hot dark matter depending on the value of the Peccei-Quinn scale. If $f_a < 1.2 \times 10^{12}$ GeV, axions interact strongly enough to be thermally produced in the hot primordial plasma. Sufficiently strong interacting axions ($f_a < 3 \times 10^7$ GeV, $m_a > 0.2$ eV) decouple after the QCD phase transition at $T \approx 250$ MeV. In this case, the most relevant interaction processes for axions involve hadrons rather than quarks and gluons, relevant at earlier epochs. Then, there would be a background of low mass ($m_a \sim$ eV) hot relic axions. Analogously to neutrinos, axions hot dark matter would suppress small scale structures in the Universe. Latest cosmological analysis give $m_a < 0.67$ eV [Arc13] [Fig. (1.2)]. Conversely, if $f_a > 1.2 \times 10^{12}$ GeV axions interact so feebly with matter that they never reach thermal equilibrium. In this case they can be efficiently produced only by non-thermal mechanisms as topological defect decay and misalignment production. Depending on the production mechanism, axions with $10\,\mu\text{eV} < m_a < 100\,\mu\text{eV}$ [Arc13] would provide the cold dark matter.

Besides these bounds, the majority of experiments exploits the axion-photon interaction, a common feature of all axion models. Since this interaction is almost model independent, the axion parameter space can be enlarged without imposing any relation between $g_{a\gamma}$ and m_a [Fig. (1.3)]. Particles with an interaction Lagrangian as Eq. (1.46) and unrelated $g_{a\gamma}$ and m_a are called *axion-like* particles (ALPs), to distinguish them from QCD axions. ALPs appear in many SM extensions, as String Theory, and can be used to probe very

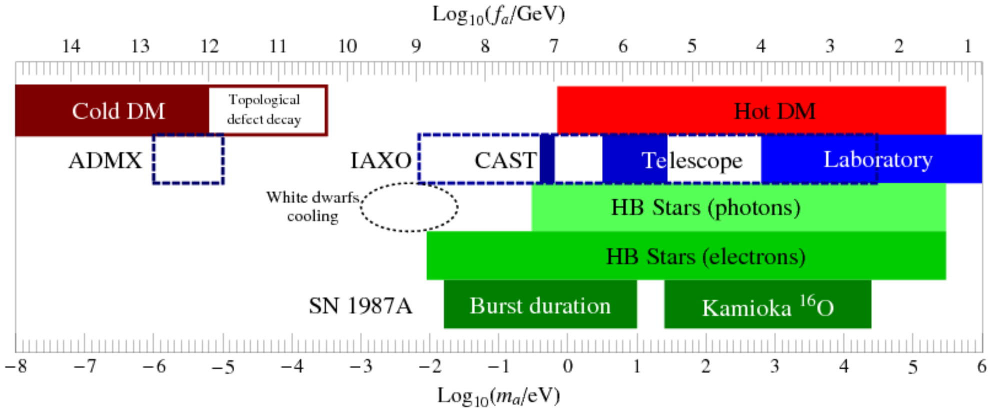

Figure 1.2: Constraints and searches on QCD axions. The red and brown bounds are given by cosmological considerations on hot and cold dark matter respectively. The blue bounds refer to direct detection experiments. The sensitivity of future experiments is represented in the blue dotted boxes. The light green zones are excluded by the energy loss of horizontal branch stars in globular clusters. The dark green zones are excluded by the analysis of the neutrino signal from SN 1987A.

high energy scale. The ALP-photon interaction is given by the Lagrangian in Eq. (1.46), which contains the model dependent coupling constant

$$g_{a\gamma} = \left(0.203(3)\frac{E}{N} - 0.39(1)\right)\frac{m_a}{\mathrm{GeV}^2}\ ; \tag{1.62}$$

where E and N are the electromagnetic and color anomalies. For DFSZ axions, $E/N = 8/3$ and for KSVZ axions, $E/N = 0$ if the electric charge of the heavy quark is zero. The yellow region in Fig. (1.3) is the QCD axion parameter space, which is not a line because of the differences between various models as DFSZ and KSVZ. Axion-photon coupling allows to obtain constraints on the otherwise invisible axions. In particular two effects can be exploited. The two-photon coupling allows the conversion $a \leftrightarrow \gamma$ in an external electric or magnetic field by virtue of the process shown in Fig. (1.4).

This process was first proposed by Primakoff (1951) to study the $\pi^0 - \gamma$ coupling which is experimentally difficult to measure in free decays $\pi^0 \to \gamma\gamma$. In stars the Primakoff process allows for the production of low mass pseudoscalars in the microscopic electric fields of nuclei and electrons. In the other case of a macroscopic field, usually a large scale magnetic field, the momentum transfer is small, the interaction is coherent over a large distance, and the conversion is best viewed as an axion-photon oscillation phenomenon in analogy to neutrino flavor oscillations. In particular, photon-axion conversions in coherent large-scale macroscopic magnetic fields were

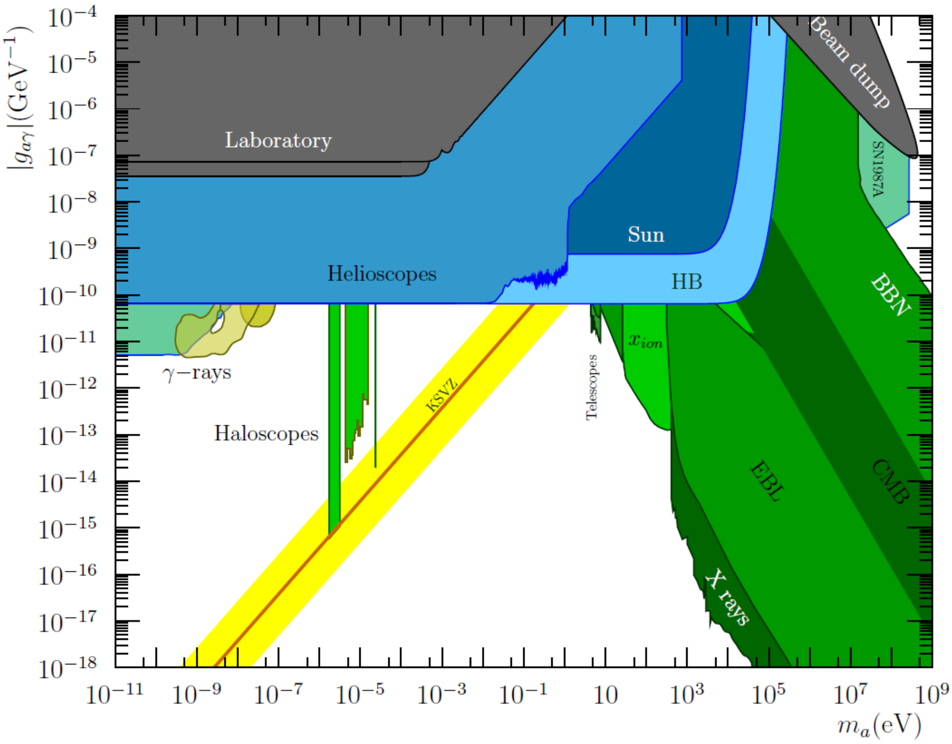

Figure 1.3: Parameter space for axion-like particles. The exclusion regions are described in the text. The yellow band is the QCD axion parameter space. (Figure taken from [Ira18]).

at the basis of two different experimental techniques to search for axions proposed by Pierre Sikivie in 1983 [Sik84]: haloscope and helioscope.

The haloscope technique searches for DM axions in the galactic halo through a microwave resonant cavity, where one can vary the cavity frequency until one matches the axion mass, getting a peak in the signal of the cavity.

Exploiting this effect, the Axion Dark Matter eXperiment (ADMX) tries to detect axions in the Milky Way dark matter halo. At the moment, the experiment excludes the mass range $1.9\,\mu\mathrm{eV} < m_a < 3.3\,\mu\mathrm{eV}$ for KSVZ axions [Fig. (1.2)] [Asz09].

ALPs and QCD axions are produced by Primakoff effect in the hot stellar plasma. Solar axion telescopes, the helioscopess, like SUMICO and CAST are built to detect solar axions by Primakoff effect, searching for the back conversions into X-rays into a magnet pointing towards the Sun. CAST gets the best experimental limits for low-mass ALPs, getting $g_{a\gamma} < 6.6 \times 10^{-11}\,\mathrm{GeV}^{-1}$ and $m_a < 0.02$ eV [Pat16]. Moreover, this experiment for the first time

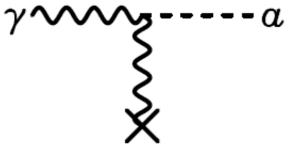

Figure 1.4: Primakoff $a \leftrightarrow \gamma$ conversion in an external electromagnetic field.

enters in the QCD axion parameter space region [Fig. (1.3)]. The future helioscope IAXO will explore the zone indicated in Fig. (1.2), improving the CAST bound with a sensitivity to $g_{a\gamma} \lesssim 10^{-12}\,\text{GeV}^{-1}$ [Ira11].

Using photon-ALP conversions, the "light shining through walls" experiments search whether photons pass an optical barrier thanks to photon-ALP oscillations in a magnetic field. The current best limit is given by the ALPS experiment at DESY which sets as limit $g_{a\gamma} < 3.5 \times 10^{-8}\,\text{GeV}^{-1}$ for $m_a < 0.3$ meV [Ehr10] [Fig. (1.3)]. Furthermore, the ALP-photon conversion might explain the observed hardening of TeV photons coming from very far sources. According to Standard physics, TeV photons should be absorbed by the cosmic microwave background radiation in pair production processes $\gamma\gamma \to e^+e^-$ and should not reach us. Conversely, different experiments have observed TeV photons coming from faraway sources. This transparency of the Universe might be an hint to the existence of ALPs in the range $m_a < 10^{-7}$ eV and $g_{a\gamma} \sim 10^{-12} - 10^{-10}\,\text{GeV}^{-1}$ [Dea11].

The analysis of a large number of stars can be used to test the presence of an additional energy loss channel caused by axions produced in Primakoff processes. In this context a useful probe is constituted by globular clusters, bound systems of stars with nearly the same age and differing only for their mass. Globular clusters can be used to estimate the duration of each stellar evolution phase. The additional energy loss channel can shorten the helium burning phase, the stars in the horizontal branch (HB) of the Hertzsprung-Russel diagram are in this phase. The globular clusters data give the bound $g_{a\gamma} < 6.6 \times 10^{-11}\,\text{GeV}^{-1}$ and $m_a < 1$ keV [Aya14].

Supernova explosions are another important tool to study ALPs and QCD axions. The neutrino burst detected from SN 1987A was roughly in agreement to standard SN models, showing no evidence of exotic energy loss channels associated with new particles [Raf96]. The presence of weakly interacting axions reduces the duration of the burst. Numerical simulations show that KSVZ axions with $f_a > 4 \times 10^8\,\text{GeV}$, in the free-streaming regime, do not shorten significantly the burst duration. However, also very strongly interacting axions would be trapped inside the SN core and would not modify the burst. Too strongly interacting axions are excluded because of the absence of an axion signal in the neutrino Cherenkov detector Kamiokande II. A small window around $f_a \sim 10^6\,\mathrm{GeV}$, called "hadronic axion window" was unconstrained by this consideration [Fig. (1.2)] [Raf96]. However, the cosmological bounds on hot dark matter close this small window left open by SN 1987A bounds.

Chapter 2

Axion emission from supernovae

In this Chapter we characterize the axion emission from supernovae (SNe). In Section 2.1 we explain the SN explosion mechanism. In Section 2.2 we characterize the expected neutrino burst from such an event. Section 2.3 is a review of the most important features of the SN neutrino signal from SN 1987A. In Section 2.4 we discuss the expected SN axion spectrum.

2.1 Supernova explosion

A star has its origin from a hot and dense cloud of gas bound by the gravity. Density and temperature grow up until the ignition of the nuclear fusion, which starts if the proto-star is massive enough ($M > 0.08 M_\odot$, where $M_\odot$ is the solar mass). As hydrogen is burnt producing helium, the energy released contrasts the gravitational collapse. The star reaches a stable configuration when the gravitational force and the radiation pressure compensate each other. For massive stars ($M > 8 M_\odot$) the nuclear fusion produces heavy elements in an "onion" structure with shells of burning elements, an expanded envelope and a degenerate iron core [Fig. (2.1)]. Iron in the core cannot be further burnt because it is the most stable nucleus and the only electron degeneracy pressure contrasts gravity. A typical iron core has a radius $R \sim 6000\,\mathrm{km}$ and a density $\rho \sim 10^{10}\,\mathrm{g\,/\,cm^3}$ [Mir16,Raf96]. The last star evolution stage is determined when the mass of the star core reaches the Chandrasekhar limit, $M \sim 1.4 M_\odot$, the maximum mass that can be supported by electron degeneracy pressure. At this point gravity is no more compensated and the core would unavoidably collapse. The collapse continues until density reaches $\rho \simeq 10^{14}\,\mathrm{g\,/\,cm^3}$, i.e. the nuclear density, and the radius becomes $R \sim 50\,\mathrm{km}$ [Mir16, Raf96]. Then the core becomes incompressible and the implosion is stopped, generating a shock wave reverting the implosion into an

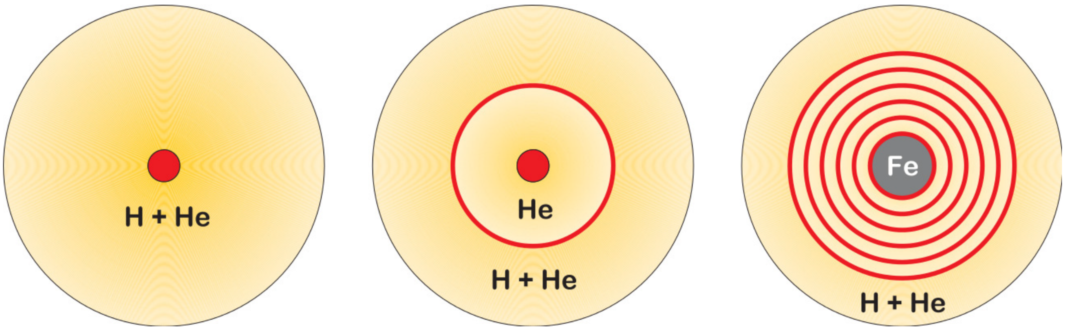

Figure 2.1: Different stages of the stellar evolution. Left: hydrogen fusion in the stellar core. Centre: helium burning phase. Right: shell structure of a massive star with an iron core and shells of lighter elements produced during the different phases of nuclear fusion.

explosion. Now we focus our attention on the detailed process of explosion of core collapse SNe. Simulations show that a core collapse SN explosion is divided into six phases as shown in Fig. (2.2) [Raf96]:

- *Initial phase of the collapse*: At the beginning of the collapse, the electron capture ($e^- p \to n\nu_e$) decreases the number of electrons per baryon converting electrons into neutrinos that escape freely. The electron captures reduce the electron degeneracy pressure producing neutron-rich nuclei. The lower degeneracy pressure accelerates the collapse and moves the heavier nuclei in the inner of the star, where they decay (via β decay) subtracting energy at the core.

- *Neutrino trapping*: When the nuclear matter in the core reaches a density $\rho \sim 10^{12}\,\mathrm{g}\,/\,\mathrm{cm}^3$, neutrinos are trapped because their diffusion time is larger than the collapse time. The inner part of the core, the "homologous core", collapses at a subsonic velocity because of the lower compressibility of nuclear matter. In the meantime the outer part experiences a supersonic collapse.

- *Bounce and shock formation*: The core collapse is decelerated when the core density is $\rho \sim 10^{14}\,\mathrm{g}\,/\,\mathrm{cm}^3$, the nuclear density. Since the outer layers continue to fall onto the inner core with supersonic velocity, a shock wave starts to propagate in the outer core. This bounce invertes the collapse in an explosion propagating from the interior to the outer mantle of the SN.

- *Shock propagation and ν_e burst*: Simulations show that the shock energy is not enough to generate the explosion and most of the energy is lost in the heavy nuclei dissociation. The increase in the number of free protons enhances the electron capture and the neutrinos produced in this way are trapped in a well defined zone, the "neutrinosphere". The total energy of this neutrino burst is $\sim 10^{51}$ erg.

- *Shock stagnation and ν heating*: After the bounce, the compact object at the center of the star grows thanks to the infalling material from the star. This is the proto-neutron star, that will become a neutron star if the mass is lower than $25M_{\odot}$, otherwise it becomes a black hole. Neutrinos need some seconds to escape the dense proto-neutron star and they deposit energy in the nuclear medium. The proto-neutron star emits neutrinos, relasing 99% of the total energy of the collapse in this form. Part of this energy is deposited in the weakened shock wave via $n\nu_e \rightarrow pe^-$ and $p\bar{\nu}_e \rightarrow ne^+$. This causes a revitalization of the shock wave.

- *Neutrino cooling and neutrino driven wind*: The core energy is lost via neutrino emission, producing all the three flavor neutrinos. The external layers expand and create a zone with low density and high temperature between the proto-neutron star and the shock-wave front. The high pressure in this zone restarts the explosion, that eventually end with a SN explosion.

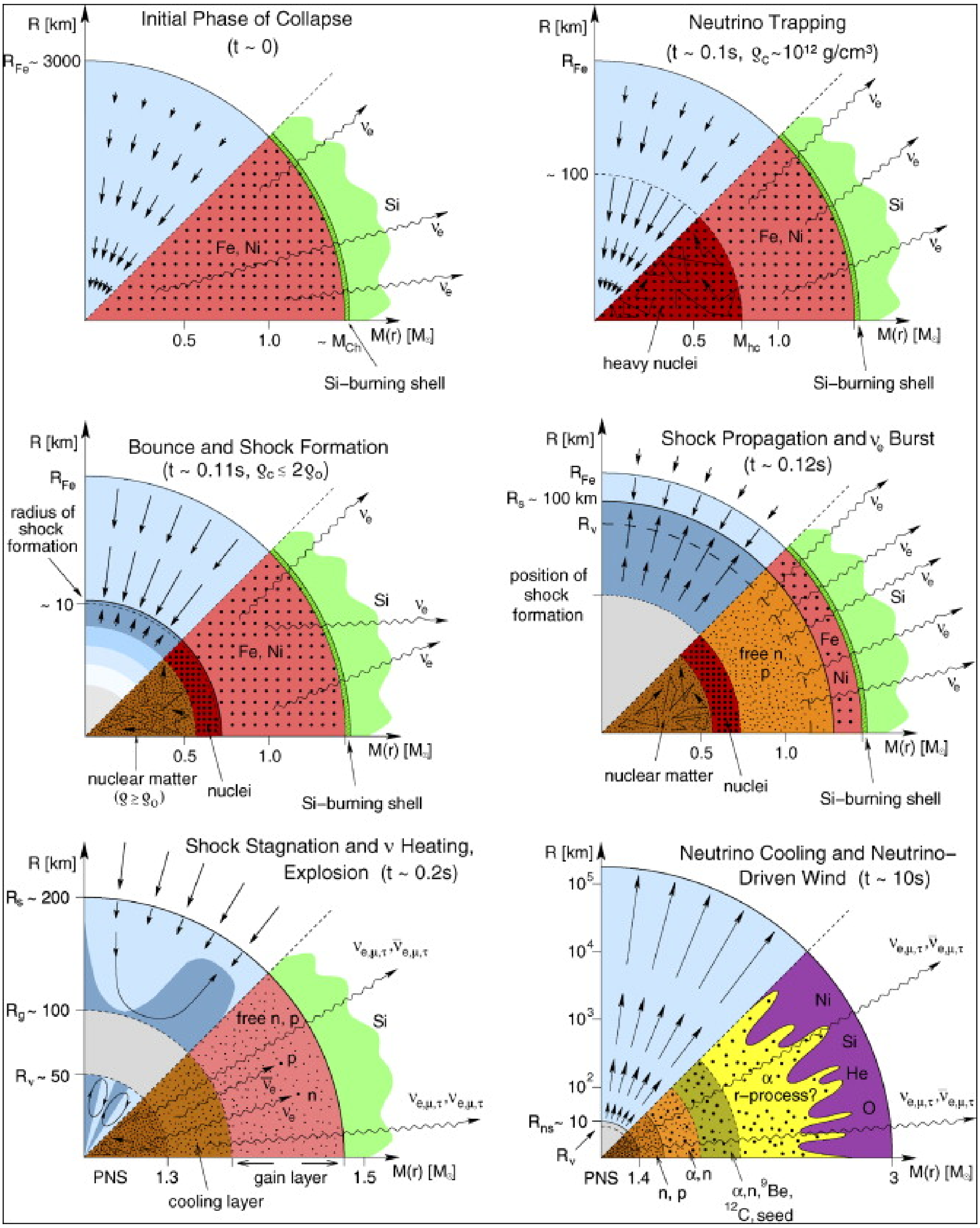

Figure 2.2: Scheme of the six phases of a core collapse SN.

2.2 Supernova neutrino signal

The main features of a SN neutrino burst can be understood with simple considerations [Raf96]. The energy carried away by neutrinos is approximately given by the binding energy of the proto-neutron star, approximating it with a sphere we obtain

$$E \approx \frac{3}{5}\frac{G_N M^2}{R} = 1.60 \times 10^{53}\,\mathrm{erg}\left(\frac{M}{M_\odot}\right)^2\left(\frac{10\,\mathrm{km}}{R}\right) . \qquad (2.1)$$

Neutrinos interact strongly enough to be trapped in the interior of the proto-neutron star, then in a simplified model they are emitted from a spherical surface, the “neutrinosphere”, with a radius of $10-20\,\mathrm{km}$ depending on the star and neutrinos properties. In the non-degenerate regime, matter near the proto-neutron star obeys the virial theorem:

$$2\langle E_{\mathrm{kin}}\rangle = -\langle U\rangle \approx \frac{G_N M}{R} m_N \; ; \qquad (2.2)$$

where m_N is the nucleon mass. The temperature can be computed using Eq. (2.2)

$$T = \frac{2}{3}\langle E_{\mathrm{kin}}\rangle \approx 17\,\mathrm{MeV} \; ; \qquad (2.3)$$

for $M = 1.4 M_\odot$ and $R = 15\,\mathrm{km}$. This simple estimate gives the order of magnitude of the neutrinosphere temperature.

The duration of the neutrino emission depends on the time that neutrinos need to escape the proto-neutron star and it is reasonable to take

$$\Delta t \approx \frac{R}{c}\frac{R}{\lambda} \; ; \qquad (2.4)$$

where R/c is the time to escape in absence of interactions and the interactions, parametrized by the mean free path $\lambda < R$, prolong this time. A typical neutrino-nucleon weak interaction cross section is $\sigma \sim 10^{-40}\,\mathrm{cm}^2$, taking a nucleon density $n \sim 10^{39}\,\mathrm{cm}^{-3}$, we obtain as mean free path [Vog01]

$$\lambda = \frac{1}{n\sigma} \sim 0.1\,\mathrm{m} \; ; \qquad (2.5)$$

and an emission time $\Delta t \sim O(10\,\mathrm{s})$ for $30\,\mathrm{MeV}$ neutrinos. These estimates can be improved considering that ν_e and $\bar{\nu}_e$ interact with matter via charged and neutral current interactions because they have an energy greater than the threshold for $\bar{\nu}_e p \to n e^+$ and $\nu_e n \to p e^-$. On the other hand, ν_μ and ν_τ do not have enough energy to produce respectively muons and tauons, then their interactions are only neutral current interactions, weaker than ν_e charged current interactions. This implies that ν_μ and ν_τ decouple in the inner of the star, at higher temperature. The mean energies are the following [Mir16, Raf96]:

$$\begin{aligned}
\langle E_{\nu_e} \rangle &= 10 - 12\,\mathrm{MeV} \ ; \\
\langle E_{\bar{\nu}_e} \rangle &= 12 - 15\,\mathrm{MeV} \ ; \\
\langle E_{\nu_x} \rangle &= 15 - 18\,\mathrm{MeV} \ ;
\end{aligned} \tag{2.6}$$

where $\nu_x \equiv \nu_\mu, \nu_\tau, \bar{\nu}_\mu, \bar{\nu}_\tau$ (sometimes will be important to distinguish between $\nu_x \equiv \nu_\mu, \nu_\tau$ and $\bar{\nu}_x \equiv \bar{\nu}_\mu, \bar{\nu}_\tau$). The difference between ν_e and $\bar{\nu}_e$ is due to their decoupling processes

$$\nu_e \; n \rightarrow p \; e^- \qquad \bar{\nu}_e \; p \rightarrow n \; e^+ \ .$$

Since there are fewer protons than neutrons, the anti-neutrinos decouple at higher temperature.

A SN can be roughly considered as a blackbody that cools via neutrino emission [Raf96]. Indeed, the neutrino energy distribution is well approximated with a quasi-thermal distribution with the temperature of the neutrinosphere. A simple parametrization of the neutrino energy distribution, based on numerical simulations is [Kei02, Mir05]

$$\begin{aligned}
f(E) &= \frac{(1+\alpha)^{1+\alpha}}{\Gamma(1+\alpha)\langle E \rangle} \left(\frac{E}{\langle E \rangle} \right)^{\alpha} \exp\left[-(1+\alpha)\frac{E}{\langle E \rangle} \right] \ ; \\
\frac{dN}{dE} &= \frac{L_0}{\langle E \rangle} f(E) \ ; \\
\alpha &= \frac{2\langle E \rangle^2 - \langle E^2 \rangle}{\langle E^2 \rangle - \langle E \rangle^2} \ ;
\end{aligned} \tag{2.7}$$

where L_0 is the time-integrated luminosity, α is a pinching parameter and for $\alpha = 2$ we recover the blackbody spectrum with a temperature $T = \langle E \rangle / 3$. This energy distribution [Fig. (2.3)], the mean energy [Fig. (2.4)] and the number of neutrinos emitted $N_0 = L_0 / \langle E \rangle$ [Fig. (2.5)] are obtained from a simulation of a $18 M_\odot$ SN.

This simulation developed by the "Wroclaw Supernova Project" [Fis] is based on a spherically symmetric core-collapse SN model, the AGILE-BOLTZTRAN model. The dynamics is determined by general relativistic neutrino radiation hydrodynamics with angle and energy-dependent three flavor Boltzmann neutrino transport.

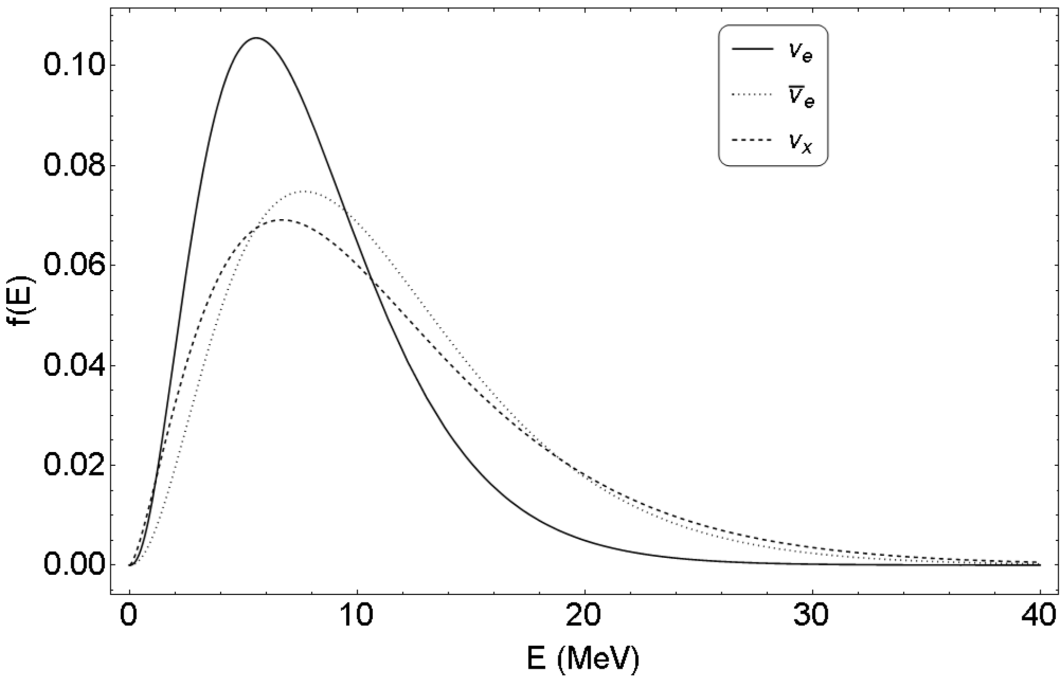

Figure 2.3: Neutrino energy distribution from numerical simulations of a $18M_{\odot}$ SN at post-bounce time $t = 1\,\mathrm{s}$. The three lines represents the different neutrino flavors as shown in the legend.

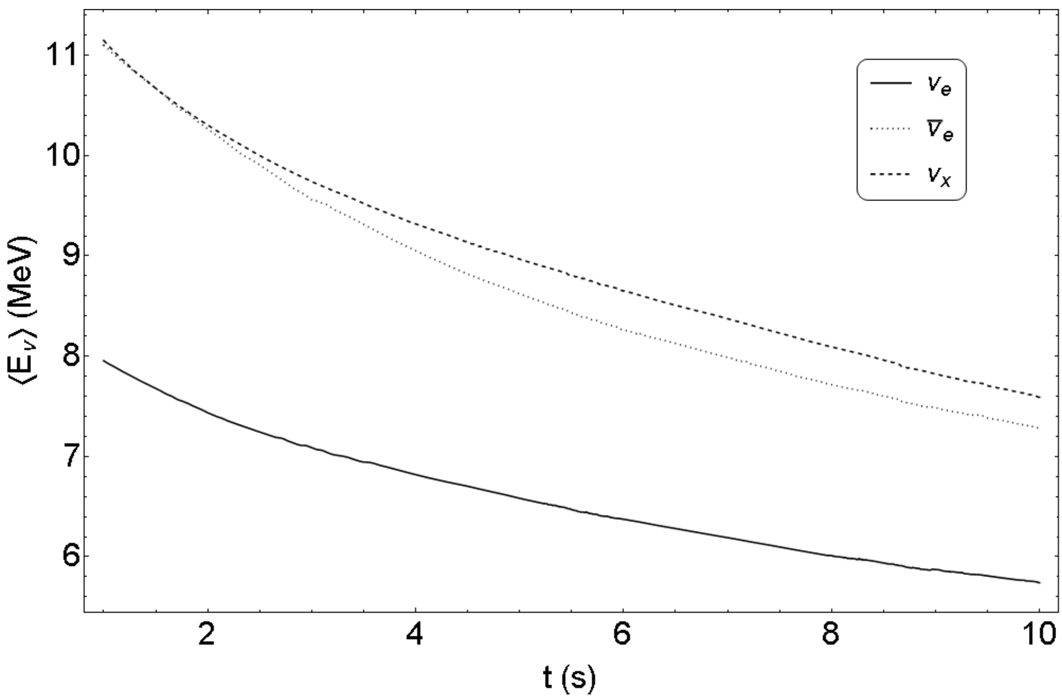

Figure 2.4: Neutrinos mean energy from numerical simulations of a $18M_{\odot}$ SN for $t > 0.5$ s. The three lines represents the different neutrino flavors as shown in the legend.

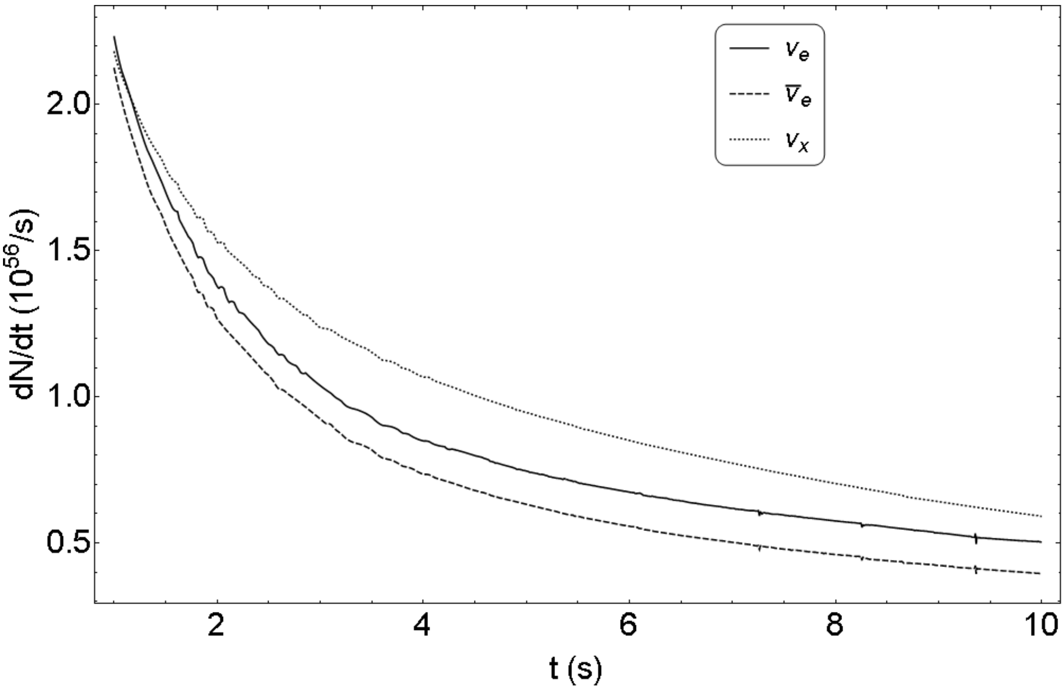

Figure 2.5: Number of neutrinos from numerical simulations of a $18M_\odot$ SN for $t > 0.5$ s. The three lines represents the different neutrino flavors as shown in the legend.

Table 2.1: Best fit parameters for the time-integrated neutrino fluxes in the time window $0.7 - 10\,\text{s}$.

Species	α	$\text{N}_0\,(\times 10^{56})$	$\langle E \rangle$
ν_e	2.08	8.42	6.91
$\overline{\nu}_e$	1.56	7.37	9.41
ν_x	1.33	9.76	9.38

In this Thesis we will be mostly interested in the cooling phase, where axion effects are more relevant. Therefore we integrate the neutrino fluxes in the time window $0.7-10\,\text{s}$. These can be fitted with Eq. (2.7) and time-independent parameters α, N_0 and $\langle E \rangle$ [Tab. (2.1)]. In Fig. (2.6) we show the time-integrated fluxes.

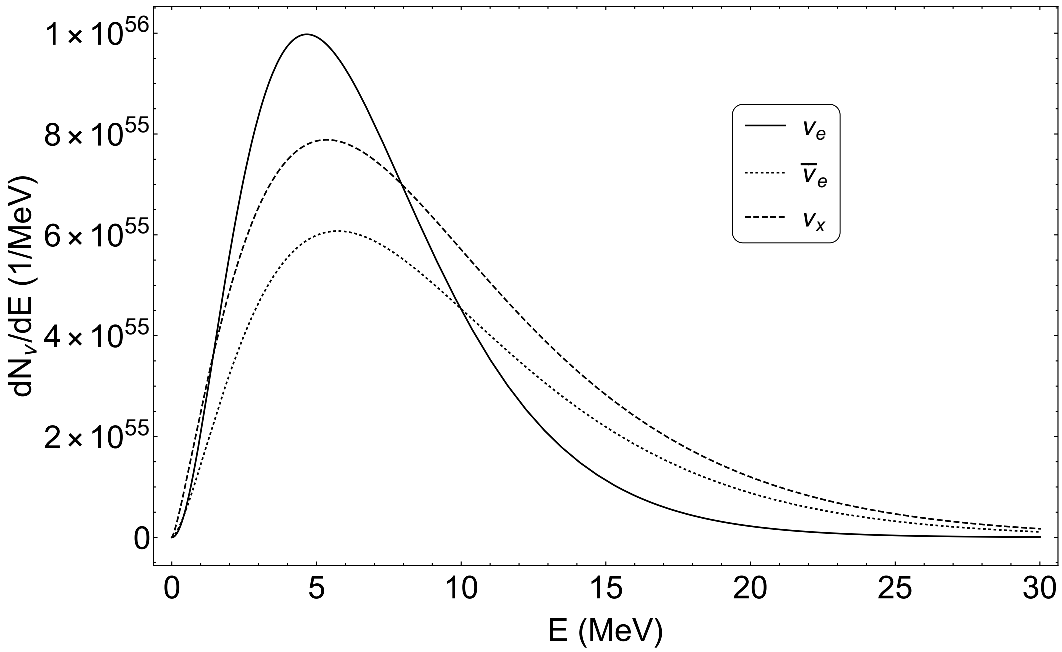

Figure 2.6: Time-integrated neutrino fluxes ($t \in [0.7; 10]\,\text{s}$).

2.3 SN 1987A neutrinos

Supernova neutrinos have been observed for the first and unique time from supernova SN 1987A in the Large Magellanic Cloud, a small satellite galaxy of the Milky Way at a distance of 51.4 kpc. This event was useful to test our knowledge about SNe and neutrinos. The SN 1987A progenitor was Sanduleak $-69^{\circ}202$, a blue supergiant with a mass of $\sim 20 M_{\odot}$. The neutrino burst of this SN was detected by different underground detectors on 23$^{\mathrm{th}}$ February 1987 [Fig. (2.7)] and the subsequent optical signal was seen three hours later. The most important detections came from the Kamiokande II (KII) water Cherenkov detector, originally planned to search for proton decay and the Irvine-Michigan-Brookhaven (IMB). In particular KII detected 11 events while IMB 8 events. A smaller number of events were detected also at Baksan Scintillator Telescope (BST). The detection channel of SN 1987A neutrinos was the inverse beta decay (IBD) $\bar{\nu}_e p \to n e^+$. SN 1987A confirmed that the gravitational binding energy is carried out by neutrinos with a characteristic energy of $\langle E \rangle \sim 10\,\mathrm{MeV}$. Moreover the neutrino burst duration, a few seconds, permits to estimate a neutrino luminosity of $L_\nu \sim 10^{52}\,\mathrm{erg}\,/\,\mathrm{s}$.

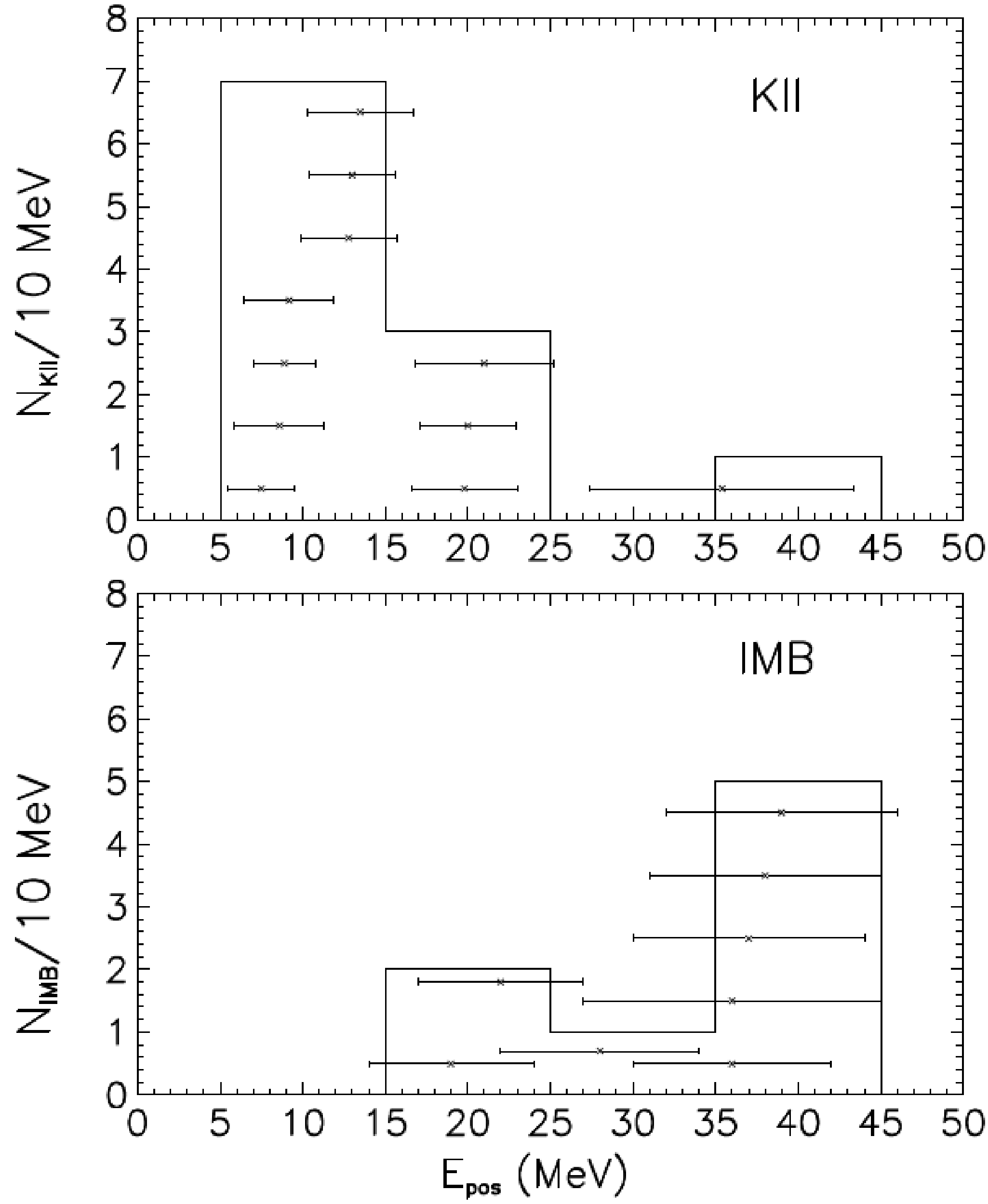

Figure 2.7: SN 1987A neutrino signal at KII and IMB.

2.4 Axion production

To study the impact of an additional energy loss channel given by axions, we have to calculate the axion production rate in a SN enviroment. The only relevant axion production process is the axion bremsstrahlung $NN \to NNa$. This process is induced by the axion-nucleon interaction, determined by the following Lagrangian [Raf96]

$$\mathcal{L}_{aN} = \sum_{i=p,n} \frac{C_i}{2f_a} \bar{\Psi}_i \gamma^\mu \gamma^5 \Psi_i \partial_\mu a \; ; \tag{2.8}$$

where C_i is the axion-nucleon coupling constant and Ψ_i is the nucleon spinor. At the lowest order, the nucleons exchange a pion, this is the One Pion Exchange (OPE) approximation.

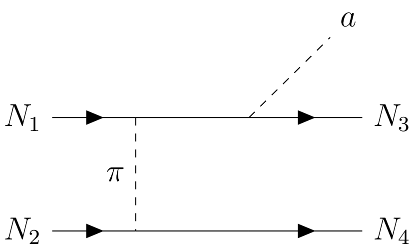

The pion-nucleus interaction Lagrangian is similar to the axion-nucleus one [Raf96]

$$\mathcal{L}_{\pi N} = 2m_N \frac{f_{ij}}{m_\pi} \bar{\Psi}_i \gamma^5 \Psi_j \pi \; ; \tag{2.9}$$

where m_N is the nucleon mass and m_π is the pion mass. Therefore, the matrix element of the nucleon bremsstrahlung can be computed using the Lagrangians in Eq. (2.8)-(2.9). The matrix element in the non-relativistic limit is [Raf96]

$$\begin{aligned}
&\sum_{s_f} |\mathcal{M}|^2 = \frac{16(4\pi)^3 \alpha_\pi^2 \alpha_a}{3m_N^2} \left[\left(\frac{\mathbf{k}^2}{\mathbf{k}^2 + m_\pi^2} \right)^2 \right. \\
&\left. \left(\frac{\mathbf{l}^2}{\mathbf{l}^2 + m_\pi^2} \right)^2 + \frac{\mathbf{k}^2 \mathbf{l}^2 - 3(\mathbf{k} \cdot \mathbf{l})^2}{(\mathbf{k}^2 + m_\pi^2)(\mathbf{l}^2 + m_\pi^2)} \right] \; ; \\
&\mathbf{k} = \mathbf{p}_2 - \mathbf{p}_4 \; ; \\
&\mathbf{l} = \mathbf{p}_2 - \mathbf{p}_3 \; ; \\
&\alpha_a = \left(\frac{C_N m_N}{f_a} \right)^2 \frac{1}{4\pi} \; ; \\
&\alpha_\pi \approx 15 \; .
\end{aligned} \tag{2.10}$$

The momentum-dependent part in the matrix element in Eq. (2.10) can be ignored introducing a small error. Therefore we obtain

$$\sum_{s_f} |\mathcal{M}|^2 = \frac{16(4\pi)^3 \alpha_\pi^2 \alpha_a}{3m_N^2} \,. \tag{2.11}$$

Axions modify the stellar energy-loss in different ways, depending on the axion-nucleon coupling. For instance, Fig. (2.8) shows that the neutrino burst duration could be reduced by axions. Only axions that interact too strongly or too feebly with matter do not affect the neutrino burst duration. Axions can be classified according to their interaction strength. Fig. (2.8) shows that axions with a coupling constant g_{aN} in the range $[10^{-11}, 10^{-8}]$ interact so weakly that freely escape from the star, stealing energy from SN core. As a consequence their emission would significantly reduce the duration of the neutrino burst since they carry out efficiently energy from the SN core. This means that axions in this regime, the free-streaming regime, have a strong impact on the stellar evolution. Axions with $g_{aN} > 10^{-7}$ are in the trapping regime. In this regime, axions cannot escape from the star and do not contribute to the energy-loss efficiently. However, in this case they would be emitted from an "axionsphere" (analogous to the neutrinosphere) as a burst and produce a possible signal in an underground detector.

In the rest of this Thesis we assume that $g_{aN} = C_N m_N / f_a$, where m_N is the nucleon mass and C_N, $N = n, p$ is a model-dependent factor. Furthermore, the trapping regime is characterized by $f_a = 10^6\,\mathrm{GeV}$ and then $g_{ap} = g_{an} = 10^{-6}$; the free-streaming regime is characterized by $g_{ap} = 9 \times 10^{-10}$ and $g_{an} = 0$.

2.4.1 Free-streaming regime

In the free-streaming regime axions interact weakly with matter and escape freely subtracting energy to the SN. In this regime axions are emitted from the whole SN volume. The energy-loss rate is obtained

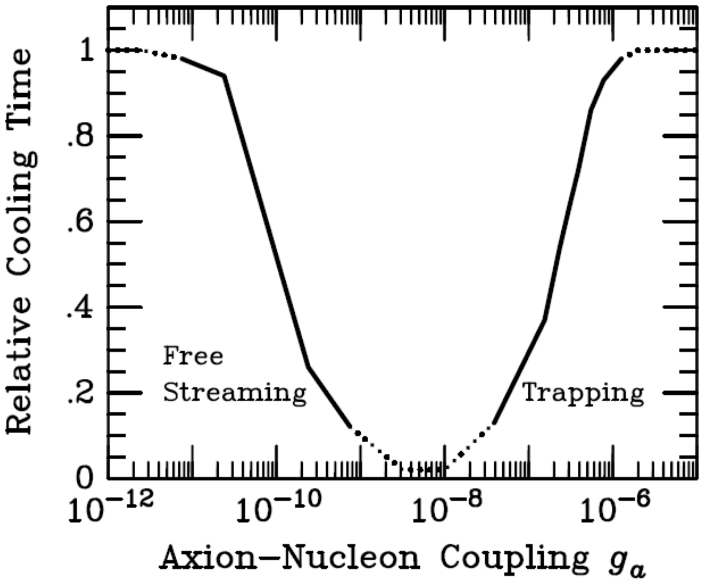

Figure 2.8: Duration of the neutrino burst as a function of the axion-nucleon coupling constant. (Figure taken from [Raf96]).

using the matrix element in Eq. (2.10) as shown in Appendix A.1-A.2:

$$\begin{aligned}
Q_a &= \frac{\alpha_a n_B \Gamma_\sigma T^3}{4\pi m_N^2}\int_0^{+\infty} dx\, x^2 s(x) e^{-x} \;; \\
\Gamma_\sigma &= 4\sqrt{\pi}\alpha_\pi^2 n_B T^{1/2} m_N^{-5/2} \;; \\
s(x) &= Y_n^2 C_n^2 [s_0(x) - s_{\mathbf{k}\cdot\mathbf{l}}(x)] + Y_p^2 C_p^2 [s_0(x) - s_{\mathbf{k}\cdot\mathbf{l}}(x)] + \\
&+ \frac{Y_n Y_p}{3}\left\{[7(C_n + C_p)^2 + 5(C_n - C_p)^2] s_0(x) + \right. \\
&\left. -[6(C_n + C_p)^2 + 2(C_n - C_p)^2] s_{\mathbf{k}\cdot\mathbf{l}}(x)\right\} \;;
\end{aligned} \tag{2.12}$$

where Y_p and Y_n are the nucleon number per baryon and

$$\begin{aligned}
s_0(x) &= \int_0^\infty dv\, e^{-v}\sqrt{v(x+v)} \;; \\
s_{\mathbf{k}\cdot\mathbf{l}}(x) &= \int_0^\infty dv\, e^{-v}\frac{x^2}{2(2v+x)}\ln\left(\frac{\sqrt{v+x}+\sqrt{v}}{\sqrt{v+x}-\sqrt{v}}\right) \;.
\end{aligned} \tag{2.13}$$

The electron number per baryon, Y_e, can be used to set $Y_p = Y_e$ and $Y_n = 1 - Y_e$. To simplify the calculations we need the following approximations that are accurate at the $15-20\%$

$$\begin{aligned} xe^{-x}s_0(x) &\simeq 1.4x^{1.25}e^{-x} \ ; \\ xe^{-x}s_{\mathbf{k}\cdot\mathbf{l}}(x) &\simeq 0.28x^{2.2}e^{-1.1x} \ ; \\ xe^{-x}[s_0(x)-s_{\mathbf{k}\cdot\mathbf{l}}(x)] &\simeq 1.15x^{1.05}e^{-1.05x} \ . \end{aligned} \tag{2.14}$$

We used a simulation of a perturbed $18M_\odot$ SN in presence of axions with $g_{ap}=9\times10^{-10}$ and $g_{an}=0$ [Fis]. Fig. (2.9)-(2.10) show the time evolution of the neutrino mean energy and neutrino emission rate. For the axion emission rate we obtain

$$\frac{dN_{\rm ax}}{dtdE}=\frac{C}{2T_{\rm eff}}g_{aN}^2\left(\frac{E}{T_{\rm eff}}\right)e^{-E/T_{\rm eff}} \ ; \tag{2.15}$$

where

$$\begin{aligned} C &= 6.864\times10^{83}t^{-6.93}e^{-17.53t^{-0.49}}\,\mathrm{s}^{-1} \ ; \\ T_{\rm eff} &= 2310\,e^{-4.3t^{0.273}}t^{1.353}\,\mathrm{MeV} \ ; \\ t &\in [0.5;15] \ . \end{aligned} \tag{2.16}$$

Fig. (2.11) shows the neutrino energy distribution in presence of free streaming axions. Fig. (2.12) shows the axion spectrum of Eq. (2.15).

The energy-loss rate [Eq. (2.12)] has the following dependence [Appendix A.2]:

$$\begin{aligned} Q_a \sim\ & (2.06Y_n^2+10.4Y_nY_p)C_n^2+(2.06Y_p^2+10.4Y_nY_p)C_p^2+ \\ & +0.625Y_nY_pC_nC_p \ ; \end{aligned} \tag{2.17}$$

that can be integrated over the stellar model. The time-integrated luminosity is

$$L\sim g_{an}^2+0.6g_{ap}^2+0.03g_{an}g_{ap} \ ; \tag{2.18}$$

and the number of emitted axions is

$$N\sim g_{an}^2+0.6g_{ap}^2+0.07g_{an}g_{ap} \ . \tag{2.19}$$

Eq. (2.17)-(2.19) are obtained using a SN model perturbed by axions interacting only with protons. However we expect that Eq. (2.17)-(2.19) do not depend from the axion model because axion interactions cannot change the nucleon abundance.

The neutrino and axion fluxes in this model of perturbed SN can be integrated from 0.7 s to 10 s and fitted with Eq. (2.7). In Fig. (2.13)-(2.14) we show the numerical time-integrated fluxes and the fit parameters are shown in Tab. (2.2).

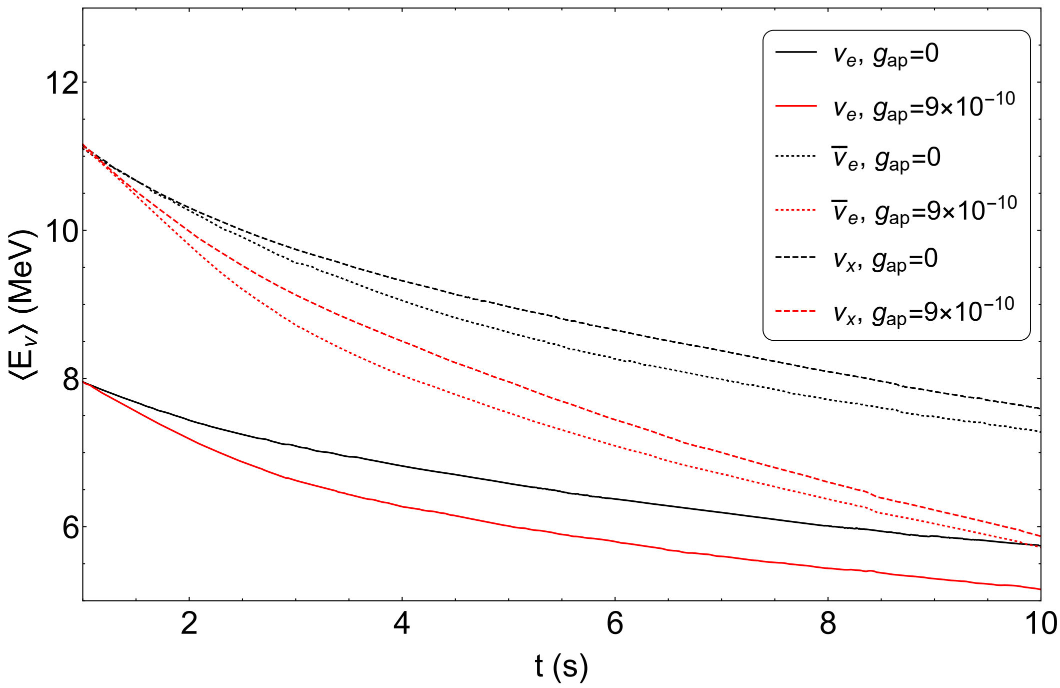

Figure 2.9: Time evolution of the neutrino mean energies. The axion couplings are $g_{ap} = g_{an} = 0$ (black lines) and $g_{ap} = 9 \times 10^{-10}$, $g_{an} = 0$ (red lines).

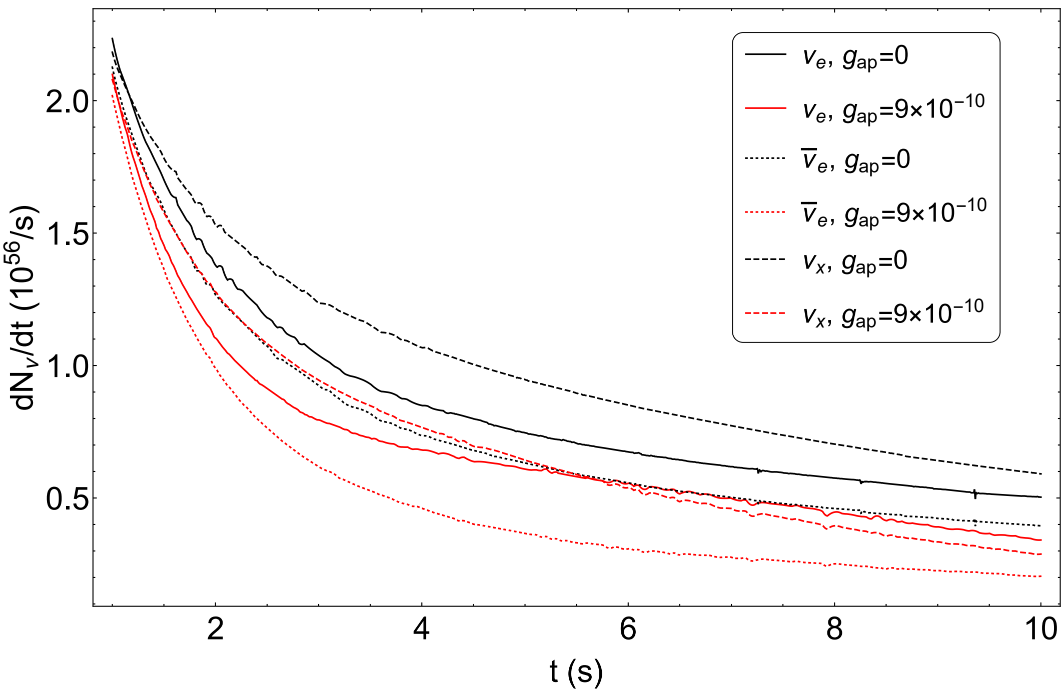

Figure 2.10: Time evolution of the neutrino emission rates. The axion couplings are $g_{ap} = g_{an} = 0$ (black lines) and $g_{ap} = 9 \times 10^{-10}$, $g_{an} = 0$ (red lines).

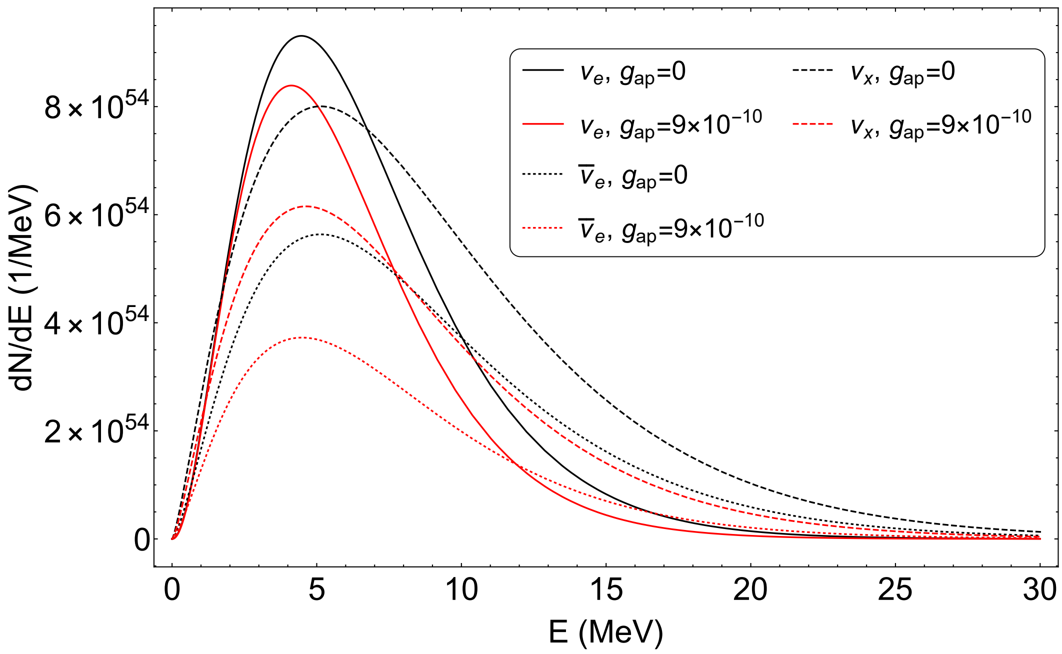

Figure 2.11: Neutrino energy distribution for $g_{ap} = g_{an} = 0$ (black lines) and $g_{ap} = 9 \times 10^{-10}$ and $g_{an} = 0$ (red lines) at post-bounce time $t = 5\,\mathrm{s}$.

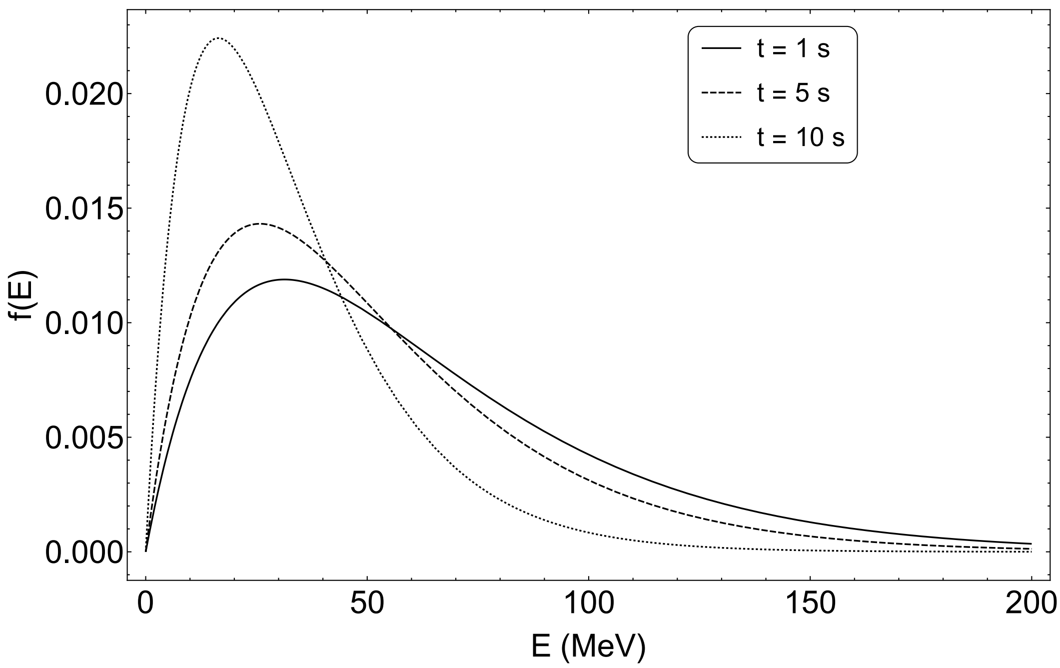

Figure 2.12: Axion energy distribution for $g_{ap} = 9 \times 10^{-10}$ and $g_{an} = 0$ at different post-bounce times.

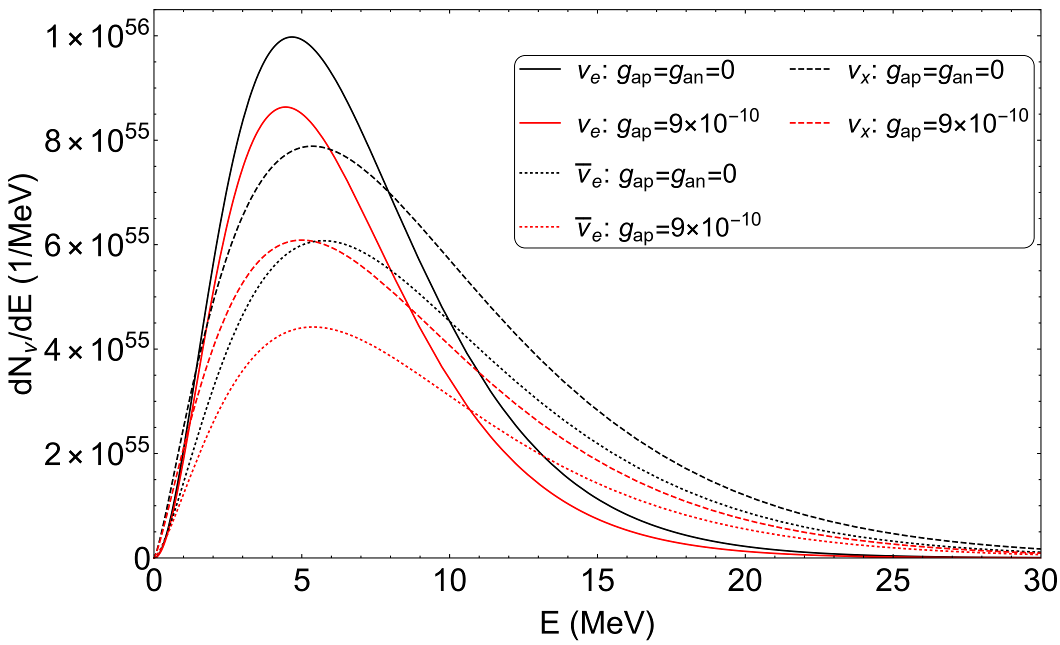

Figure 2.13: Time-integrated neutrino fluxes ($t \in [0.7; 10]\,\mathrm{s}$) for $g_{ap} = g_{an} = 0$ (black line) and $g_{ap} = 9 \times 10^{-10}$, $g_{an} = 0$ (red line).

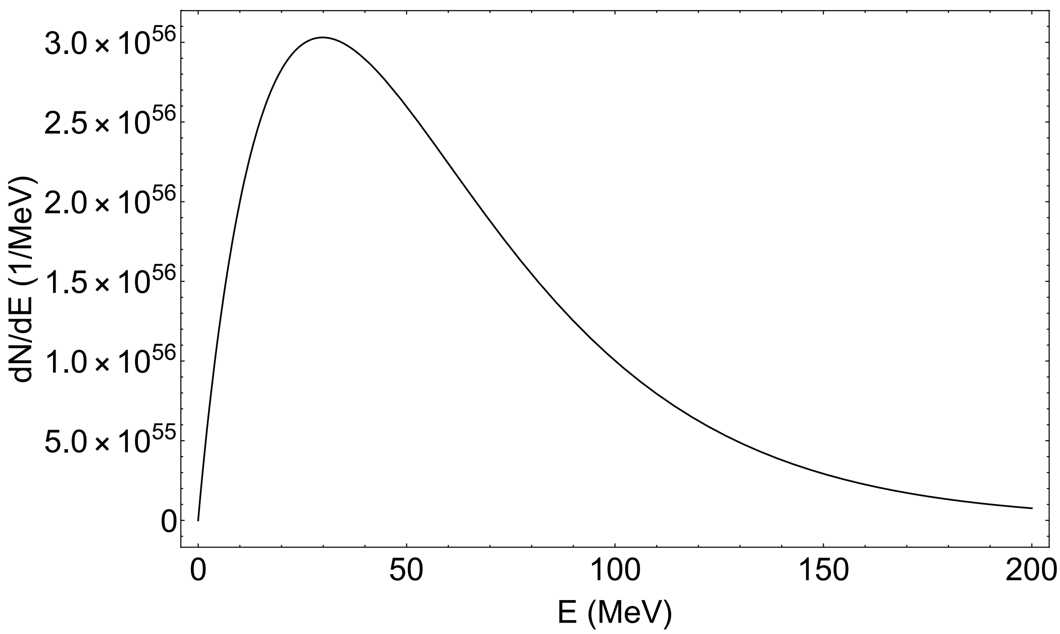

Figure 2.14: Time-integrated axion flux for $g_{ap} = 9 \times 10^{-10}$ and $g_{an} = 0$ ($t \in [0.7; 10]\,\mathrm{s}$).

Table 2.2: Best fit parameters for the time-integrated neutrino and axion fluxes ($t \in [0.7; 10]\,\mathrm{s}$), $g_{an} = 0$ and $g_{ap} = 9 \times 10^{-10}$.

Species	α	$\mathrm{N}_0\,(\times 10^{56})$	$\langle E \rangle$
ν_e	2.12	6.88	6.55
$\overline{\nu}_e$	1.48	5.18	9.01
ν_x	1.31	7.09	8.81
a	0.97	250.30	60.63

2.4.2 Trapping regime

The emission of trapped axions can be seen as a quasi-thermal emission from a surface rather than from the entire volume of the star [Raf96]. To determine the radius of this surface, the "axionsphere", we have to define the optical depth of a medium. Then, the axion spectrum can be approximated with a blackbody spectrum at the axionsphere temperature. The mean opacity is defined in terms of $x = \omega/T$ as [Raf96] [Appendix A.3]

$$\begin{aligned} k &= \left(\frac{C_N}{2f_a}\right)^2 \frac{\Gamma_\sigma}{m_N T}\hat{k} \; ; \\ \hat{k}^{-1} &= \frac{15}{8\pi^4}\int_0^\infty dx \, \frac{x^4 e^{2x}}{(e^x - 1)^3}\frac{2x}{s(x)} \; ; \\ s(x) &= 4\int du\, dv\, u^2 v^2 e^{|x| - u^2}\delta(u^2 - v^2 - |x|) = \\ &= \int_0^\infty dy\, e^{-y}\left(|x|y + y^2\right)^{1/2} \approx \sqrt{1 + |x|\frac{\pi}{4}} \; ; \end{aligned} \tag{2.20}$$

valid in the non-degenerate regime. We can introduce the optical depth [Raf96]

$$\tau(r) = \int_r^\infty dr \, k_a \rho \; . \tag{2.21}$$

Solving the equation $\tau(r_{\mathrm{ax}}) = 2/3$ we determine the radius of the axionsphere r_{ax}. The density and temperature profiles from the $18 M_\odot$ SN simulation for different times are plotted in Fig. (2.15)-(2.16). The calculated radius and temperature of the axionsphere are shown in Fig. (2.17)-(2.18). Now we can determine the axion luminosity by means of the Stefan's law

$$L = \frac{\pi^2}{120} 4\pi r_{\rm ax}^2 T^4(r_{\rm ax}) \; ; \tag{2.22}$$

and the axion energy distribution is given by a blackbody spectrum [Fig. (2.19)]

$$f(E) = \frac{1}{2T_{\rm ax}^3 \zeta(3)} \frac{E^2}{e^{E/T_{\rm ax}} - 1} \; ; \tag{2.23}$$

where $T_{\rm ax}$ is the temperature of the axionsphere and ζ is the zeta Riemann function. The rate of emitted axions in the SN explosion is given by $L/\langle E \rangle$, where $\langle E \rangle = 2.7\, T_{\rm ax}$ for a blackbody spectrum [Fig. (2.20)].

In order to compare the axion spectrum with the neutrino one, we can fit the time-integrated axion spectrum with Eq. (2.7). In Fig. (2.21) we show the numerical time-integrated flux and the fit with the parameters $\alpha = 1.18$, $\langle E \rangle = 11.19\,\mathrm{MeV}$ and $N_0 = 22.59 \times 10^{56}$.

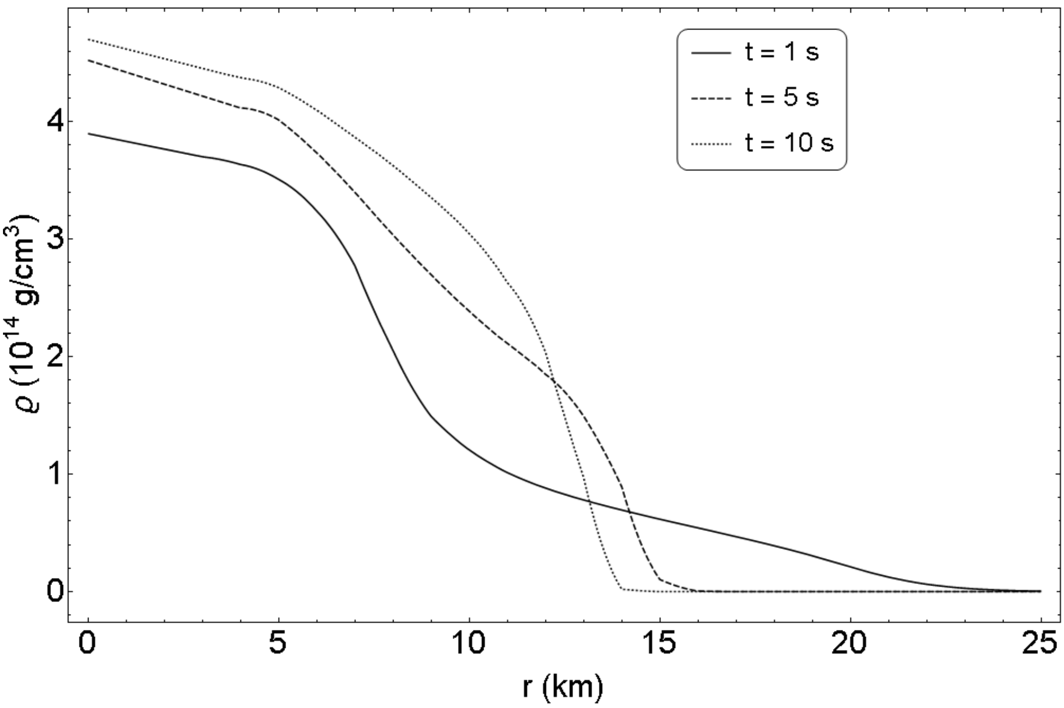

Figure 2.15: Supernova matter density at different post-bounce times for a $18M_\odot$ progenitor.

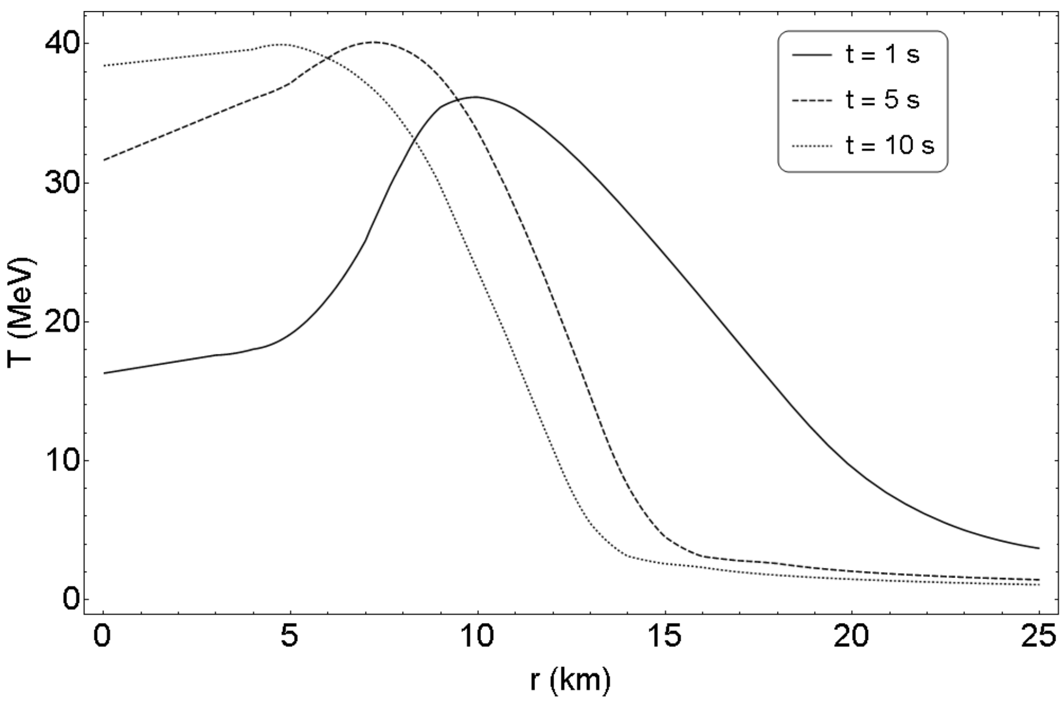

Figure 2.16: Supernova temperature at different post-bounce times for a $18M_\odot$ progenitor.

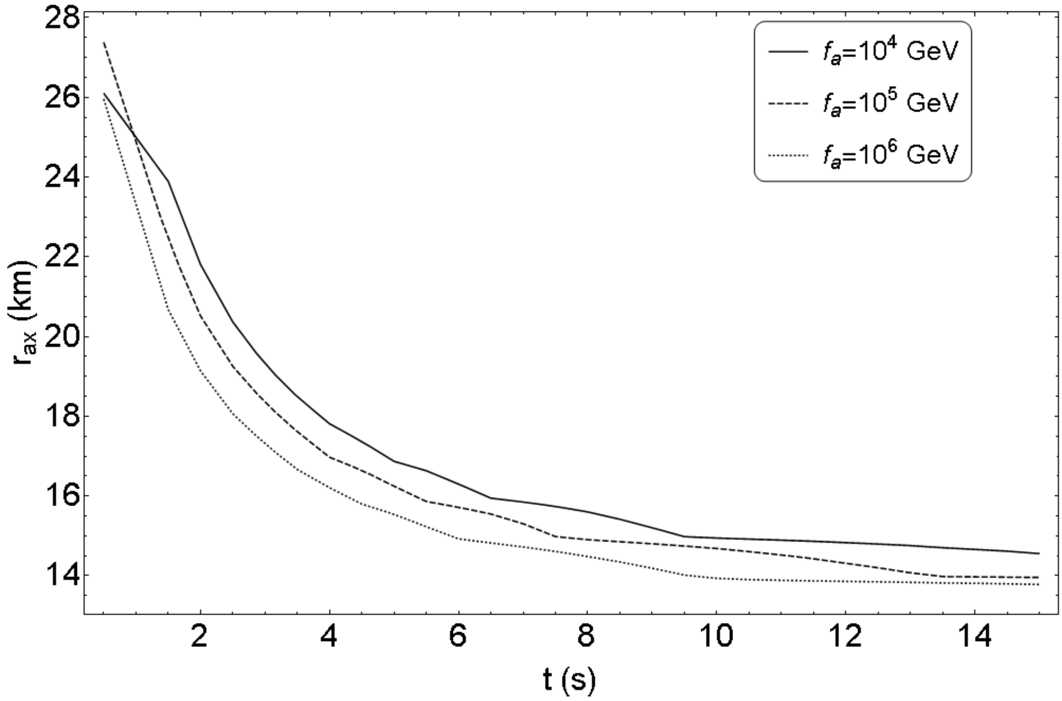

Figure 2.17: Radius of the axionsphere for different couplings.

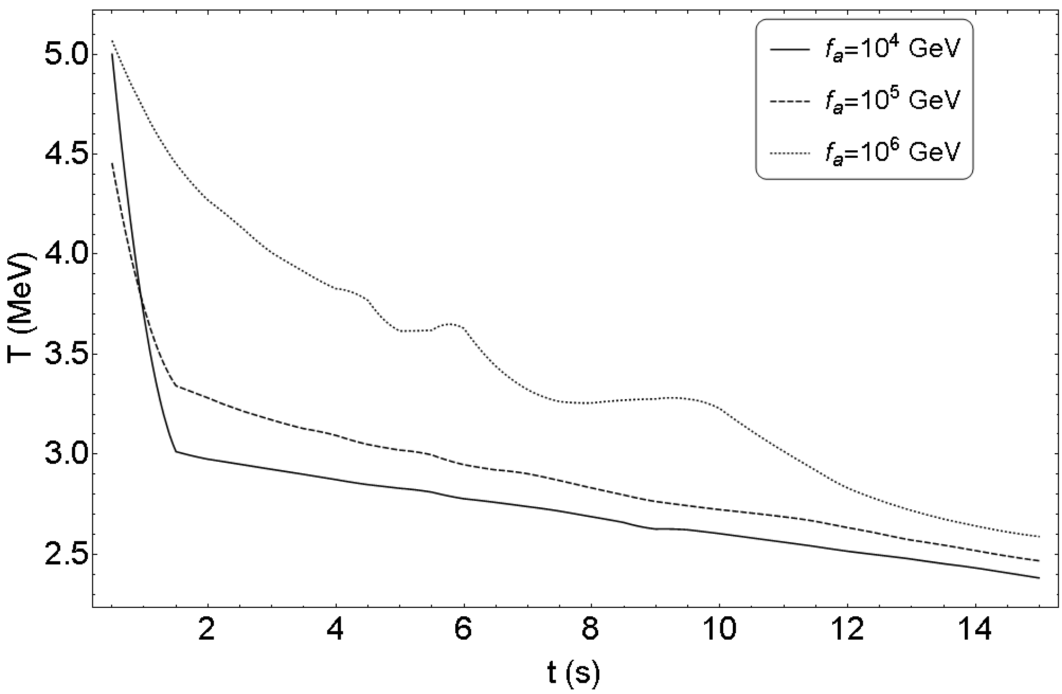

Figure 2.18: Temperature of the axionsphere for different couplings.

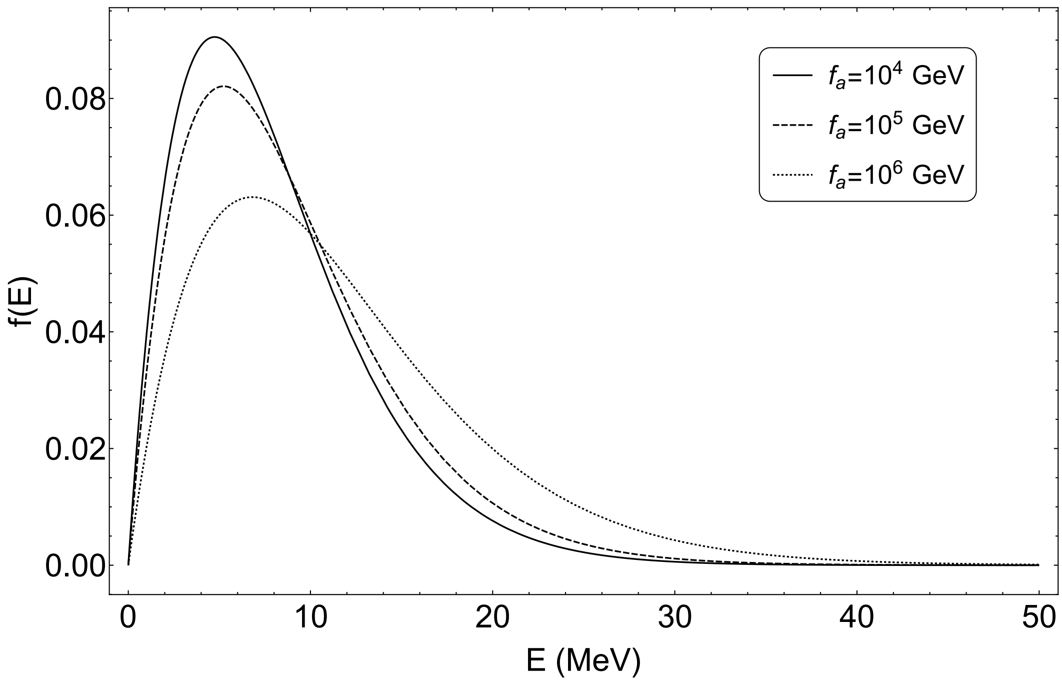

Figure 2.19: Axion spectrum for different couplings at post-bounce time $t = 2\,\mathrm{s}$.

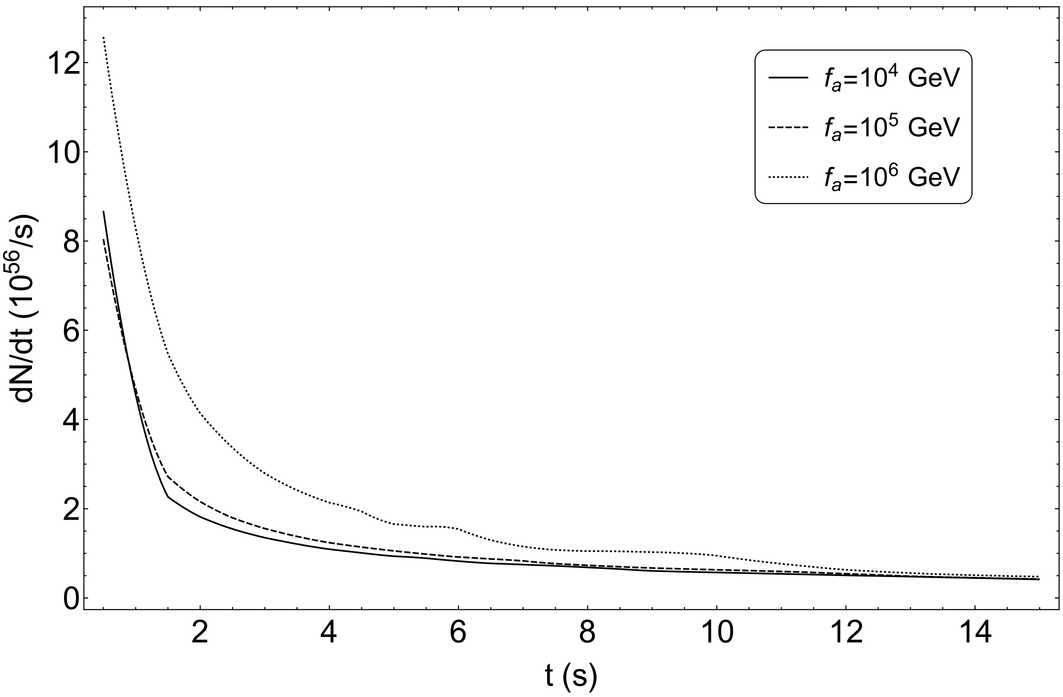

Figure 2.20: Rate of emitted axions for different couplings.

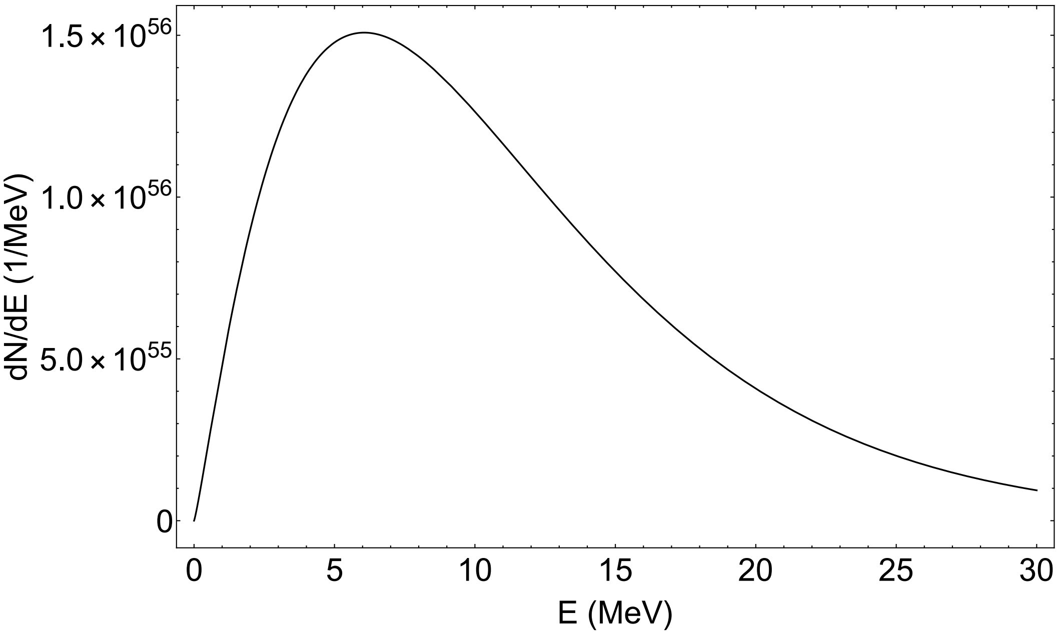

Figure 2.21: Time-integrated axion flux for $g_{ap} = g_{an} = 10^{-6}$ (from 0.7 s to 10 s).

Chapter 3

Axion-oxygen cross section

A galactic SN could produce an axion signal in water Cherenkov detectors thanks to the absorption of axions by the oxygen nuclei. Engel *et al.* elaborated these ideas in a seminal paper [Eng90]. We repeat this calculation updating it with the state-of-the-art nuclear models. In this Chapter we illustrate the calculation of the axion-oxygen absorption cross section. In Section 3.1 we recall the difference between the derivative and the pseudoscalar axion-fermion interaction Lagrangian. In Section 3.2 we compute the cross section for the axion nuclear absorption. In Section 3.3 we explicit the matrix element for the cross section calculation, and in Section 3.4 we present the nuclear model used. In conclusion, Section 3.5 deals with the energy levels excited by axion absorption and neutrino neutral current nuclear interactions and their radiative decays.

3.1 Axion-fermion interaction Lagrangian

In this section we will analyze the differences between the derivative and non-derivative coupling for axion-fermion interactions [Raf96]. As we saw in Chap. 1, in every axion model, the axion degree of freedom is enclosed in an additional Higgs field. In general the Lagrangian for a fermion field Ψ and a Higgs field Φ is

$$\begin{aligned} &\mathcal{L} = i\bar{\Psi}\gamma^\mu\partial_\mu\Psi + \partial_\mu\Phi^\dagger\partial^\mu\Phi - V(|\Phi|) - h\bar{\Psi}_L\Psi_R\Phi \ ; \\ &\Psi_L = \frac{1}{2}(1-\gamma^5)\Psi \ ; \\ &\Psi_R = \frac{1}{2}(1+\gamma^5)\Psi \ . \end{aligned} \tag{3.1}$$

The Lagrangian in Eq. (3.1) is invariant under the axial $U(1)_{\mathrm{PQ}}$ transformation

$$\begin{aligned}
&\Phi \rightarrow e^{i\alpha}\Phi \\
&\Psi_L \rightarrow e^{i\alpha/2}\Psi_L \\
&\Psi_R \rightarrow e^{-i\alpha/2}\Psi_R \ .
\end{aligned}$$

The Higgs potential has a minimum for $|\Phi| = f_a/\sqrt{2}$ and the ground state is

$$\langle\Phi\rangle = \frac{f_a}{\sqrt{2}}e^{i\alpha_0} \ ; \tag{3.2}$$

for a fixed α_0 and this vacuum configuration is no more invariant under $U(1)_{\mathrm{PQ}}$. Near the minimum we can write the Higgs field as

$$\Phi = \frac{f_a + \rho}{\sqrt{2}}e^{ia/f_a} \ ; \tag{3.3}$$

where ρ is the radial component of the Higgs field and the Lagrangian in Eq. (3.1) at low energy becomes

$$\begin{aligned}
\mathcal{L} &= i\bar{\Psi}\gamma^\mu\partial_\mu\Psi + \frac{1}{2}\partial_\mu a\partial^\mu a + \mathcal{L}_{\mathrm{int}} \ ; \\
\mathcal{L}_{\mathrm{int}} &= -m\bar{\Psi}e^{ia\gamma^5/f_a}\Psi \ ;
\end{aligned} \tag{3.4}$$

neglecting the large mass field ρ. Expanding the exponential in the interaction Lagrangian $\mathcal{L}_{\mathrm{int}}$ in Eq. (3.4) we obtain infinite interaction terms. At the lowest order we find the pseudoscalar coupling [Raf96]

$$\mathcal{L}_{\mathrm{int}} = -\frac{im}{f_a}a\bar{\Psi}\gamma^5\Psi + \dots \ . \tag{3.5}$$

We can also proceed in a different way. We redefine the fermion field as

$$\begin{aligned}
\Psi &\rightarrow e^{-ia\gamma^5/2f_a}\Psi \ ; \\
\bar{\Psi} &\rightarrow \bar{\Psi}e^{-ia\gamma^5/2f_a} \ ;
\end{aligned} \tag{3.6}$$

and the Lagrangian in Eq. (3.4) becomes

$$\begin{aligned}
\mathcal{L} = {} & i\bar{\Psi}e^{-ia\gamma^5/2f_a}\gamma^\mu\left(e^{-ia\gamma^5/2f_a}\partial_\mu\Psi - \frac{i}{2f_a}e^{-ia\gamma^5/2f_a}\partial_\mu a\gamma^5\Psi\right) + \\
& + \frac{1}{2}\partial_\mu a\partial^\mu a - m\bar{\Psi}\Psi = \\
& = \bar{\Psi}(i\gamma^\mu\partial_\mu - m)\Psi + \frac{1}{2}\partial_\mu a\partial^\mu a + \frac{1}{2f_a}\bar{\Psi}\gamma^\mu\gamma^5\Psi\partial_\mu a \ .
\end{aligned} \tag{3.7}$$

The Lagrangian in Eq. (3.4) loses the exponential coupling in the mass term, acquiring an exact derivative coupling coming from the kinetic term [Raf96]

$$\mathcal{L}_{\rm int} = \frac{1}{2f_a}\bar{\Psi}\gamma^\mu\gamma^5\Psi\partial_\mu a \ . \tag{3.8}$$

Since pions are Goldstone bosons, their interactions have a form similar to that of the axions. In the process $pp \to pp\pi^0$ the cross section obtained by using the derivative Lagrangian is in accord to experimental data. In fact, both the interaction Lagrangians give the same results except when two Goldstone bosons are attached to one fermion line as in the diagram below

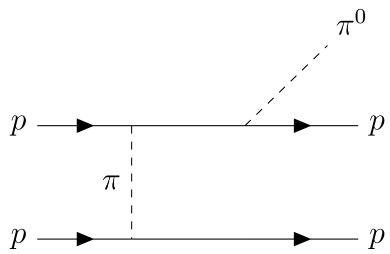

In this case one must use at least a derivative Lagrangian [Eq. (3.8)] for one Goldstone boson [Raf96].

3.2 Axion-nucleus scattering cross section

The description of the absorption of an axion by an atomic nucleus is a process which implies the interaction of an elementary particle with a many-body system. We describe this process by considering first the interaction between the axion and a single nucleon, which we consider a structureless particle, and, in a second step, we consider the nucleus a many-nucleon system. Due to the low mass of the axion, we assume that it is massless. First of all we consider the following axion-nucleus interaction Lagrangian [Eng90]

$$\begin{aligned}
\mathcal{L} &= \frac{1}{2f_a}\bar{\Psi}_N\gamma^\mu\gamma^5(C_0 + C_1\boldsymbol{\tau}_3)\Psi_N\partial_\mu a \ ; \\
C_0 &= \frac{1}{2}(C_p + C_n) \ ; \\
C_1 &= \frac{1}{2}(C_p - C_n) \ ; \\
\Psi_N &= \begin{pmatrix} p \\ n \end{pmatrix} \ ;
\end{aligned} \tag{3.9}$$

where $\boldsymbol{\tau}_3$ is a Pauli matrix and $C_{p,n}$ are the proton and neutron coupling constants. From this Lagrangian [Eq. (3.9)] we can compute the Hamiltonian:

$$\begin{aligned}
\frac{\partial \mathcal{L}}{\partial(\partial_0 a)} &= \frac{1}{2f_a}\bar{\Psi}_N\gamma^0\gamma^5(C_0 + C_1\boldsymbol{\tau}_3)\Psi_N\ ; \\
\frac{\partial \mathcal{L}}{\partial(\partial_0 \Psi)} &= 0\ ; \\
\frac{\partial \mathcal{L}}{\partial(\partial_0 \bar{\Psi})} &= 0\ ;
\end{aligned} \tag{3.10}$$

and then

$$\begin{aligned}
\mathcal{H} &= \frac{\partial \mathcal{L}}{\partial(\partial_0 a)}\partial_0 a - \mathcal{L} = \\
&= \frac{1}{2f_a}\left(\bar{\Psi}_N\gamma^0\gamma^5(C_0 + C_1\boldsymbol{\tau}_3)\Psi_N\partial_0 a - \bar{\Psi}_N\gamma^\mu\gamma^5(C_0 + C_1\boldsymbol{\tau}_3)\Psi_N\partial_\mu a\right) = \\
&= -\frac{1}{2f_a}\bar{\Psi}_N\gamma^i\gamma^5(C_0 + C_1\boldsymbol{\tau}_3)\Psi_N\partial_i a\ ;
\end{aligned} \tag{3.11}$$

where greek indices vary from 0 to 3 and the latin ones from 1 to 3. The initial state is formed by an axion of momentum $\mathbf{p}$ and the nucleus in its ground state. The axion state is $|\mathbf{p}\rangle$ and the initial nucleus state is indicated as $|\alpha\rangle$. In the final state the axion is absorbed and the nucleus is in an excited state. The state without the axion is $|0\rangle$ and the final nucleus state is $|\beta\rangle$. Both the nuclear states $|\alpha\rangle$ and $|\beta\rangle$ are energy and angular momentum eigenstates. The transition amplitude between these states is

$$M_{\mathrm{fi}} = \langle f|\left(\int d^3r dt\, \mathcal{H}_{\mathrm{fi}}\right)|i\rangle = -\frac{1}{2f_a}\int d^3r dt \langle\beta|J^i(\mathbf{r},t)|\alpha\rangle\langle 0|\partial_i a(\mathbf{r},t)|\mathbf{p}\rangle\ ; \tag{3.12}$$

where

$$J^i(\mathbf{r},t) = \bar{\Psi}_N(\mathbf{r},t)\gamma^i\gamma^5(C_0 + C_1\boldsymbol{\tau}_3)\Psi_N(\mathbf{r},t)\ ; \tag{3.13}$$

is the hadronic current. The time dependence of the hadronic current [Eq. (3.13)] can be isolated by expressing the current in the Heisenberg representation

$$\langle\beta|J^i(\mathbf{r},t)|\alpha\rangle = \langle\beta|e^{iHt}J^i(\mathbf{r},0)e^{-iHt}|\alpha\rangle = e^{i(E_\beta - E_\alpha)t}\langle\beta|J^i(\mathbf{r})|\alpha\rangle\ . \tag{3.14}$$

The axion current can be computed expanding the axion field in plane waves[1]:

$$
\begin{aligned}
a(\mathbf{r},t) &= \int \frac{d^3q}{\sqrt{V}} \frac{1}{\sqrt{2E_q}} \left(e^{-iE_q t + i\mathbf{q}\cdot\mathbf{r}} a_q + e^{iE_q t - i\mathbf{q}\cdot\mathbf{r}} a_q^\dagger \right) \; ; \\
\langle 0|\partial_i a(\mathbf{r},t)|\mathbf{p}\rangle &= \langle 0|\partial_i a(\mathbf{r},t) a_p^\dagger|0\rangle = \frac{e^{-iE_p t + i\mathbf{p}\cdot\mathbf{r}}}{\sqrt{2E_p V}} ip_i \; ;
\end{aligned}
\tag{3.15}
$$

where V is a finite normalization volume; $E_q = |\mathbf{q}|$; $a_q^\dagger$ and a_q are the creation and destruction operators of an axion state of momentum $\mathbf{q}$. Using Eq. (3.12), Eq. (3.14) and Eq. (3.15) we obtain

$$
\begin{aligned}
M_{\text{fi}} &= -\frac{1}{2f_a} \int dt\, e^{i\Delta E t} \int \frac{d^3r}{\sqrt{2E_p V}} \langle\beta|J^i(\mathbf{r})|\alpha\rangle \partial_i e^{i\mathbf{p}\cdot\mathbf{r}} = \\
&= -\frac{1}{2f_a} 2\pi\delta(\Delta E) \int \frac{d^3r}{\sqrt{2E_p V}} \langle\beta|J^i(\mathbf{r})|\alpha\rangle \partial_i e^{i\mathbf{p}\cdot\mathbf{r}} \; ; \\
\Delta E &= E_\beta - E_\alpha - E_p \; .
\end{aligned}
\tag{3.16}
$$

The plane wave in Eq. (3.16) can be expanded in spherical harmonics [Mes67]

$$
e^{i\mathbf{p}\cdot\mathbf{r}} = 4\pi \sum_{j=0}^{\infty} \sum_{m=-l}^{l} i^j j_j(qr) {Y_{j,m}}^*(\Omega_p) Y_{j,m}(\Omega_r) \; ; \tag{3.17}
$$

where the two spherical harmonics depend on the angular coordinate of the $\mathbf{p}$ and $\mathbf{r}$ vectors. Without losing generality, we can select the z axis along the $\mathbf{p}$ direction. Therefore

$$
{Y_{j,m}}^*(0) = \left[\frac{2j+1}{4\pi} \right]^{1/2} \delta_{m,0} \; . \tag{3.18}
$$

Then Eq. (3.17) becomes

$$
e^{i\mathbf{p}\cdot\mathbf{r}} = \sum_{j=0}^{\infty} i^j \sqrt{4\pi(2j+1)} j_j(pr) Y_{j,0}(\Omega) \; ; \tag{3.19}
$$

[1]In the following we use the finite volume normalization. The integral representation of the Dirac delta will be written as

$$
\delta^3(\mathbf{r}-\mathbf{r}_0) = \frac{1}{V} \int d^3p\, e^{i\mathbf{p}\cdot(\mathbf{r}-\mathbf{r}_0)} \; .
$$

The transition to $V \to \infty$ is equivalent to the substitution $V \to (2\pi)^3$.

where we defined $\Omega = \Omega_r$ and then

$$\partial_i e^{i\mathbf{p}\cdot\mathbf{r}} = \sum_{j=0}^{\infty} i^j \sqrt{4\pi(2j+1)}\partial_i(j_j(pr)Y_{j,0}(\Omega)) \ . \tag{3.20}$$

The matrix element [Eq. (3.12)] can be written as

$$M_{\text{fi}} = -2\pi\delta(\Delta E)\frac{1}{2f_a\sqrt{2E_pV}} \sum_{j=0}^{\infty} i^j \sqrt{4\pi(2j+1)}E_p \int d^3r\frac{1}{p}\partial_i(j_j(pr)Y_{j,0}(\Omega))\langle\beta|J^i(\mathbf{r})|\alpha\rangle \ . \tag{3.21}$$

In Eq. (3.21) we have multiplied and divided by p, using the hypothesis of massless axion ($p = E_p$). In order to verify our result [Eq. (3.16)] we repeat this calculation using the equivalent non-derivative coupling

$$\mathcal{H} = i\frac{m}{f_a}\bar{\Psi}_N\gamma^5(C_0 + C_1\boldsymbol{\tau}_3)\Psi_N a \ . \tag{3.22}$$

Following the steps used to arrive up to Eq. (3.21) we obtain the expression of the matrix element

$$M_{\text{fi}} = 2\pi\delta(\Delta E)\frac{im}{f_a\sqrt{2E_pV}} \sum_j i^j \sqrt{4\pi(2j+1)}E_p \int d^3r\frac{1}{p}j_j(pr)Y_{j,0}(\Omega)\langle\beta|P(\mathbf{r})|\alpha\rangle \ ; \tag{3.23}$$

where

$$P(\mathbf{r}) = \bar{\Psi}_N\gamma^5(C_0 + C_1\boldsymbol{\tau}_3)\Psi_N \ . \tag{3.24}$$

Integrating by parts Eq. (3.21) and using that

$$\partial_\mu J^\mu(\mathbf{r}) = \partial_i J^i(\mathbf{r}) = 2imP(\mathbf{r}) \ ; \tag{3.25}$$

we obtain the same expression as Eq. (3.23).

3.3 Single particle transitions

The nuclear states are eigenstates of angular momentum, energy and parity. The ground state of the ^{16}O nucleus is characterized by angular momentum and parity 0^+. The interaction Lagrangian [Eq. (3.9)] is symmetric under parity, which means that in this process parity is conserved. In the initial state the parity is $+1$ for the nucleon, -1 for the axion and $(-1)^j$ for the relative angular momentum. In the final state, the nucleus will be excited into a state with angular momentum j and parity $(-1)^{j+1}$ and those states are called "unnatural" states. Therefore, after the axion absorption, the final nuclear state has the angular momentum of the incident axion j and parity determined by the conservation law $(-1)^{j+1}$. We can now compute the total cross section for the axion-nucleus absorption. The matrix element squared in Eq. (3.21) with $|\alpha\rangle = |J_i, M_i\rangle$ and $|\beta\rangle = |J_f, M_f\rangle$ is

$$|M_{\rm fi}|^2 = 2\pi\delta(\Delta E) T \frac{E_p}{8f_a^2 V} \left| \sum_{j=0}^{\infty} i^j \sqrt{4\pi(2j+1)} \langle J_f, M_f | L_{j,0} | J_i, M_i \rangle \right|^2 \; ; \tag{3.26}$$

where we defined the multipole operator [Sch80]

$$L_{j,0} = \frac{i}{p} \int d^3 r \partial_i (j_j(pr) Y_{j,0}(\Omega)) J^i(\mathbf{r}) \; . \tag{3.27}$$

The factor T in Eq. (3.26) is the process time duration and it comes from the square of the Dirac delta:

$$\begin{aligned} \delta(\Delta E) &= \lim_{T\to\infty} \frac{1}{2\pi} \int_{-T/2}^{T/2} dt\, e^{-i\Delta E t} \; ; \\ [\delta(\Delta E)]^2 &= \delta(\Delta E) \lim_{T\to\infty} \frac{1}{2\pi} \int_{-T/2}^{T/2} dt\, e^{-i\Delta E t} = \\ &= \delta(\Delta E) \lim_{T\to\infty} \frac{1}{2\pi} \int_{-T/2}^{T/2} dt = \frac{T}{2\pi} \delta(\Delta E) \; ; \end{aligned} \tag{3.28}$$

where $T \to \infty$, but it is not explicitly written in the last step. From the Wigner-Eckart theorem for spherical operators, with the convention used in [Sch80]:

$$\langle J_f, M_f | T_{l,m} | J_i, M_i \rangle = (-1)^{J_f - M_f} \begin{pmatrix} J_f & l & J_i \\ -M_f & m & M_i \end{pmatrix} \langle J_f || T_{l,m} || J_i \rangle \; . \tag{3.29}$$

Squaring the matrix element, mediating over the inital states and summing over the final states, we obtain [Sch80]

$$
\begin{aligned}
&\frac{1}{2J_i+1}\sum_{M_i,M_f}|\langle J_f,M_f|T_{l,m}|J_i,M_i\rangle|^2 = \\
=&\frac{|\langle J_f||T_{l,m}||J_i\rangle|^2}{2J_i+1}\sum_{M_i,M_f}\begin{pmatrix} J_f & l & J_i \\ -M_f & m & M_i\end{pmatrix}\begin{pmatrix} J_f & l' & J_i \\ -M_f & m' & M_i\end{pmatrix} = \\
=&\delta_{l,l'}\delta_{m,m'}\frac{|\langle J_f||T_{l,m}||J_i\rangle|^2}{(2l+1)(2J_i+1)}\ .
\end{aligned}
\tag{3.30}
$$

Therefore Eq. (3.26) with the ground state of ^{16}O as initial state becomes

$$
|M_{\rm fi}|^2 = \frac{\pi^2 E_p T\delta(\Delta E)}{f_a^2 V}|\langle J^P||L_{j,0}||0^+\rangle|^2\ ; \tag{3.31}
$$

where J is the axion angular momentum, P is the final state parity and J^P identifies the final nuclear state. The total cross section is

$$
\sigma = \int dE\frac{d\rho}{dE}\frac{|M_{\rm fi}|^2 V}{T}\ ; \tag{3.32}
$$

where $d\rho/dE$ is the final states density. Ignoring the nucleus recoil, $d\rho/dE = 4$ for the two isospin and spin nucleon possible states. Then we arrive at the following cross section

$$
\sigma = \frac{4\pi^2 E_p}{f_a^2}|\langle J^P||L_{j,0}||0^+\rangle|^2\ . \tag{3.33}
$$

The cross section obtained from Eq. (3.23) is

$$
\sigma = \frac{4\pi^2 E_p}{f_a^2}|\langle j^P||M_{j,0}||0^+\rangle|^2\ ; \tag{3.34}
$$

defining [Sch80]

$$
M_{j,0} = \frac{2m}{p}\int d^3r j_j(pr)Y_{j,0}(\Omega)P(\mathbf{r})\ . \tag{3.35}
$$

Using Eq. (3.25) we see that Eq. (3.35) and Eq. (3.34) are equivalent to Eq. (3.33).

The cross section in Eq. (3.33) contains a matrix element between the nuclear states $|0^+\rangle$ and $|J^P\rangle$. In a simple model we can imagine that the axion is absorbed by a nucleon below the Fermi energy, and then it is excited in a higher level. With this simplification, the "macroscopic" reduced matrix element $\langle J^P || L_{j,0} || 0^+ \rangle$ can be calculated from the "microscopic" matrix element $\langle j_f || L_{j,0} || j_i \rangle$, where $j_{i,f}$ is the nucleon angular momentum. The great simplification is that we reduced a many-body system to a calculation of single particle matrix elements. The single particle wavefunction is

$$\phi_i(\mathbf{r}) = R^t_{nlj}(r) \sum_{\mu s_z} \langle l\mu\, 1/2\, s_z | jm \rangle Y_{l\mu}(\Omega) \chi^{s_z} \chi^t \; ; \tag{3.36}$$

where $R^t_{nlj}(r)$ is the radial wavefunction; χ^{s_z} and χ^t are Pauli spinors for the third component of spin and isospin respectively.

To compute explicitly the cross section in Eq. (3.33) we must evaluate the expression of the hadronic current

$$\mathbf{j}(\mathbf{r}, t) = \bar{\Psi}_N \boldsymbol{\gamma} \gamma^5 (C_0 + C_1 \boldsymbol{\tau}_3) \Psi_N \; . \tag{3.37}$$

We compute the matrix element of the current in Eq. (3.37) between two free nucleon states with momentum $\mathbf{p}_{i,f}$, spin $s_{i,f}$ and mass m. Considering a proton, the hadron current is

$$\begin{aligned}
&\langle \mathbf{p}_f, s_f | \mathbf{j} | \mathbf{p}_i, s_i \rangle = \frac{C_p}{V} \sqrt{\frac{E_{p_f} + m}{2E_{p_f}}} \sqrt{\frac{E_{p_i} + m}{2E_{p_i}}} \bar{u}(\mathbf{p}_f, s_f) \boldsymbol{\gamma} \gamma^5 u(\mathbf{p}_i, s_i) \; ; \\
&u(\mathbf{p}, s) = \begin{pmatrix} \chi^s \\ \frac{\sigma \cdot \mathbf{p}}{E+m} \chi^s \end{pmatrix} \; ; \\
&\chi^{+1/2} = \begin{pmatrix} 1 \\ 0 \end{pmatrix} \; ; \\
&\chi^{-1/2} = \begin{pmatrix} 0 \\ 1 \end{pmatrix} \; ;
\end{aligned} \tag{3.38}$$

where the spinors χ^s refer to the spin space. The nucleons mass is about 1 GeV and their average kinetic energy in a nucleus is about 20 MeV, therefore we can apply the non-relativistic approximation. At the lowest order ($|\mathbf{p}| \ll E = m$)

$$\begin{aligned}
\langle \mathbf{p}_f, s_f | \mathbf{j} | \mathbf{p}_i, s_i \rangle &= \frac{C_p}{V} \bar{u}(\mathbf{p}_f) \boldsymbol{\gamma} \gamma^5 u(\mathbf{p}_i) \; ; \\
\bar{u}(\mathbf{p}_f) \gamma^i \gamma^5 u(\mathbf{p}_i) &= \begin{pmatrix} \chi^{s_f \dagger} & 0 \end{pmatrix} \begin{pmatrix} 0 & \sigma^i \\ -\sigma^i & 0 \end{pmatrix} \begin{pmatrix} 0 & 1 \\ 1 & 0 \end{pmatrix} \begin{pmatrix} \chi^{s_i} \\ 0 \end{pmatrix} = \\
&= \chi^{s_f \dagger} \sigma^i \chi^{s_i} \; .
\end{aligned} \tag{3.39}$$

In general, for every isospin state, introducing the isospin spinors χ^t

$$\begin{aligned}
&\langle \mathbf{p}_f, s_f, t_f | \mathbf{j} | \mathbf{p}_i, s_i, t_i \rangle = \frac{1}{V} \chi^{t_f \dagger} (C_0 + C_1 \boldsymbol{\tau}_3) \chi^{t_i} \chi^{s_f \dagger} \boldsymbol{\sigma} \chi^{s_i} \; ; \\
&\chi^{+1/2} = \begin{pmatrix} 1 \\ 0 \end{pmatrix} \; ; \\
&\chi^{-1/2} = \begin{pmatrix} 0 \\ 1 \end{pmatrix} \; .
\end{aligned} \tag{3.40}$$

In the r-space, the current is

$$\mathbf{j}(\mathbf{r}) = \frac{1}{V} (C_0 + C_1 \boldsymbol{\tau}_3) \int d^3 q \boldsymbol{\sigma} e^{-i\mathbf{q}(\mathbf{r}-\mathbf{r}_i)} = (C_0 + C_1 \boldsymbol{\tau}_3) \boldsymbol{\sigma} \delta^3 (\mathbf{r} - \mathbf{r}_i) \; ; \tag{3.41}$$

where $\mathbf{r}_i$ is the position of the i-th nucleon. Once obtained the hadronic current operator in the non-relativistic limit [Eq. (3.41)], we can compute the multipole operator in Eq. (3.27) to eventually calculate the reduced matrix element in Eq. (3.33). Then, the operator in Eq. (3.27) becomes

$$\begin{aligned}
L_{j,0} &= \frac{i}{p} (C_0 + C_1 \boldsymbol{\tau}_3) \int d^3 r \boldsymbol{\sigma} \cdot \nabla (j_j(pr) Y_{j,0}(\Omega)) \delta^3 (\mathbf{r} - \mathbf{r}_i) = \\
&= \frac{i}{p} (C_0 + C_1 \boldsymbol{\tau}_3) \boldsymbol{\sigma} \cdot \nabla (j_j(pr_i) Y_{j,0}(\Omega)) \; .
\end{aligned} \tag{3.42}$$

The operator in Eq. (3.42) can be rewritten in terms of the vector spherical harmonics [Sch80]

$$\begin{aligned}
&\mathcal{Y}_{l,j,m}(\Omega) = \sum_{nq} \langle ln1q | jm \rangle Y_{l,n}(\Omega) \mathbf{e}_q \; ; \\
&\mathbf{e}_{\pm 1} = \mp \frac{1}{\sqrt{2}} (u_x \pm i u_y) \; ; \\
&\mathbf{e}_0 = u_z \; ;
\end{aligned} \tag{3.43}$$

where $u_{x,y,z}$ are the unit vectors along the cartesian axes. We obtain

$$\begin{aligned}
&\nabla (j_j(pr) Y_{j,0}(\Omega)) = \\
&\qquad = p \left[\sqrt{\frac{j+1}{2j+1}} j_{j+1}(pr) \mathcal{Y}_{j+1,j,0} + \sqrt{\frac{j}{2j+1}} j_{j-1}(pr) \mathcal{Y}_{j-1,j,0} \right] \; ;
\end{aligned} \tag{3.44}$$

and

$$\langle j_p || j_{j+1}(pr)\mathcal{Y}_{j,j+1,0}\cdot\boldsymbol{\sigma}||j_h\rangle =$$
$$= (-1)^{j+j_h+\frac{3}{2}}\sqrt{\frac{(2j_p+1)(2j_h+1)}{4\pi}}\xi(l_p+l_h+j+1)\begin{pmatrix} j_p & j_h & j \\ 1/2 & -1/2 & 0 \end{pmatrix}$$
$$\left[\frac{\chi_p+\chi_h+j+1}{\sqrt{j+1}}\right]\int dr\, r^2 j_{j+1}(pr)R_p^* R_h \;; \tag{3.45}$$

$$\langle j_p || j_{j-1}(pr)\mathcal{Y}_{j,j-1,0}\cdot\boldsymbol{\sigma}||j_h\rangle =$$
$$= (-1)^{j+j_h+\frac{3}{2}}\sqrt{\frac{(2j_p+1)(2j_h+1)}{4\pi}}\xi(l_p+l_h+j+1)\begin{pmatrix} j_p & j_h & j \\ 1/2 & -1/2 & 0 \end{pmatrix}$$
$$\left[\frac{\chi_p+\chi_h-j}{\sqrt{j}}\right]\int dr\, r^2 j_{j-1}(pr)R_p^* R_h \;; \tag{3.46}$$

where R is the nucleon radial wavefunction as defined in Eq. (3.36); $\xi(L)$ is 1 for even L, 0 otherwise; and

$$\chi = (l-j)(2j+1)\;;$$
$$|j_p - j_h| \le j \le |j_p + j_h|\;.$$

The matrix element can also be computed from the pseudoscalar Lagrangian [Eq. (3.35)]. The explicit expression is

$$\langle \mathbf{p}_f, s_f|P|\mathbf{p}_i, s_i\rangle = \frac{C_p}{V}\sqrt{\frac{E_{p_f}+m}{2E_{p_f}}}\sqrt{\frac{E_{p_i}+m}{2E_{p_i}}}\bar{u}(\mathbf{p}_f, s_f)\gamma^5 u(\mathbf{p}_i, s_i)\;; \tag{3.47}$$

at the zeroth order of the non-relativistic approximation

$$\langle \mathbf{p}_f, s_f|P|\mathbf{p}_i, s_i\rangle = \frac{C_p}{V}\bar{u}(\mathbf{p}_f)\gamma^5 u(\mathbf{p}_i)\;;$$
$$\bar{u}(\mathbf{p}_f)\gamma^5 u(\mathbf{p}_i) = \begin{pmatrix} \chi^{s_f\dagger} & 0 \end{pmatrix}\begin{pmatrix} 1 & 0 \\ 0 & -1 \end{pmatrix}\begin{pmatrix} 0 & 1 \\ 1 & 0 \end{pmatrix}\begin{pmatrix} \chi^{s_i} \\ 0 \end{pmatrix} = 0\;. \tag{3.48}$$

Since the matrix element in Eq. (3.48) is zero, we expand to the first order in $|\mathbf{p}|/m$

$$\bar{u}(\mathbf{p}_f)\gamma^5 u(\mathbf{p}_i) = \begin{pmatrix} \chi^{s_f\dagger} & \chi^{s_f\dagger}\frac{\sigma\cdot\mathbf{p_f}}{2m} \end{pmatrix}\begin{pmatrix} 1 & 0 \\ 0 & -1 \end{pmatrix}\begin{pmatrix} 0 & 1 \\ 1 & 0 \end{pmatrix}\begin{pmatrix} \chi^{s_i} \\ \frac{\sigma\cdot\mathbf{p_i}}{2m}\chi^{s_i} \end{pmatrix} =$$
$$= \frac{1}{2m}\chi^{\dagger s_f}\boldsymbol{\sigma}\chi^{s_i}\cdot(\mathbf{p}_i - \mathbf{p}_f)\;; \tag{3.49}$$

and then

$$\langle \mathbf{p}_f, s_f, t_f | P | \mathbf{p}_i, s_i, t_i \rangle = \frac{1}{2mV} \chi^{t_f \dagger} (C_0 + C_1 \boldsymbol{\tau}_3) \chi^{t_i} \chi^{s_f \dagger} \boldsymbol{\sigma} \chi^{s_i} \cdot (\mathbf{p}_i - \mathbf{p}_f) \; . \tag{3.50}$$

In the r-space

$$\begin{aligned} P(\mathbf{r}) &= \frac{1}{2mV}(C_0 + C_1 \boldsymbol{\tau}_3) \int d^3 q e^{i\mathbf{q}(\mathbf{r}-\mathbf{r}_i)} \boldsymbol{\sigma} \cdot \mathbf{q} = \\ &= -\frac{i}{2m}(C_0 + C_1 \boldsymbol{\tau}_3) \boldsymbol{\sigma} \cdot \nabla(\delta^3(\mathbf{r} - \mathbf{r}_i)) \; ; \end{aligned} \tag{3.51}$$

where $\mathbf{q} = \mathbf{p}_i - \mathbf{p}_f$. Inserting Eq. (3.51) in Eq. (3.35) and integrating by parts we obtain the same resuts as Eq. (3.42):

$$\begin{aligned} M_{l,0} &= -\frac{i}{p}(C_0 + C_1 \boldsymbol{\tau}_3) \boldsymbol{\sigma} \cdot \int d^3 r \nabla(\delta^3(\mathbf{r} - \mathbf{r}_i)) j_l(pr) Y_{l,0}(\Omega) = \\ &= \frac{i}{p}(C_0 + C_1 \boldsymbol{\tau}_3) \boldsymbol{\sigma} \cdot \nabla(j_l(pr_i) Y_{l,0}(\Omega)) \; . \end{aligned} \tag{3.52}$$

3.4 Nuclear models

In order to calculate the cross section, we need to explicit the matrix element in Eq. (3.33). In a mean field approximation all the states below the Fermi energy are occupied. Excited states are obtained by moving a nucleon to a state above the Fermi energy. This model cannot account for a collective behaviour. Hovewer, the nucleus is a many body system where nucleons collective excitations are relevant. For this reason we used a description of the excitation spectrum which consider both collective and single particle excited states. This approach is known as Random Phase Approximation (RPA) [Sch80]. In spite of the complexity of this system, we can describe nuclear configurations as a linear combination of particle-hole states. We are interested in the ^{16}O nucleus, a closed shell nucleus [Fig. (3.1)].

The Schrödinger equation can be written as

$$H|\nu\rangle = \omega|\nu\rangle \; ; \tag{3.53}$$

where H is the many-body Hamiltonian, $|\nu\rangle$ is an excited state and $|0\rangle$ the ground state. The excited states of the system are obtained by acting with the creation operator $Q^\dagger_\nu$ on the ground state

$$Q^\dagger_\nu|0\rangle = |\nu\rangle \; ; \tag{3.54}$$

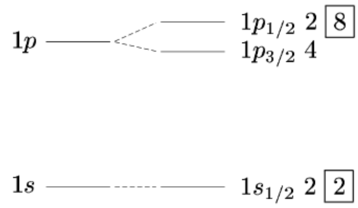

Figure 3.1: Oxygen nucleons ground state configuration.

and the ground state $|0\rangle$ is defined as

$$Q_\nu|0\rangle = 0 \; . \tag{3.55}$$

In our approximation, the operator in Eq. (3.54) takes contributions only from one particle-one hole transitions, ignoring the higher order transitions. In the RPA the creation operator is a linear combination of particle-hole a_p, a_h operators with coefficients X^ν_{ph} and Y^ν_{ph} [Sch80]

$$Q^\dagger_\nu = \sum_{ph}\left(X^\nu_{ph}a^\dagger_p a_h - Y^\nu_{ph}a^\dagger_h a_p\right) \; ; \tag{3.56}$$

where the subscripts p, h indicate the quantum numbers of particle and hole states. The many-body Hamiltonian containing two-body interactions only can be written as [Sch80]:

$$H = \sum_\alpha \epsilon_\alpha a^\dagger_\alpha a_\alpha - \frac{1}{2}\sum_{ijij}\bar{V}_{ijij} + \frac{1}{4}\sum_{\alpha\beta\alpha'\beta'}\bar{V}_{\alpha\beta\alpha'\beta'}N(a^\dagger_\alpha a^\dagger_\beta a_{\beta'}a_{\alpha'}) \; ; \tag{3.57}$$

where N indicates the normal ordering, the pedices i, j indicate only hole states (i.e. above the Fermi level) and the matrix element of the two-body interaction is

$$\begin{aligned} V_{\alpha\beta\gamma\delta} &= \int d^3r_1 d^3r_2\, \phi^*_\alpha(\mathbf{r_1})\phi^*_\beta(\mathbf{r_2})v(\mathbf{r_1},\mathbf{r_2})\phi_\gamma(\mathbf{r_1})\phi_\delta(\mathbf{r_2}) \; ; \\ \bar{V}_{ijij} &= V_{ijij} - V_{ijji} \; . \end{aligned} \tag{3.58}$$

The single particle energy ϵ_α is defined as

$$\epsilon_\alpha = \int d^3r\, \phi^*_\alpha(\mathbf{r})\left(-\frac{1}{2m}\nabla^2\right)\phi_\alpha(\mathbf{r}) + \sum_i \bar{V}_{\alpha i\alpha i} \; . \tag{3.59}$$

In the RPA theory the X^{ν}_{ph} and Y^{ν}_{ph} coefficients satisfy the following equations [Sch80]:

$$\begin{aligned} (\epsilon_p - \epsilon_h - \omega) X^{\nu}_{ph} + \sum_{p'h'} (v_{ph,p'h'} X^{\nu}_{p'h'} + u_{ph,p'h'} Y^{\nu}_{p'h'}) = 0 \ ; \\ (\epsilon_p - \epsilon_h + \omega) Y^{\nu}_{ph} + \sum_{p'h'} (v^{*}_{ph,p'h'} Y^{\nu}_{p'h'} + u^{*}_{ph,p'h'} X^{\nu}_{p'h'}) = 0 \ ; \end{aligned} \tag{3.60}$$

where the eigenvalue ω is the excitation energy, and the interaction terms are

$$\begin{aligned} v_{ph,p'h'} = \bar{V}_{ph'hp'} = \langle ph' | V | hp' \rangle - \langle ph' | V | p'h \rangle \ ; \\ u_{ph,p'h'} = \bar{V}_{pp'hh'} = \langle pp' | V | hh' \rangle - \langle pp' | V | h'h \rangle \ . \end{aligned} \tag{3.61}$$

The excited states are orthonormal

$$\langle \nu | \mu \rangle = \delta_{\nu\mu} \ ; \tag{3.62}$$

implying a relation among the X^{ν}_{ph} and Y^{ν}_{ph} coefficients

$$\sum_{ph} (X^{\nu}_{ph} X^{\mu}_{ph} - Y^{\nu}_{ph} Y^{\mu}_{ph}) = \delta_{\nu\mu} \ . \tag{3.63}$$

The matrix element of a one-body operator is [Sch80]

$$\langle J | T_{J,M} | 0 \rangle = \sum_{ph} \left[X^{J,M}_{ph} \langle j_p || T_{J,M} || j_h \rangle + (-1)^{J + j_p - j_h} Y^{J,M}_{ph} \langle j_h || T_{J,M} || j_p \rangle \right] \ ; \tag{3.64}$$

this is expressed in the angular momentum basis as explained in Appendix B.1.

3.4.1 Continuum RPA results

In this thesis we study axions in a broad range of energies, from a few MeV to a hundred of MeV. Hence we will use the Continuum RPA [Appendix B.2] to compute the cross section in Eq. (3.33) that includes the possibility of nucleon emission. The same cross sections can be evaluated with different types of nuclear interactions. We used the D1M, D1MTd and D1S interactions defined in [Gor09, Co18, Ber91], respectively [Appendix B.3]. These interactions have been used to solve Hartree-Fock equations. Our calculations describe the ^{16}O ground state and generate the set of single particle states and wave functions.

The binding energy per nucleon predicted by the three interactions are presented in Tab. (3.1). The calculated energy levels, obtained with the three forces used in our work, are shown in Tab. (3.2).

Table 3.1: Binding energy per nucleon of the nucleus ^{16}O . The data are expressed in MeV.

exp	D1M	D1Mtd	D1S
-7.97620	-7.97507	-8.02556	-8.11250

Table 3.2: Single particle energies obtained in our Hartree-Fock calculations. All the values are expressed in MeV. The lines divide levels below and above the Fermi energy.

PROTONS state	exp	D1M	D1MTd	D1S
2s1/2	-0.10	0.85	0.83	1.11
1d5/2	-0.60	-2.33	-2.25	-2.24
1p1/2	-12.11	-11.95	-12.04	-12.52
1p3/2	-18.44	-17.67	-17.74	-18.62
1s1/2	—	-32.78	-32.93	-35.41

NEUTRONS state	exp	D1M	D1MTd	D1S
2s1/2	-3.27	-2.21	-2.23	-1.87
1d5/2	-4.14	-5.77	-5.78	-5.61
1p1/2	-15.65	-15.14	-15.25	-15.66
1p3/2	-21.81	-20.95	-21.02	-21.86
1s1/2	—	-36.09	-36.19	-38.65

The excitation spectrum of unnatural parity states is shown in Tab. (3.3). The charge distribution of the ^{16}O ground state is another experimentally observed property of this nucleus. The Hartree-Fock results are shown in Fig. (3.2).

Table 3.3: Excitation energies of some unnatural parity states expressed in MeV.

state	exp	D1M	D1Mtd	D1S
2-	8.87	9.52	9.36	10.46
0-	10.96	12.89	11.57	13.86
0-	12.80	13.72	12.04	14.78
4-	17.79	15.72	15.46	16.80
4-	18.89	16.80	15.95	18.04

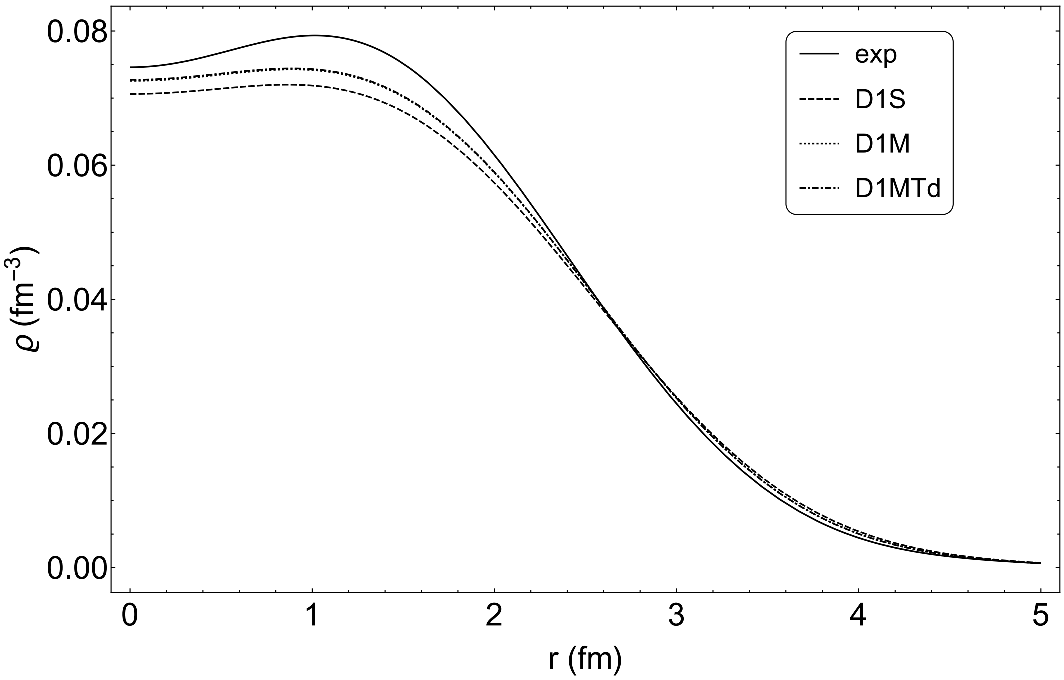

Figure 3.2: Charge distribution and experimental data.

3.5 Excitation levels

In our calculations we use a traditional RPA approach where the single particle configuration space is generated by defining an integration box where the single particle wave functions are bound. We call Discrete RPA (DRPA) this type of calculations. On the opposite the Continuum RPA (CRPA) calculations properly consider the fact that single particle wavefunctions with positive energy have oscillating behaviour at the boundaries.

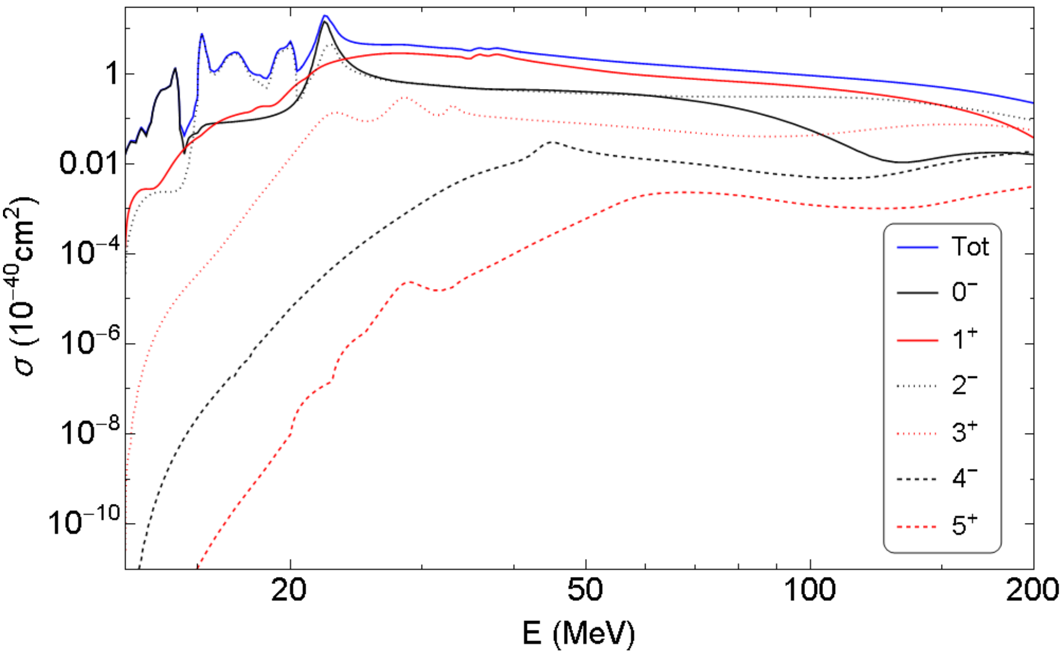

Figure 3.3: Axion absorption cross sections for different multipolarities and total cross section with D1M interaction and $f_a = 10^6$ GeV.

The CRPA approach can be used only for those excitation energies above the nucleon emission threshold. We combine the results of the two calculations to have the full spectrum.

We have calculated excited unnatural parity multipoles up to $J = 5$, but those $J^\pi = 0^-, 1^+, 2^-$ are largely dominant on the other ones. The results of the CRPA calculations for the first six multipolarities of the cross section with D1M interactions are shown in Fig. (3.3).

In Fig. (3.4)-(3.6) we show the axion cross sections for the first three multipolarities (0^-, 1^+,2^-) evaluated with D1MTd and D1S interactions. The most important features are preserved for all the three interactions. In the 0^- multipole the cross section with the D1MTd interaction has a pronunced peak near 12 MeV absent in the calculations with the other interactions. This is because the 0^- state is very sensitive to the presence of a tensor term in the D1MTd interaction potential. Experimentally, a 0^- state in the ^{16}O nucleus has been identified at about 11 MeV. In general, the D1S interaction shifts the cross sections to higher energies. A further confirmation of our results can be obtained from the comparison of axion and photon cross sections. A photon cannot excite the 0^- multipole, but we can analyze the other multipolarities. Fig. (3.7)-(3.8) show the photon cross sections for the 1^+ and 2^- multipolarities computed with different nuclear interactions. The energy of the excited levels is very similar for both axions and photons, as it should be. In fact, even if the incident particles and the interactions are different, the target nucleus and the available excited levels are the same.

In Fig. (3.9) we show the results for 0^-. The first two excitation levels below 15 MeV are slightly different from the CRPA. The peak between 20 MeV and 25 MeV is a result of the RPA three peaks summed toghether. The last two RPA points could be an artifact caused by the discretization of the continuum space, in fact the CRPA has no signs of these levels. The relevant excited levels for the 0^- multipole are:

$$\begin{aligned}
E &= 12.93\,\mathrm{MeV} \quad \sigma = 0.5 \times 10^{-40}\,\mathrm{cm}^2 \\
E &= 13.77\,\mathrm{MeV} \quad \sigma = 0.575 \times 10^{-40}\,\mathrm{cm}^2 \\
E &= 22.20\,\mathrm{MeV} \quad \sigma = 15.87 \times 10^{-40}\,\mathrm{cm}^2 \ .
\end{aligned}$$

In the case of multipole 1^+ in Fig. (3.10), the excited states indicate the presence of a wide resonance. This is mainly due to the configurations $(2p_{3/2} \otimes 1p_{3/2})$ for both protons and neutrons. The $2p_{3/2}$ single particle levels are wide resonances in the continuum for this reason we indicate the peak of the resonance. In conclusion, the relevant level for the 1^+ multipole is:

$$E = 28.00\,\mathrm{MeV} \quad \sigma = 3.1 \times 10^{-40}\,\mathrm{cm}^2 \ .$$

The situation for the 2^- in Fig. (3.11) is more complicated since discrete particle states are involved and also in the continuum the single particle states have relatively narrow widths. The first two excites states are below the nucleon emission threshold and they are taken from the DRPA results. They are dominated by the $(2d_{5/2} \otimes 1p_{1/2})$ proton and neutron configurations. In our model the neutron and proton $2d_{5/2}$ states are bound. The other energies we indicate correspond to the peaks of the CRPA calculations, also supported by the DRPA.

$$\begin{aligned}
E &= 9.55\,\mathrm{MeV} \quad \sigma = 2.52 \times 10^{-40}\,\mathrm{cm}^2 \\
E &= 11.20\,\mathrm{MeV} \quad \sigma = 3.47 \times 10^{-40}\,\mathrm{cm}^2 \\
E &= 15.20\,\mathrm{MeV} \quad \sigma = 8.47 \times 10^{-40}\,\mathrm{cm}^2 \\
E &= 16.80\,\mathrm{MeV} \quad \sigma = 3.02 \times 10^{-40}\,\mathrm{cm}^2 \\
E &= 20.00\,\mathrm{MeV} \quad \sigma = 5.07 \times 10^{-40}\,\mathrm{cm}^2 \\
E &= 22.60\,\mathrm{MeV} \quad \sigma = 4.85 \times 10^{-40}\,\mathrm{cm}^2 \ .
\end{aligned}$$

Since neutrinos and axions cannot be experimentally distinguished, we calculated the ν and $\overline{\nu}$-^{16}O neutral current (NC) cross section for the excited ^{16}O levels with the DRPA. The NC cross section are almost flavor-independent, therefore we consider a generic ν and $\bar{\nu}$. The difference between flavors is in the incident neutrino flux. In fact the neutrino-oxygen NC cross section depends from the incident neutrino energy. Fig. (3.12) shows a comparison between ν_x and $\bar{\nu}_x$ cross sections (convoluted with the ν_x and $\bar{\nu}_x$ fluxes).

3.5.1 Excited levels decay

For the calculation of the axion and neutrino induced emission spectra of ^{16}O a two-step approach was adopted, similar to the ones chosen in [Eng90, Lan95]. In a first step, the population of excited states in ^{16}O by axions or neutrinos was calculated in a RPA approach. In the second step the de-excitation of the excited ^{16}O is treated in a separate calculation as described below.

Excited states in ^{16}O decay at least via γ-emission. For states above the particle separation energies, the decay is dominated by particle emission. In the calculation, emissions of neutrons, protons, α-particles, and photons (γ-rays) were considered. This is similar to the approach used in [Lan95]. The relative transmission into the four channels was computed using the methods implemented in the SMARAGD Hauser-Feshbach reaction code [Rau15], with spin/parity-selection rules applied in the calculation of the energetically allowed transitions. Particle emission was treated by calculating transmission coefficients in an optical model, using the microscopic optical potential shown in [Jeu77, Lej80] for neutrons and protons, and the global optical potential used in [Mcf66] for α-particles. The γ-emission from an excited state was treated as described in [Rau00]. To obtain an appropriate γ-spectrum, the further de-excitation of populated excited states was followed additionally by considering a simple γ-cascade, not accounting for further particle emission during the cascade. The γ-branching probability at each excited state reached in the cascade was derived again from calculated relative γ-transmission coefficients.

Particle emission from excited states of ^{16}O can lead to particle bound or unbound states in the secondary nuclei ^{15}O, ^{15}N, and ^{12}C, respectively. In order to obtain the full particle and γ spectra, an iterative approach was adopted, including further particle and γ-emission from states in the secondary nuclides populated by the initial decay of states in ^{16}O . Again, emissions of neutrons, protons, α-particles, and photons were taken into account and γ-cascades in the secondary nuclides were followed. With the given initial ^{16}O excitation by axions and neutrinos, tertiary particle emission is negligible and therefore was not included. Simple γ-emission to the ground state was assumed for the de-excitation of the final, tertiary nuclides.

A main difference between axion and neutrino excitation of ^{16}O is that neutrinos excite isospin $T = 1$ configurations [Lan95] whereas axions excite states with $T = 0$ [Eng90]. This results in an isospin suppression of α-emission from neutrino induced states in ^{16}O even when it would be energetically allowed and favorable. Transmission coefficients obtained from an optical model do not consider isospin. Therefore the approach described in [Lan95] was followed and all γ-transmission coefficients were divided by a factor of 100, as suggested in [Kol92]. This leads to one major difference in the spectra induced by neutrinos and by axions: in the neutrino spectra α-emission from ^{16}O and thus also the production and decay of ^{12}C is strongly suppressed.

For the total spectra, all emissions of a particle type or of photons from all nuclides and all excited states were added. The information of separate primary and secondary emissions is separately stored in our output files and available on request (for example, if a detector would be able to discriminate between such primary and secondary events).

Using the neutrino and axion fluxes in Chap. 2 and the cross sections introduced in this Chapter[2], we calculated the ^{16}O emission spectra. Fig. (3.13)-(3.16) show the photon events in a 374 kton Cherenkov detector, like Hyper-Kamiokande (see Chap. 4 for details on this calculation), from a galactic SN at distance $d = 10\,\mathrm{kpc}$. The $\nu\,^{16}\mathrm{O} \to \gamma\nu\,^{16}\mathrm{O}$ and $\bar{\nu}\,^{16}\mathrm{O} \to \gamma\bar{\nu}\,^{16}\mathrm{O}$ processes produce photons in the energy range $[0; 12]\,\mathrm{MeV}$ as shown in Fig. (3.13)-(3.14). Instead, the $a\,^{16}\mathrm{O} \to \gamma\,^{16}\mathrm{O}$ absorption processes produce photon events in the energy range $[5; 10]\,\mathrm{MeV}$ [Fig. (3.15)-(3.16)]. Fig. (3.17)-(3.20) show the number of neutron events. The $\nu\,^{16}\mathrm{O} \to n\nu\,^{15}\mathrm{O}$ and $\overline{\nu}\,^{16}\mathrm{O} \to n\overline{\nu}\,^{15}\mathrm{O}$ processes emit neutrons in the energy range $[0; 4]\,\mathrm{MeV}$ [Fig. (3.17)-(3.18)]. The $a\,^{16}\mathrm{O} \to n\,^{15}\mathrm{O}$ absorption processes produce the majority of neutrons in the energy range $[0; 7]\,\mathrm{MeV}$ [Fig. (3.19)-(3.20)].

[2]For neutrinos we use a cross section for the $\nu\,^{16}\mathrm{O} \to \nu\,^{16}\mathrm{O}^*$ obtained with a similar procedure.

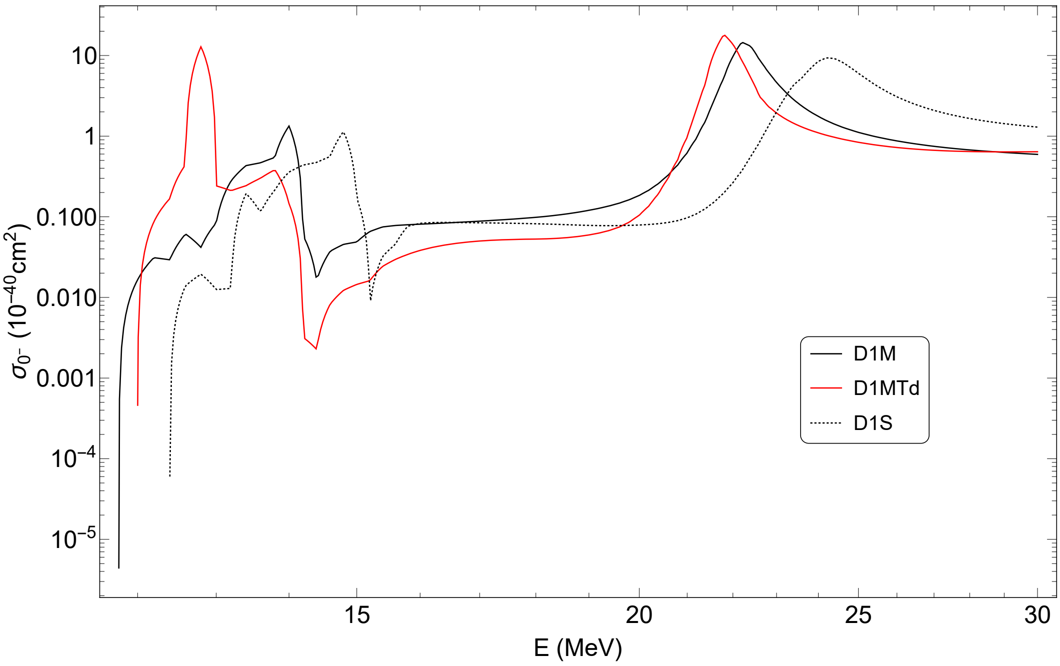

Figure 3.4: Axion cross sections with different interactions for $J^P = 0^-$ with $f_a = 10^6\,\text{GeV}$.

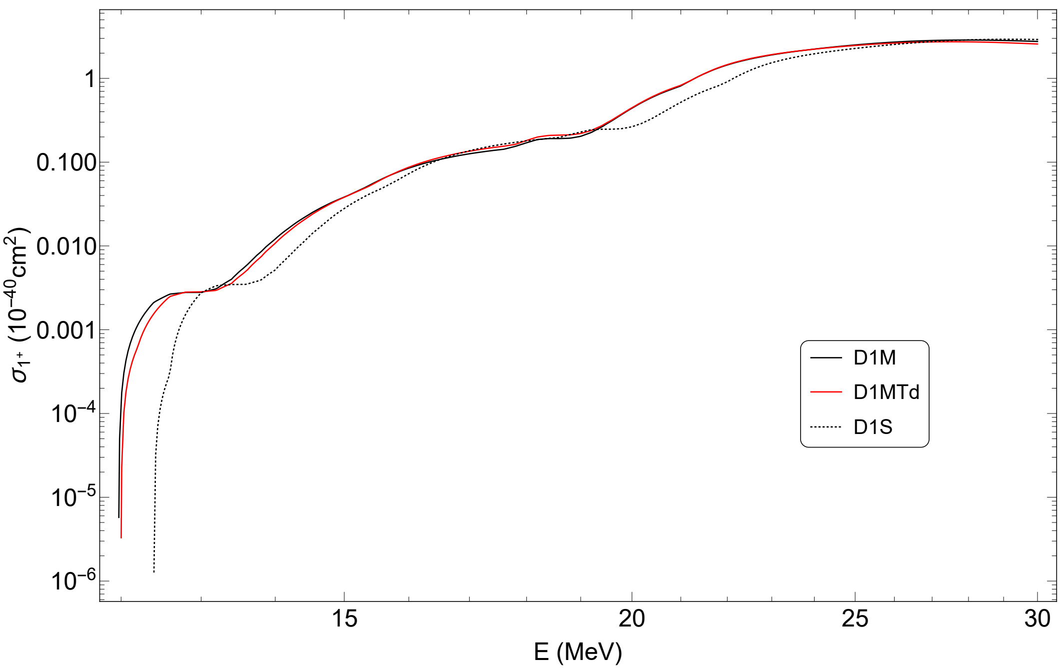

Figure 3.5: Axion cross sections with different interactions for $J^P = 1^+$ with $f_a = 10^6\,\text{GeV}$.

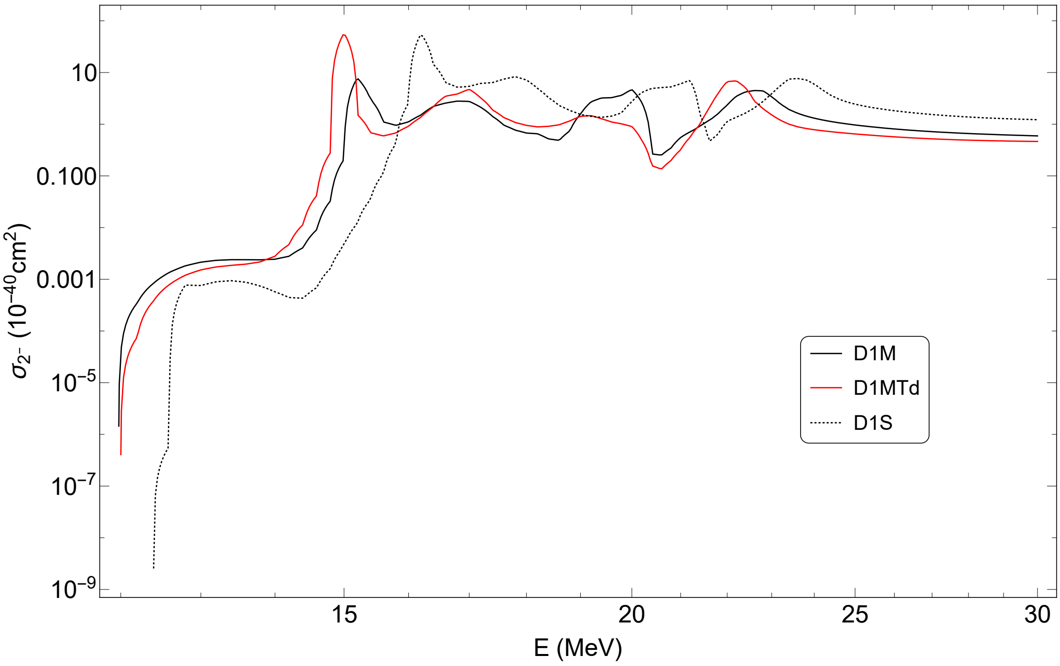

Figure 3.6: Axion cross sections with different interactions for $J^P = 2^-$ with $f_a = 10^6\,\text{GeV}$.

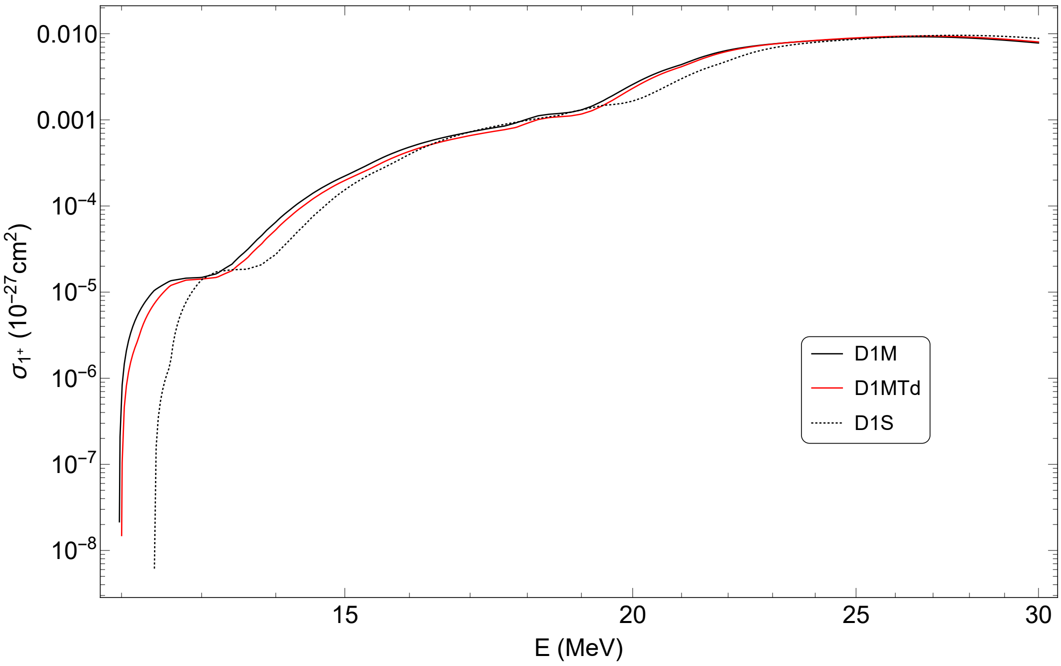

Figure 3.7: Total photon absorption cross sections with different interactions for $J^P = 1^+$.

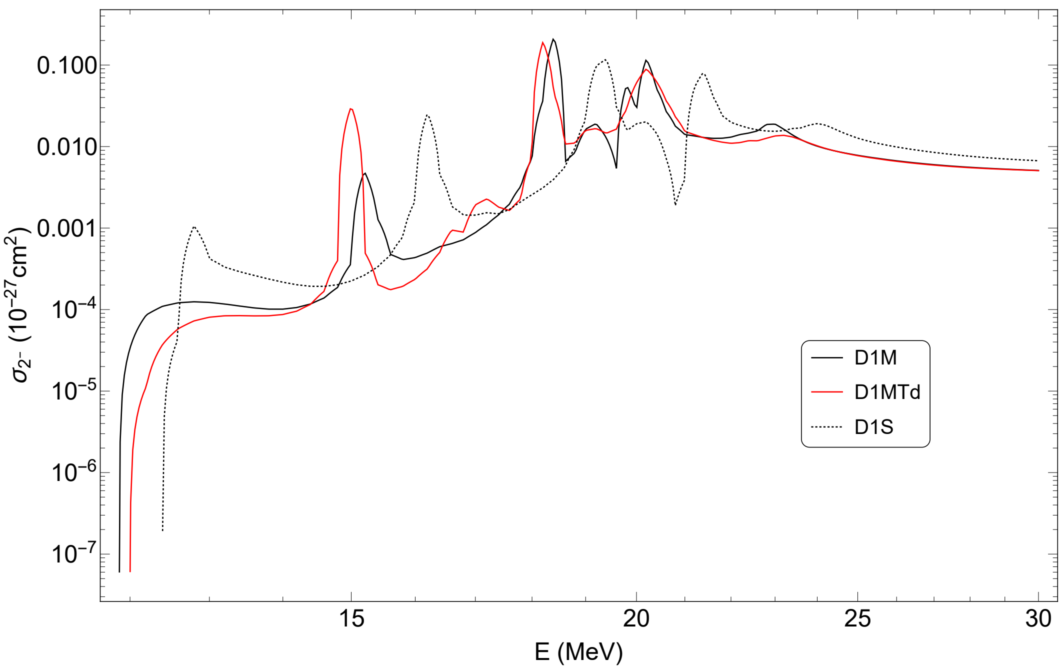

Figure 3.8: Total photon absorption cross sections with different interactions for $J^P = 2^-$.

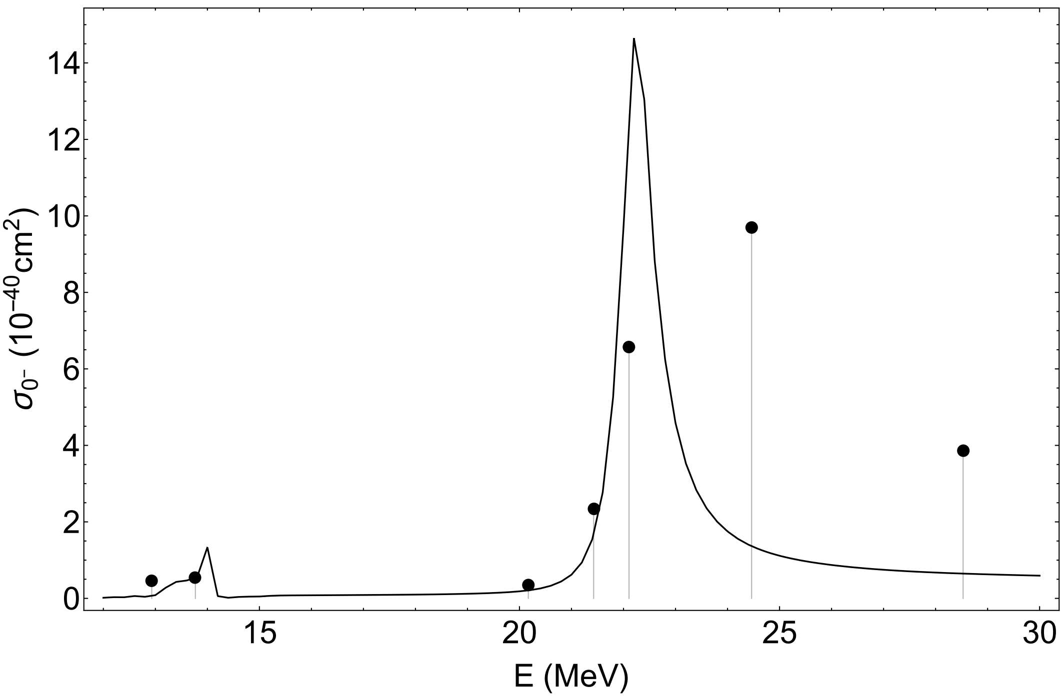

Figure 3.9: DRPA vs CRPA: $J^P = 0^-$ cross section with $f_a = 10^6\,\mathrm{GeV}$.

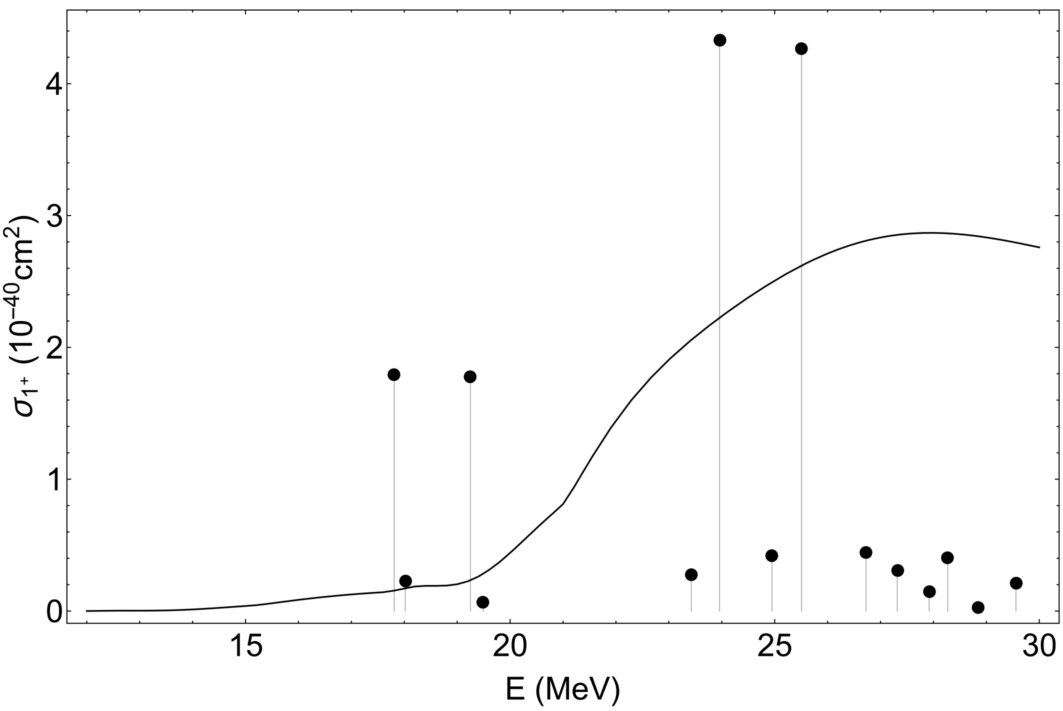

Figure 3.10: DRPA vs CRPA: $J^P = 1^+$ cross section with $f_a = 10^6\,\mathrm{GeV}$.

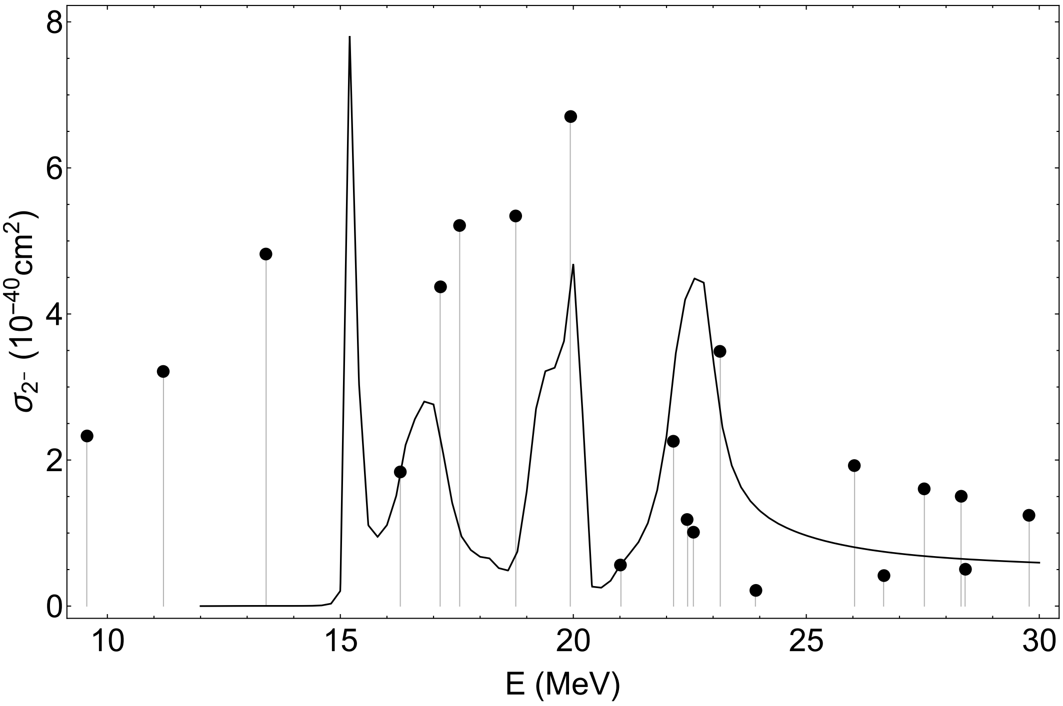

Figure 3.11: DRPA vs CRPA: $J^P = 2^-$ cross section with $f_a = 10^6\,\mathrm{GeV}$.

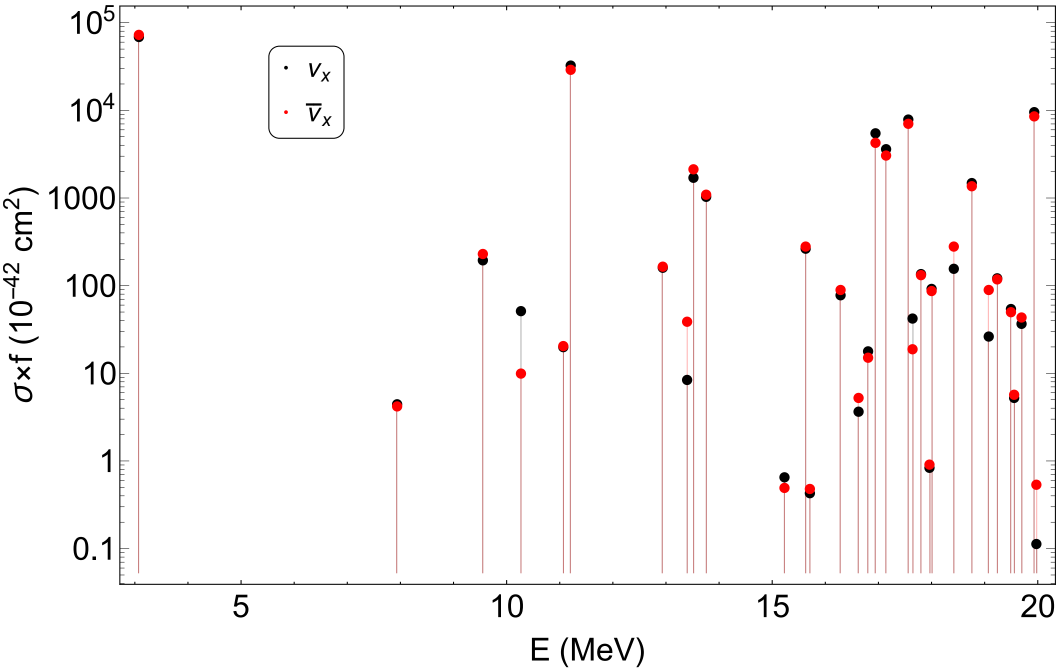

Figure 3.12: DRPA: ν_x and $\bar{\nu}_x$ excited levels cross sections convoluted with the unperturbed ($g_{ap} = g_{an} = 0$) time-integrated neutrino fluxes (integrated over $[0.7; 10]$ s).

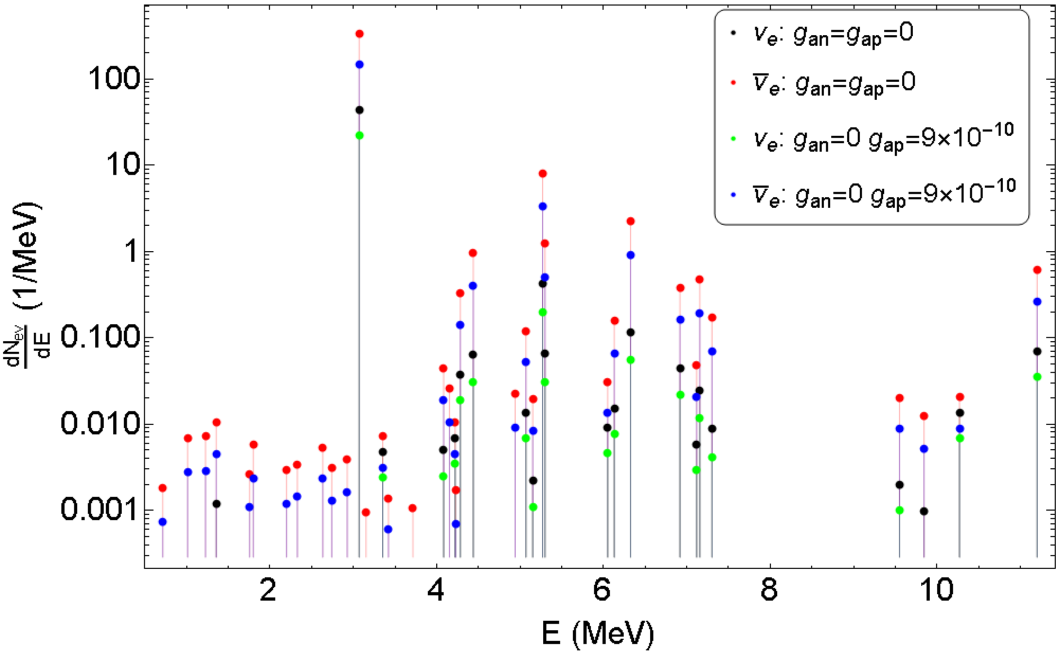

Figure 3.13: Number of photon events produced by ν_e and $\overline{\nu}_e$ NC nuclear interactions for a SN at $d = 10\,\text{kpc}$ and a detector mass $M = 374\,\text{kton}$ with $g_{ap} = g_{an} = 0$ and $g_{ap} = 9 \times 10^{-10}$, $g_{an} = 0$.

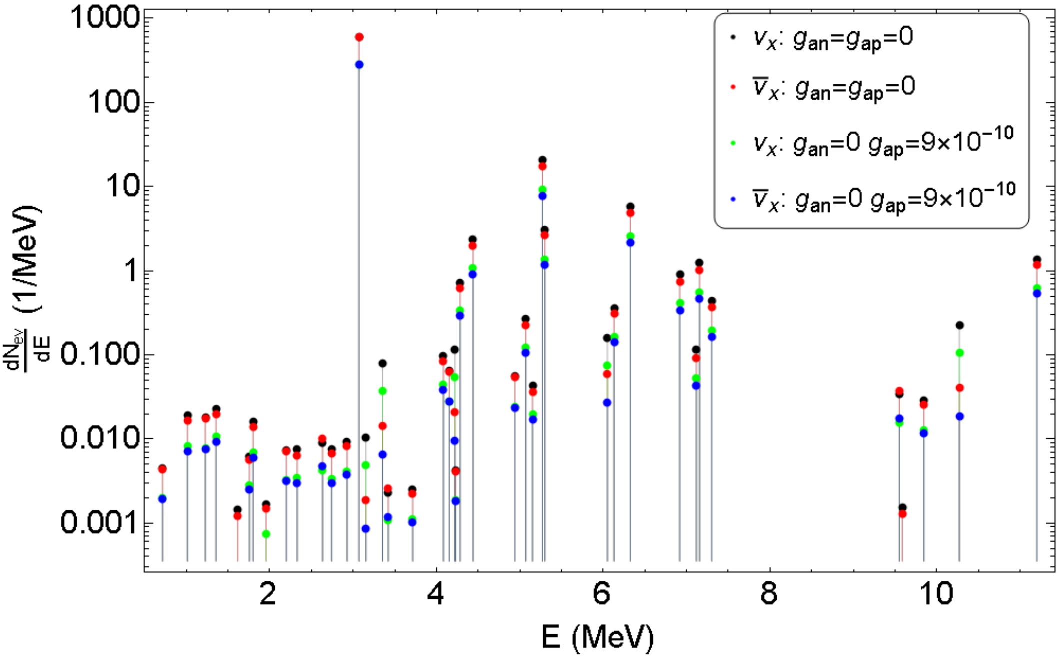

Figure 3.14: Number of photon events produced by ν_x and $\overline{\nu}_x$ NC nuclear interactions for a SN at $d = 10\,\text{kpc}$ and a detector mass $M = 374\,\text{kton}$ with $g_{ap} = g_{an} = 0$ and $g_{ap} = 9 \times 10^{-10}$, $g_{an} = 0$.

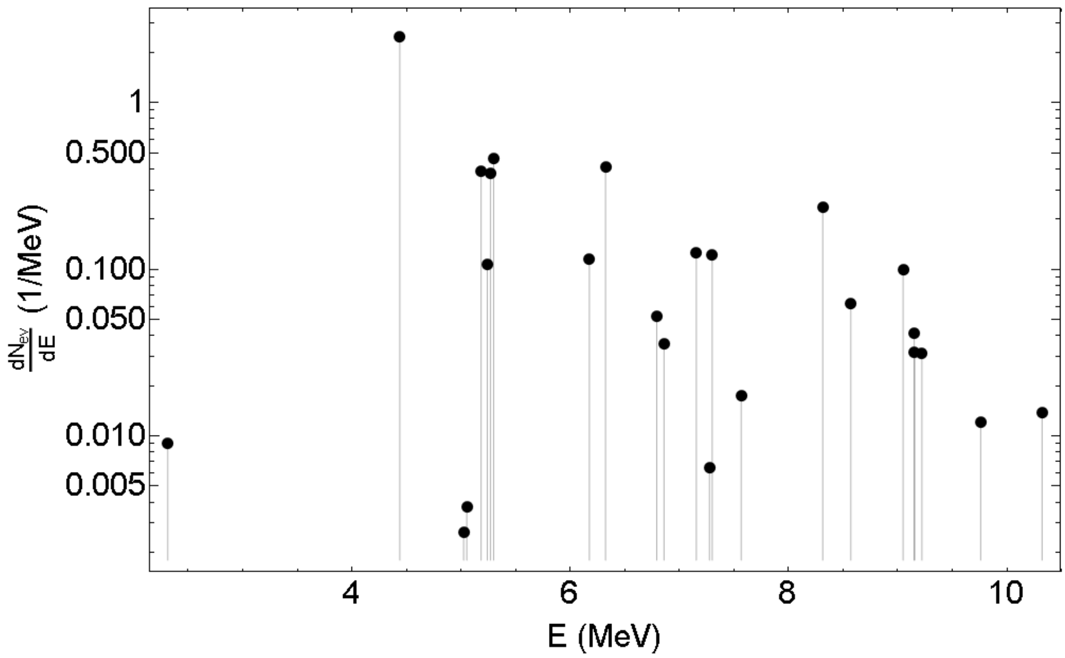

Figure 3.15: Number of photon events produced by axion nuclear absorption for a SN at $d = 10\,\mathrm{kpc}$ and a detector mass $M = 374\,\mathrm{kton}$ with $g_{ap} = 9 \times 10^{-10}$, $g_{an} = 0$.

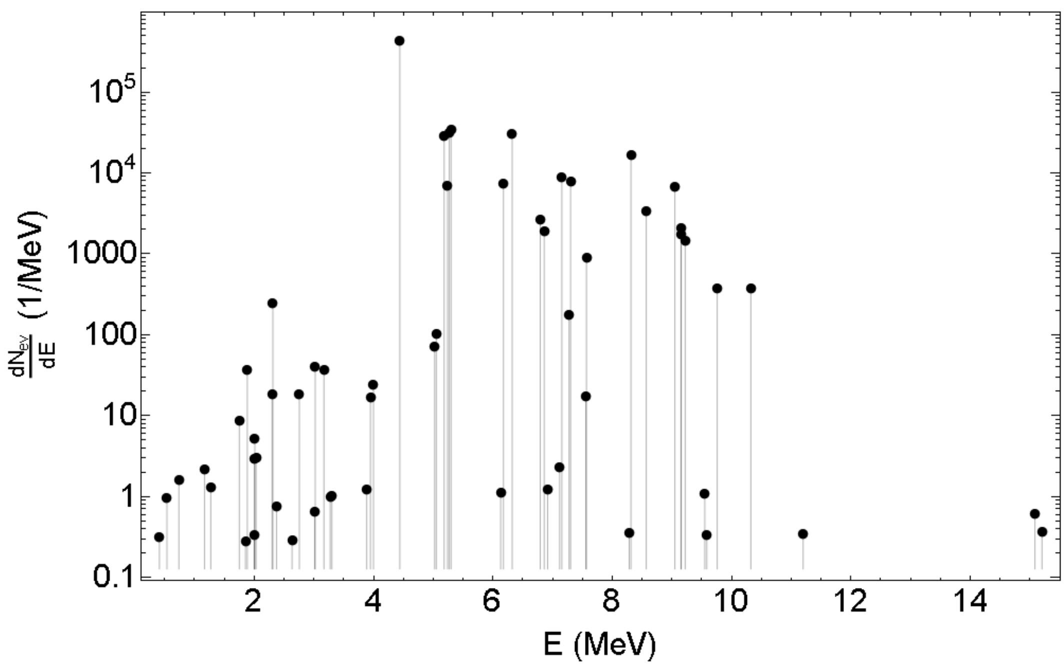

Figure 3.16: Number of photon events produced by axion nuclear absorption for a SN at $d = 10\,\mathrm{kpc}$ and a detector mass $M = 374\,\mathrm{kton}$ with $g_{ap} = g_{an} = 10^{-6}$.

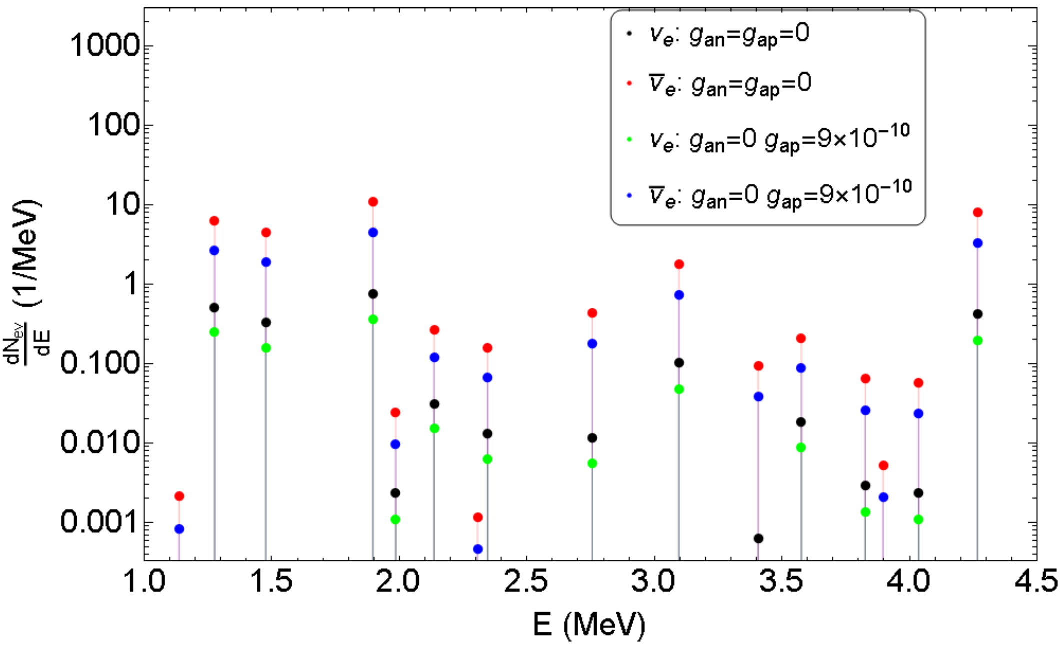

Figure 3.17: Number of neutron events produced by ν_e and $\overline{\nu}_e$ NC nuclear interactions for a SN at $d = 10\,\mathrm{kpc}$ and a detector mass $M = 374\,\mathrm{kton}$ with $g_{ap} = g_{an} = 0$ and $g_{ap} = 9 \times 10^{-10}$, $g_{an} = 0$.

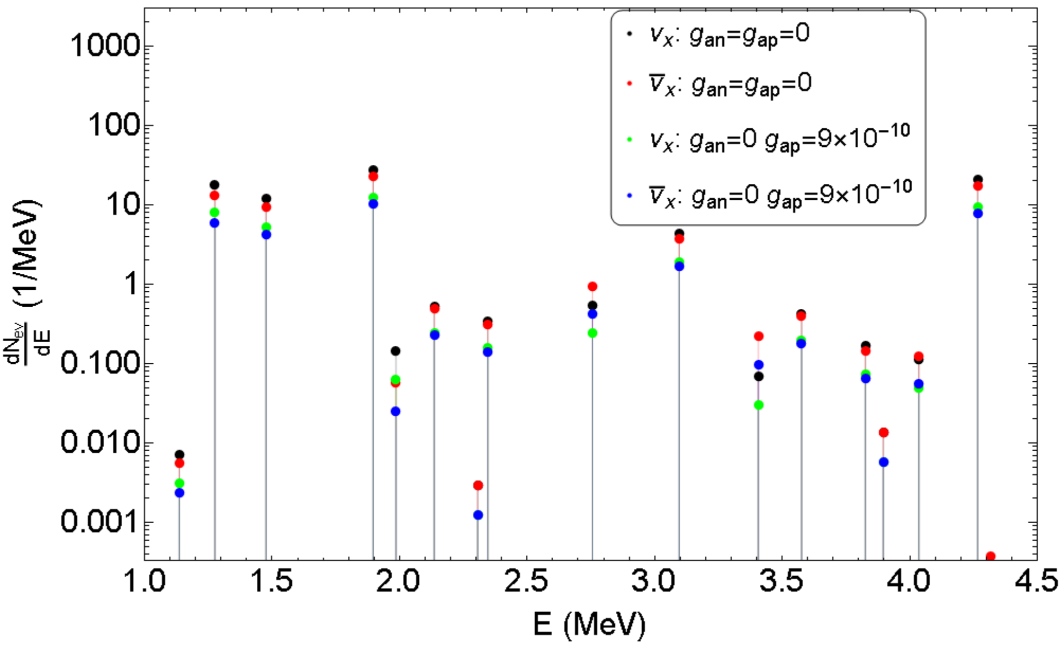

Figure 3.18: Number of neutron events produced by ν_x and $\overline{\nu}_x$ NC nuclear interactions for a SN at $d = 10\,\mathrm{kpc}$ and a detector mass $M = 374\,\mathrm{kton}$ with $g_{ap} = g_{an} = 0$ and $g_{ap} = 9 \times 10^{-10}$, $g_{an} = 0$.

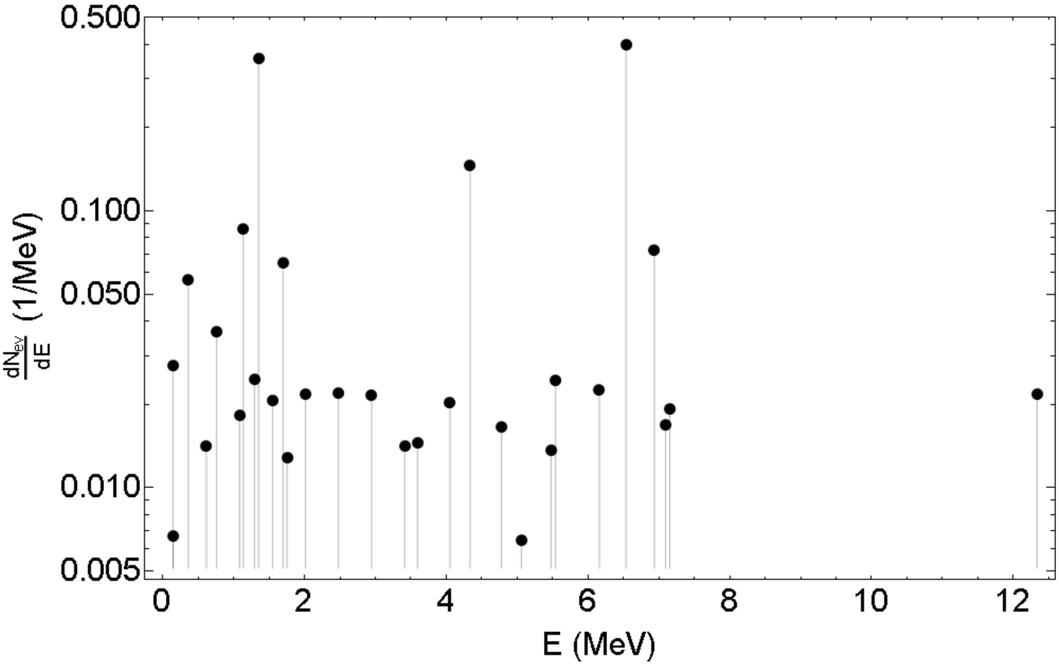

Figure 3.19: Number of neutron events produced by axion nuclear absorption for a SN at $d = 10\,\mathrm{kpc}$ and a detector mass $M = 374\,\mathrm{kton}$ with $g_{ap} = 9 \times 10^{-10}$, $g_{an} = 0$.

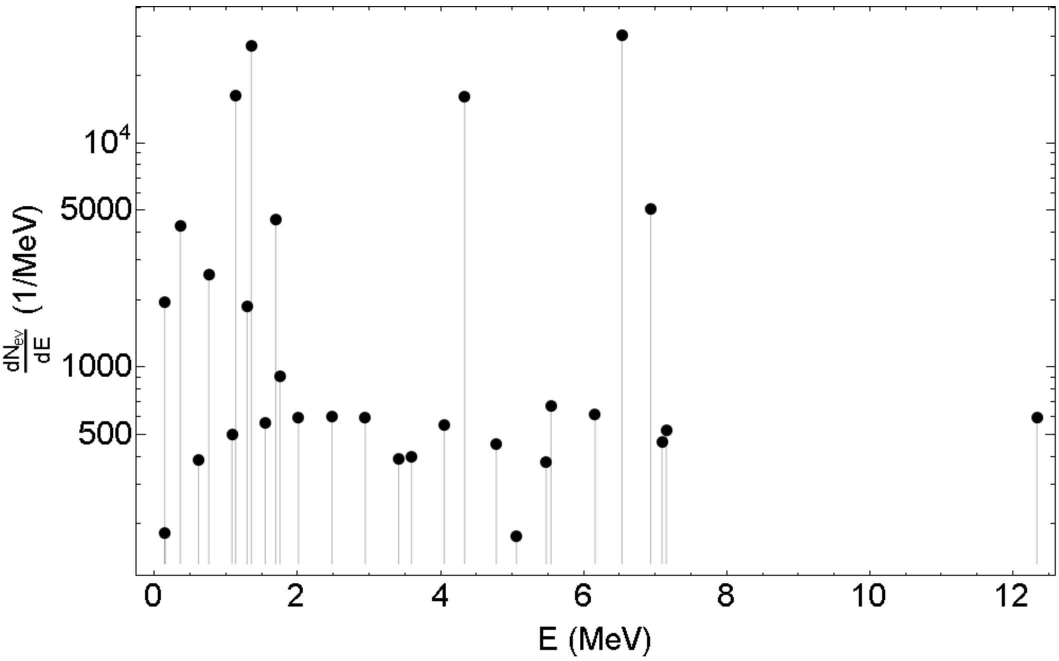

Figure 3.20: Number of neutron events produced by axion nuclear absorption for a SN at $d = 10\,\mathrm{kpc}$ and a detector mass $M = 374\,\mathrm{kton}$ with $f_a = 10^6\,\mathrm{GeV}$.

Chapter 4

Detection of a SN axion signal

In this Chapter we calculate the SN neutrino and axion signal in a future Mton-scale water Cherenkov detector. In Sec. 4.1 we discuss some detector properties and the calculation of the detected events. Sec. 4.2 briefly summarizes how neutrino flavor conversions would affect the detected neutrino fluxes. In Sec. 4.3 we list the neutrino processes in a water Cherenkov detector. Sec. 4.4 deals with the free-streaming axion signal. We discuss how to reduce the neutrino background to enhance the axion detectability and future perspectives on the detailed calculation of the axion flux. In conclusion, in Sec. 4.5 we calculate the axion signal in the trapping regime.

4.1 Detector features and setup of events calculation

In this Thesis we will focus on a next-generation Mton-class water Cherenkov detector to study the sensitivity to the SN axion signal. Water Cherenkov detectors employ water as detection material. Optical-frequency Cherenkov radiation from charged particles moving faster than light in water is collected by photomultiplier tubes. Among detectors running at the time of this Thesis, Super-Kamiokande will collect the largest number of individually-reconstructed SN neutrino events. Super-Kamiokande is a 50-kton water Cherenkov detector in Japan, located in the Kamioka mine at 1000 meters underground [Ike07]. The proposed next-generation large water Cherenkov detector is Hyper-Kamiokande, with $M = 374\,\mathrm{kton}$ of fiducial mass [Abe11]. We will take

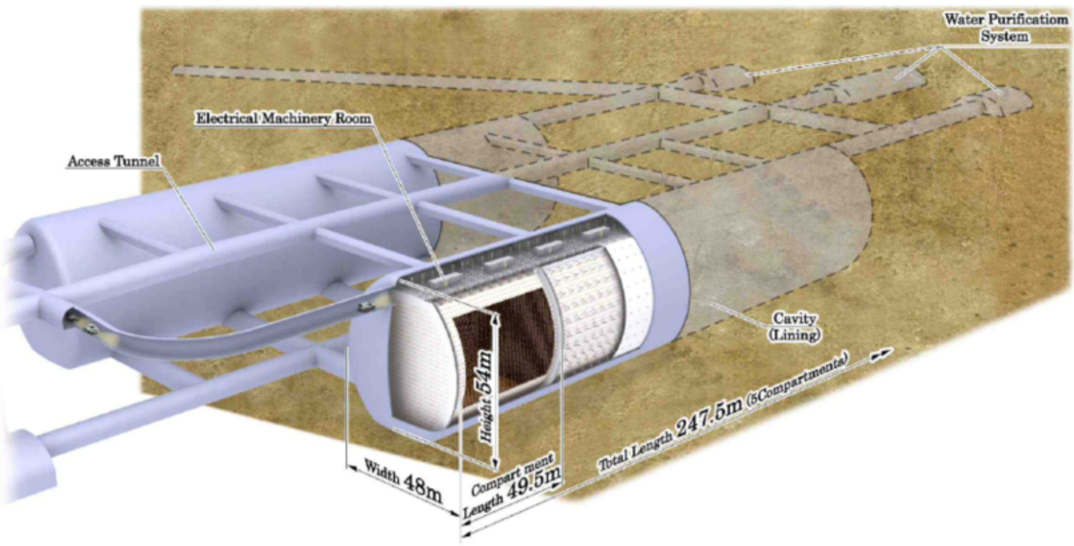

Figure 4.1: Schematic view of the Hyper-Kamiokande detector. (Figure taken from [Abe11]).

Hyper-Kamiokande as reference detector for our following discussion. Fig. (4.1) shows a schematic view of the Hyper-Kamiokande detector.

The detected neutrino (or axion) events in the proposed detector are calculated as [Fis16]

$$N_{\rm ev} = F \otimes \sigma \otimes \mathcal{R} \otimes \mathcal{E} \; ; \tag{4.1}$$

where F, the neutrino (or axion) flux, is convoluted with the cross section σ in the detector, the detector energy resolution $\mathcal{R}$ and the detector efficiency $\mathcal{E}$. We assume $\mathcal{E} = 1$ above the energy threshold. Explicitly Eq. (4.1) can be written as [Lun04]

$$\frac{dN}{d\epsilon} = N_{\rm T} \int_{E_{\rm th}}^{+\infty} d\epsilon' \, \mathcal{R}(\epsilon, \epsilon') \int dE \, F(E) \frac{d\sigma}{d\epsilon'}(\epsilon', E) \; ; \tag{4.2}$$

where ϵ and ϵ' are respectively the observed and true energies of the detectable particles; $N_{\rm T}$ is the number of targets in the detector; the detector efficiency is 1 above the energy threshold $E_{\rm th} = 5\,\text{MeV}$ and the energy resolution, $\mathcal{R}$, is defined as [Fog04]

$$\mathcal{R}(\epsilon, \epsilon') = \frac{1}{\sqrt{2\pi\sigma_\epsilon^2}} \, e^{-\frac{(\epsilon-\epsilon')^2}{2\sigma_\epsilon^2}} \quad \sigma_\epsilon = 0.6\sqrt{\epsilon/\,\text{MeV}} \; ; \tag{4.3}$$

as for the Super-Kamiokande detector. The number of targets is calculated as

$$N_{\mathrm{T}} = q\frac{M(\mathrm{kton}) \times 10^9}{M_{\mathrm{mol}}} \times N_{\mathrm{A}} \; ; \tag{4.4}$$

where M is the detector mass expressed in kton; M_{mol} is the molar weight of the target molecule expressed in g / mol; $N_{\mathrm{A}} = 6.022 \times 10^{23}$ is the Avogadro's number and q is the number of targets per molecule e.g. in water, if the target is the oxygen nucleus $q = 1$, if the targets are the protons $q = 2$. The neutrino (or axion) flux is defined as

$$F(E) = \frac{1}{4\pi d^2} N_0 f(E) \; ; \tag{4.5}$$

where N_0 is the total number of neutrinos (or axions) emitted from the SN; d is the distance of the SN and $f(E)$ is the energy distribution of the emitted neutrinos (or axions) normalized to 1.

4.2 Oscillated neutrino fluxes

The neutrino fluxes emitted from the SN core and discussed in Chap. 2 can be peculiarly modificated by *flavor oscillations* effects occurring in their propagation to the Earth. In the following we assume a standard three-neutrino framework scenario [Cap18]. The neutrino masses are indicated as m_i $i = 1, 2, 3$, ordered as $m_1 < m_2 < m_3$, "normal hierarchy" (NH); or $m_3 < m_1 < m_2$, "inverted hierarchy" (IH). The neutrino mass spectrum is parametrized in terms of two mass squared differences [Cap18]

$$\begin{aligned} \Delta m^2_{32} &= m^2_3 - m^2_{1,2} = 2.45 \times 10^{-3}\,\mathrm{eV}^2 \; ; \\ \Delta m^2_{21} &= m^2_2 - m^2_1 = 7.34 \times 10^{-5}\,\mathrm{eV}^2 \; . \end{aligned} \tag{4.6}$$

The sign of Δm^2_{32} distinguishes the NH, $\Delta m^2_{32} > 0$, or the IH, $\Delta m^2_{32} < 0$. The unitary matrix which transforms the mass eigenstates into flavor eigenstates, the Pontecorvo-Maki-Nakagawa-Sakata (PMNS) matrix, is characterized by three neutrino mixing angles [Cap18]:

$$\begin{aligned} \sin^2\theta_{12} &= 0.304 \; ; \\ \sin^2\theta_{13} &= 0.0214 \; ; \\ \sin^2\theta_{23} &= 0.551 \; . \end{aligned} \tag{4.7}$$

In the following we neglect the effect of θ_{23} since we assume that the ν_μ and ν_τ fluxes are equal.

Assuming that during the cooling phase, neutrino fluxes are processed by the only Mikheyev-Smirnov-Wolfenstein matter effect, the oscillated neutrino fluxes are given by [Mir16]

$$\begin{aligned} F_{\nu_e} &= F^0_{\nu_x} \ ; \\ F_{\bar{\nu}_e} &= \cos^2\theta_{12}(F^0_{\bar{\nu}_e} - F^0_{\nu_e}) + F^0_{\nu_x} \ ; \end{aligned} \tag{4.8}$$

for NH, and

$$\begin{aligned} F_{\nu_e} &= \sin^2\theta_{12}(F^0_{\bar{\nu}_e} - F^0_{\nu_x}) + F^0_{\nu_x} \ ; \\ F_{\bar{\nu}_e} &= F^0_{\nu_x} \ ; \end{aligned} \tag{4.9}$$

for IH; where F^0_ν and F_ν indicate respectively the original neutrino fluxes and the fluxes that reach our detector. The other fluxes are calculated using the total flux conservation [Mir16]:

$$F^0_{\nu_e} + 2F^0_{\nu_x} = F_{\nu_e} + 2F_{\nu_x} \ . \tag{4.10}$$

Only charged current processes will be affected from neutrino oscillations: the neutral current ones are flavor-blind.

4.3 Neutrino interaction cross sections and events rate

In a water Cherenkov detector the SN neutrinos reactions are [Raf96]:

- $\bar{\nu}_e p \rightarrow n e^+$: the inverse beta decay (IBD) on free protons;
- $\nu e^- \rightarrow \nu e^-$: the elastic scattering (ES) on electrons (ν means neutrinos and anti-neutrinos of any flavor);
- charged (O-CC) and neutral current (O-NC) interactions on oxygen nuclei.

An approximate form for the IBD cross section is [Str06]

$$\begin{aligned} \sigma(E) = &\exp(-0.07x + 0.02x^2 - 0.002x^4)\times \\ &\left(\frac{E}{\mathrm{MeV}} - 1.293\right)^2 \theta\left(\frac{E}{\mathrm{MeV}} - 1.293\right) \times 10^{-43}\,\mathrm{cm}^2 \ ; \end{aligned} \tag{4.11}$$

where $x = \ln(E/\,\mathrm{MeV})$.

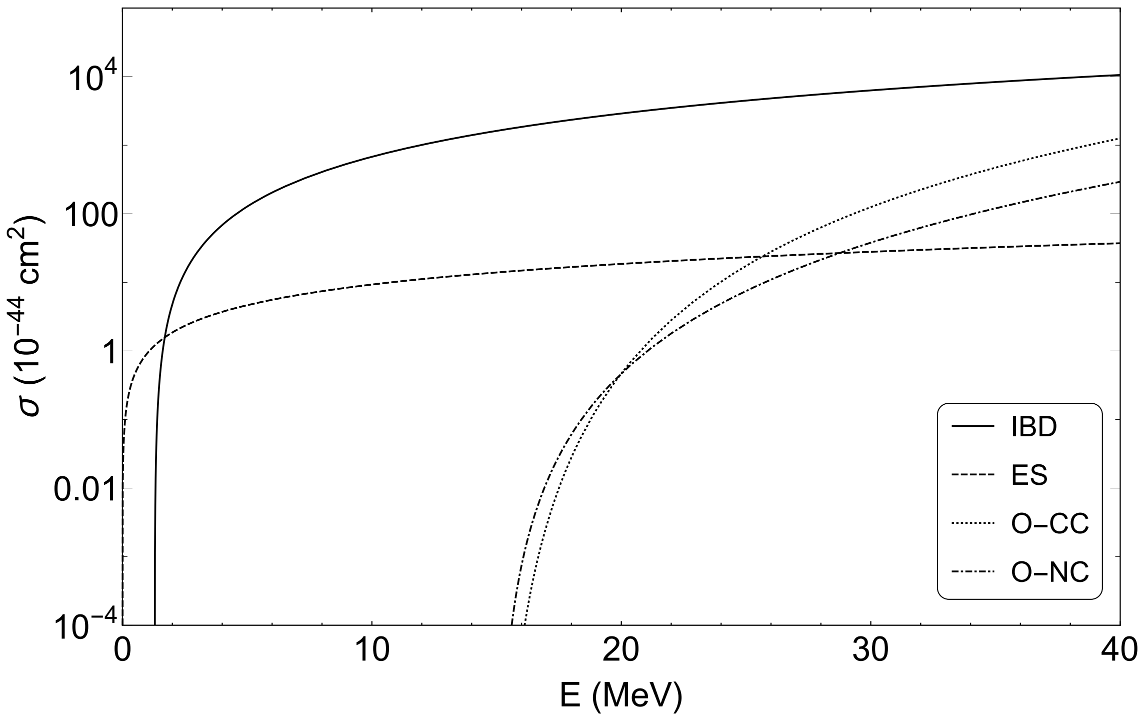

Figure 4.2: Neutrino interaction cross sections for processes in a water Cherenkov detector. The IBD is the dominant reaction.

The neutrino electron ES cross section can be parametrized by [For13]

$$\frac{d\sigma(E_{\nu,j})}{dy} = \frac{2G_F^2}{\pi} m_e E_\nu \left[g_j^2 + g_j'^2 (1-y)^2 - g_j g_j' \frac{m_e}{E_\nu} y \right] \quad j = \nu_e, \overline{\nu}_e, \nu_x \; ; \tag{4.12}$$

where $G_F = 1.166 \times 10^{-5}\,\mathrm{GeV}^{-2}$ is the Fermi constant; m_e is the electron mass; g_j and g_j' are the neutrino coupling constants in Tab. (4.1); $\sin^2\theta_W = 0.229$ is the Weinberg angle [Pat16] and

$$0 < y = (E_e - m_e)/E_\nu < (1 + m_e/2E_\nu)^{-1} \; . \tag{4.13}$$

The O-CC process $\nu_e\,{}^{16}\mathrm{O} \to e^-\,{}^{16}\mathrm{F}^*$ cross section can be approximated by [Lah13]

$$\sigma(E) = 4.7 \times 10^{-40} (E^{0.25} - 15^{0.25})^6\, \theta\left(\frac{E}{\mathrm{MeV}} - 15\right) \mathrm{cm}^2 \; . \tag{4.14}$$

The O-CC $\overline{\nu}_e\,{}^{16}\mathrm{O} \to e^+\,{}^{16}\mathrm{N}^*$ process cross section is approximated by

$$\sigma(E) = 4.99 \times 10^{-40} (E^{0.23} - 15^{0.23})^{4.61}\, \theta\left(\frac{E}{\mathrm{MeV}} - 15\right) \mathrm{cm}^2 \; . \tag{4.15}$$

Table 4.1: Constants used in the ES scattering cross section [Eq. (4.12)].

Species	g	g'
ν_e	$\frac{1}{2} + \sin^2\theta_W$	$\sin^2\theta_W$
$\overline{\nu}_e$	$\sin^2\theta_W$	$\frac{1}{2} + \sin^2\theta_W$
ν_x	$-\frac{1}{2} + \sin^2\theta_W$	$\sin^2\theta_W$
$\overline{\nu}_x$	$\sin^2\theta_W$	$-\frac{1}{2} + \sin^2\theta_W$

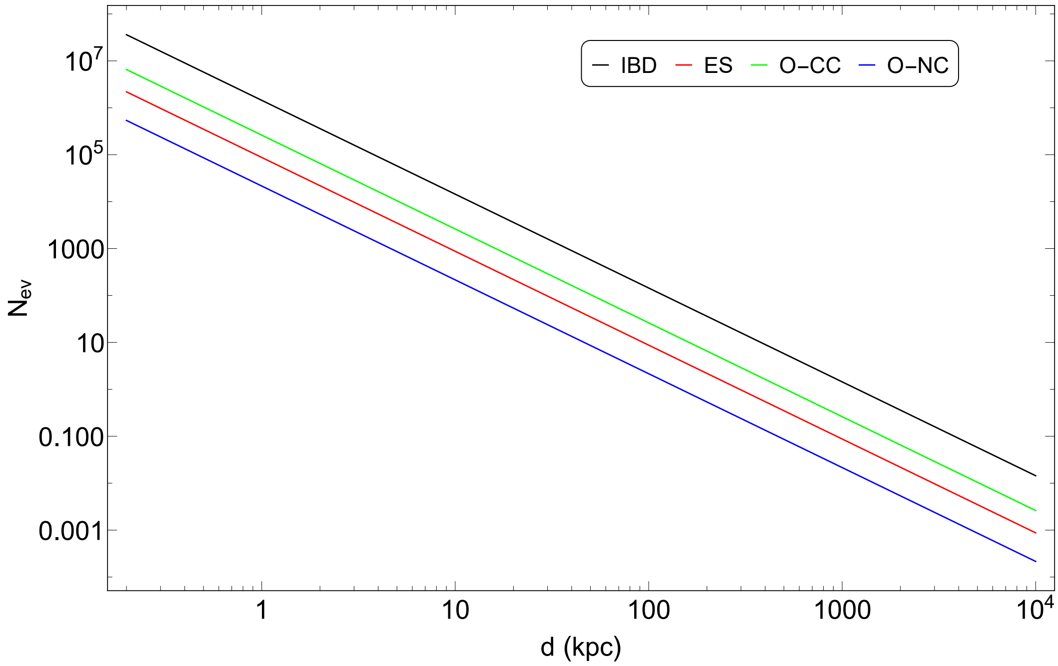

Figure 4.3: Neutrino events for the all detection channels as function of the SN distance for a water Cherenkov detector of mass $M = 374\,\mathrm{kton}$.

The total cross section from O-NC interactions summed over ν_x and $\bar{\nu}_x$ can be approximated by [Bea98]

$$\sigma(E) = 0.75\left(\frac{E}{\mathrm{MeV}} - 15\right)^4 \theta\left(\frac{E}{\mathrm{MeV}} - 15\right) \times 10^{-47}\,\mathrm{cm}^2\ ; \qquad (4.16)$$

even if in the following, for our detailed calculations, we will use RPA results, in analogy to the axion case. Fig. (4.2) shows the neutrino cross sections of the different processes described above.

Table 4.2: Number of neutrino events for a SN at $d = 10\,\mathrm{kpc}$ and a detector mass $M = 374\,\mathrm{kton}$ in the two neutrino mass hierarchies.

Interaction	Events NH	Events IH
IBD	1.44×10^4	1.88×10^4
ES ν_e	35	35
ES $\overline{\nu}_e$	80	80
ES $4\nu_x$	759	759
O-CC ν_e	1.82×10^3	1.32×10^3
O-CC $\overline{\nu}_e$	793	1.12×10^3
O-NC ν_e	2	2
O-NC $\overline{\nu}_e$	20	20
O-NC ν_x	44	44
O-NC $\overline{\nu}_x$	52	52

Based on the above cross sections we show the number of events in function of the distance assuming NH [Fig. (4.3)]. We realize that for a Mton scale detector the statistics will be excellent for a Galactic SN [Tab. (4.2)]. The IBD is the greatest source of events and gives a relevant number of events even at $30 - 40\,\mathrm{kpc}$ (~ 4000 events), the diameter of our galaxy. Also the ES events are numerous and usually are used to detect the direction of the source, because the scattered electron preserves the incident neutrino direction [Raf96, Tom03]. The photons produced by NC interactions with oxygen fall mostly in the energy range $[5; 10]\,\mathrm{MeV}$.

4.4 Axion event rate in the free-streaming regime

4.4.1 Axion events

In this Section we calculate the number of axion events in the free-streaming regime ($g_{ap} = 9 \times 10^{-10}$ and $g_{an} = 0$). The axion-oxygen absorption produce photons in the energy range $[5; 10]\,\mathrm{MeV}$ as shown in Fig. (4.4), where each discrete energy level has been convoluted with the energy resolution of the detector [Eq. (4.3)]. Therefore we restrict our attention to this specific window.

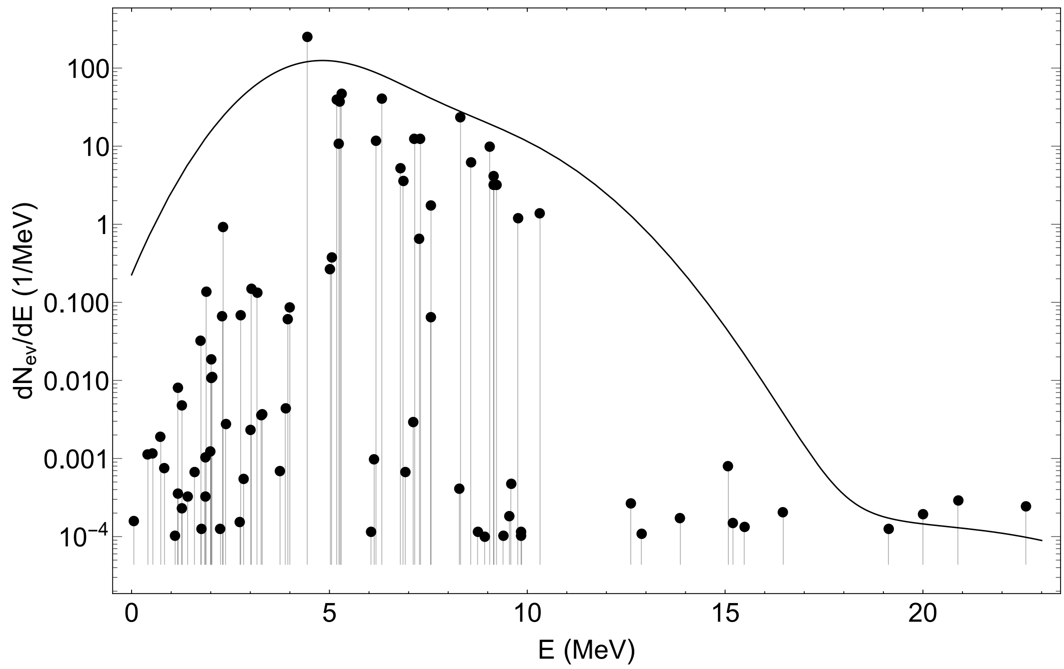

Figure 4.4: Photons produced by axion absorption for a SN at distance $d = 1\,\mathrm{kpc}$ and for a detector of mass $M = 374\,\mathrm{kton}$. The axion coupling constants are $g_{ap} = 9 \times 10^{-10}$ and $g_{an} = 0$.

As we observed in Chap. 2 the neutrino fluxes are modified by free-streaming axions [Tab. (4.3)]. Fig. (4.5) shows the neutrino and axion events for NH as function of distance of the SN. The number of axion and neutrino events in the energy window $[5; 10]\,\mathrm{MeV}$ are tabulated in Tab. (4.3) for both NH and IH. In order to enhance the SN axion signal we assumed a close-by SN at $d = 1\,\mathrm{kpc}$. We note that the differences between NH and IH are small. Then in the following, for definitiveness we will focus on NH. From Tab. (4.3) we understand that the axion signal is submerged by the huge neutrino backgrounds even for a nearby SN ($d = 1\,\mathrm{kpc}$). We will now discuss how would be possible to reduce the neutrino background.

Table 4.3: Number of neutrino events in the range [5; 10] MeV for a SN at $d = 1\,\mathrm{kpc}$ and a detector mass $M = 374\,\mathrm{kton}$ in the two neutrino mass hierarchies.

$g_{ap} = 9 \times 10^{-10}, g_{an} = 0$		
Interaction	Events NH	Events IH
a-O	270	270
IBD	$1.99{\times}10^5$	$2.39{\times}10^5$
ES ν_e	$1.99{\times}10^3$	$1.99{\times}10^3$
ES $\overline{\nu}_e$	$3.58{\times}10^3$	$3.58{\times}10^3$
ES $4\nu_x$	$2.97{\times}10^4$	$2.97{\times}10^4$
O-CC ν_e	$1.39{\times}10^3$	$1.39{\times}10^3$
O-CC $\overline{\nu}_e$	374	447
O-NC ν_e	99	99
O-NC $\overline{\nu}_e$	856	856
O-NC ν_x	$2.34{\times}10^3$	$2.34{\times}10^3$
O-NC $\overline{\nu}_x$	$1.79{\times}10^3$	$1.79{\times}10^3$

4.4.2 Background reduction

Inverse beta decay

The IBD is the most important neutrino background source for the axion signal. This process is sensitive to the $\overline{\nu}_e$ component of the flux and has an energy threshold of 1.293 MeV, the neutron-proton mass difference. The observable signal is given by the Cherenkov radiation of the produced positron.

A possible enhancement in identifying IBD events would be achieved if one can tag the neutron associated with the reaction in coincidence with the positron [Bea03, Lah13, Sch11]. In fact, a neutron needs about $200\,\mu$s to thermalize and to be captured by a free proton. Moreover, this neutron capture releases a 2.2 MeV photon. Unfortunately, this low energy photons cannot be detected because they are below the detector threshold. In order to improve the detectability of neutron captures, a Cherenkov detector can be doped with gadolinium (Gd). This element has a large neutron capture cross section and, after a neutron capture, emits a cascade of photons with a total energy of 8 MeV.

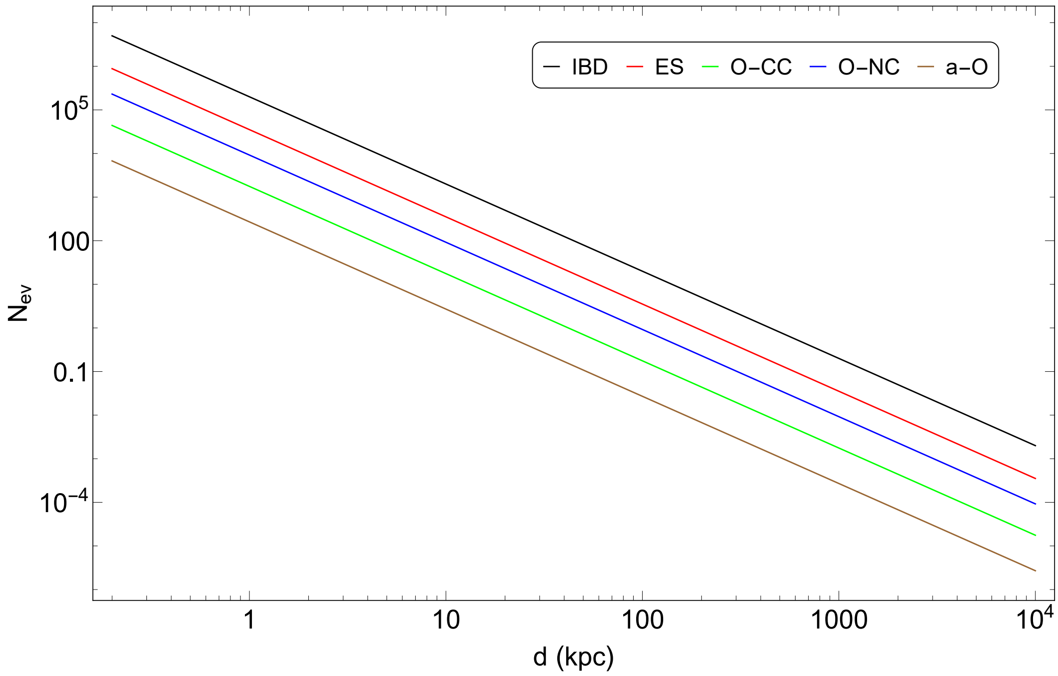

Figure 4.5: Neutrino and axion events for the all detection channels as function of the SN distance in the range $[5; 10]$ MeV for a detector of mass $M = 374$ kton.

This possibility will be soon realized in Super-Kamiokande doping the detector with Gd to improve the neutron capture cross section for better tagging of $\bar{\nu}_e$ [Bea03]. This upgrade has been proposed to strongly enhance the detectability of the feeble signal associated with diffuse SN neutrino background (DSNB) coming from all the past core-collapse SNe in the Universe [Lah13]. The tagging efficiency for electrons via neutron capture on free protons is about 18%. A Gd tagging efficiency of at least 67% has been demonstrated [Wat08], but it can likely be improved beyond that. In this sense we will assume 90% tagging efficiency as quoted in [Lah13]. Then, the remaing 10% of the IBD signal can be statistically subtracted. In conclusion, the IBD is the most important contribution to the background, but it can be reduced up to 90% in Gd-doped detectors as shown in Tab. (4.4).

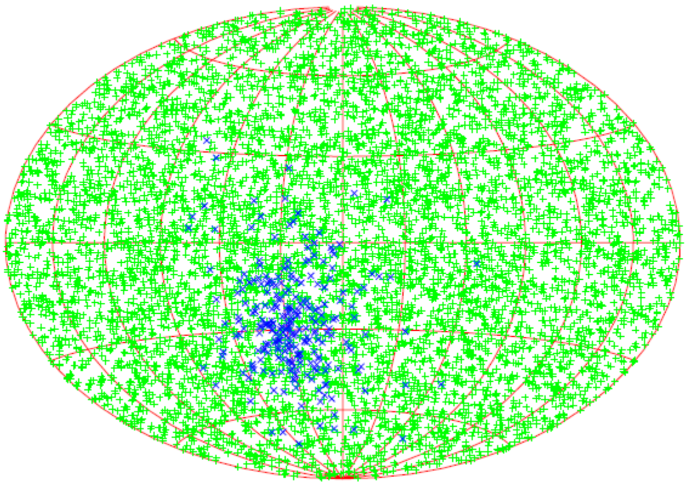

Figure 4.6: Angular distribution of IBD events (green) and ES (blue) from a simulated SN. (Figure taken from [Tom03]).

Elastic scattering

The ES involves the all flavors and produce an unbound electron, and then Cherenkov radiation. The scattered electron preserves the incident neutrino direction and indeed can be used to point the SN as shown in Fig. (4.6) [Raf96]. Then the majority of ES events (about 95%) is contained in a 40° cone, making possible a reduction of this background by means of a directional cut. This directional cut eliminates also the 12% of the events in the other channels [Lah13, Tom03].

NC and CC nuclear interactions

Concering neutrino O-NC and O-CC interactions, we assume that can be statistically subtracted, measuring the input neutrino fluxes in combination with other experiments (e.g. DUNE and JUNO).

The resultant events are shown in Tab. (4.4).

After all the background reduction, one realizes the axion signal would appear at less than 2σ for a nearby SN at $d = 1\,\mathrm{kpc}$.

Table 4.4: Total number of events with and without neutrino background reduction in the range [5; 10] MeV for a SN at $d = 1\,\mathrm{kpc}$ and detector mass $M = 374\,\mathrm{kton}$. We assume neutrino normal mass hierarchy.

Background reduction $g_{ap} = 9 \times 10^{-10}, g_{an} = 0$			
Interaction	Events	Gd doping	Directional cut
a-O	270	270	238
IBD	1.99×10^5	1.99×10^4	1.75×10^4
ES	3.53×10^4	3.53×10^4	1.77×10^3
O-CC	1.76×10^3	1.76×10^3	1.55×10^3
O-NC	9.21×10^3	9.21×10^3	8.10×10^3

4.4.3 New calculation of axion emissivity

Taking into account the corrections in Appendix A.4, that extends the nucleon axion-bremsstrahlung beyond the OPE approximation, the new axion flux F' would be roughly reduced by a factor ~ 20 with respect to the one we have used until now (F):

$$F' \sim \frac{F}{20} \,. \tag{4.17}$$

Since the flux in the free-streaming regime is proportional to [Eq. (2.15)] $F \sim g_{ap}^2$, to obtain the same luminosity of F, the new coupling constant g_p' should obey to

$$F'(g_{ap}') = F(g_{ap}) \;\rightarrow\; \frac{F(g_{ap}')}{20} = F(g_{ap}) \;\rightarrow\; {g_{ap}'}^2 = 20 g_{ap}^2 \,. \tag{4.18}$$

Therefore in this case, with the same flux, the cross section is enhanced by a factor 20 ($g_{ap}' = 4 \times 10^{-9}$) [Eq. (3.33)]. Then the detected axion events would be 20 times larger than the ones calculated until now. These rough estimates are summarized in Tab. (4.5). With this enhanced coupling, the free-streaming axions are clearly observable for a SN at $d = 1\,\mathrm{kpc}$, at $\sim 28\sigma$, and they have a significance of $\sim 3\sigma$ for a SN at $d = 10\,\mathrm{kpc}$. Therefore, this estimate would really open the possibility to detect free-streaming axions and it deserves a dedicated investigation to confirm it, with new simulations of axion emissivity.

Table 4.5: Total number of events, with background reduction ($g_{ap} = 4 \times 10^{-9}$ and $g_{an} = 0$) in the range $[5; 10]$ MeV for a SN at $d = 1$ kpc and a detector mass $M = 374$ kton. We assume neutrino normal mass hierarchy.

$g_{ap} = 4 \times 10^{-9}, g_{an} = 0$	
Interaction	Events
a-O	4.76×10^3
IBD	1.75×10^4
ES	1.77×10^3
O-CC	1.55×10^3
O-NC	8.10×10^3

4.5 Axion event rate in the trapping regime

In the trapping regime ($g_{ap} = g_{an} = 10^{-6}$) the neutrino fluxes are unperturbed as explainded in Chap. 2. The neutrino and axion number of events are shown in Tab. (4.6). The axion signal is very clear also from a SN at 10 kpc without any background reduction.

Table 4.6: Number of events in the range [5; 10] MeV for a SN at $d = 10$ kpc and a detector mass $M = 374$ kton. We assume neutrino normal mass hierarchy in the first column and inverted mass hierarchy in the second.

$g_{ap} = g_{an} = 10^{-6}$		
Interaction	Events NH	Events IH
a-O	2.73×10^5	2.73×10^5
IBD	2.85×10^3	3.31×10^3
ES ν_e	27	27
ES $\overline{\nu}_e$	55	55
ES $4\nu_x$	440	440
O-CC ν_e	19	19
O-CC $\overline{\nu}_e$	5	6
O-NC ν_e	2	2
O-NC $\overline{\nu}_e$	20	20
O-NC ν_x	43	43
O-NC $\overline{\nu}_x$	51	51

Chapter 5

Conclusions

In this Thesis we revised and updated the mechanism of axion emission from core-collapse SNe and characterized the perspectives for their detection in a large Mton-class water Cherenkov detector. At first, using the state-of-the-art SN simulations, we characterized the expected axion spectrum in both free-streaming and trapping regime. Then, our main goal was to investigate if this axion flux, that can be comparable or larger than the neutrino one, has chances of being detected in the case of a Galactic SN explosion. In this regard, as realized in a seminal paper by Engel *et al.* [Eng90], the main detection channel for axions in a water Cherenkov detector would be the axion absorption on oxygen nuclei, whose de-excitation would lead to a photon signal. In order to have a reliable characterization of this signal we performed an updated calculation of the axion-oxygen cross section, based on avanced techniques used in nuclear physics (Random Phase Approximation). With this result, the next step has been to calculate the branching ratio for oxygen de-excitation in photons. For this purpose, we used a code (SMARAGD Hauser-Feshbach reaction code) that computed the decay branching ratio in the all possible channels for oxygen excited by axion absorption. With a complete characterization of the cross section, we finally computed the gamma-ray signal associated with the axion-oxygen process in a Mton-scale water Cherenkov detector, such as Hyper-Kamiokande. We realized that in the trapping regime the axion signal would be clearly detectable, but in the free-streaming case it would be submerged by a huge neutrino background. However, if the Hyper-Kamiokande detector would be doped with Gd, this would allow one to reduce the huge background from inverse beta decay. Then, in principle the axion signal seems to be detectable expecially if one includes the recently-discussed modifications [Cha18] in the calculation of axion emissivity from a SN. Our work motivates further studies to improve the characterization of the axion emission process and of the signal detectability. In this context, our main result, i.e. the accurate characterization of the axion detection cross section, would remain extremely useful to perform further and more accurate estimates. In conclusion, the next Galactic SN explosion together with the unprecedent sensitivity of next-generation neutrino detectors would be a lifetime opportunity for axions.

Appendix A

Axion processes in a nuclear medium

A.1 The energy-loss rate

Axions are produced in a SN enviroment mostly by nucleon bremsstrahlung.

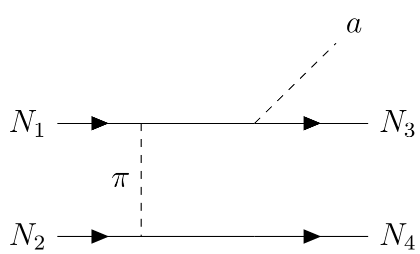

The matrix element of this process, for a single species of nucleons, is [Raf96]

$$\sum_{\text{spin}} |\mathcal{M}|^2 = \frac{16(4\pi)^3\alpha_\pi^2\alpha_a}{3m_N^2}\left[\left(\frac{\mathbf{k}^2}{\mathbf{k}^2+m_\pi^2}\right)^2 + \left(\frac{\mathbf{l}^2}{\mathbf{l}^2+m_\pi^2}\right)^2 + \right. \\ \left. + \frac{\mathbf{k}^2\mathbf{l}^2 - 3(\mathbf{k}\cdot\mathbf{l})^2}{(\mathbf{k}^2+m_\pi^2)(\mathbf{l}^2+m_\pi^2)}\right] ; \tag{A.1}$$

where $\alpha_a = (C_N m_N/f_a)^2 1/4\pi$, $\mathbf{k} = \mathbf{p}_2 - \mathbf{p}_4$ and $\mathbf{l} = \mathbf{p}_2 - \mathbf{p}_3$. The first term is the result from direct diagrams, the second from the exchange diagrams and the third term results from the interference. From the equipartition principle $\mathbf{k}^2 \approx 3m_N T$ and then $\mathbf{k}^2 \gg m_\pi^2$ for a typical SN temperature. Therefore Eq. (A.1) becomes

$$\sum_{\text{spin}} |\mathcal{M}|^2 = \frac{16(4\pi)^3\alpha_\pi^2\alpha_a}{m_N^2}\left[1 - (\hat{\mathbf{k}}\cdot\hat{\mathbf{l}})^2\right] \; ; \tag{A.2}$$

and the term $(\hat{\mathbf{k}}\cdot\hat{\mathbf{l}})^2$ could be important in a non-degenerate enviroment. However, in a first approximation the matrix element can be written as [Raf96]

$$\sum_{\text{spin}} |\mathcal{M}|^2 = \frac{16(4\pi)^3\alpha_\pi^2\alpha_a}{m_N^2} \; . \tag{A.3}$$

The energy-loss rate is defined as [Raf96]

$$\begin{aligned} Q_a = \int \frac{d^3\mathbf{k}_a}{2\omega_a(2\pi)^3}\omega_a \int \prod_{i=1}^{4} \frac{d^3\mathbf{p}_i}{2E_i(2\pi)^3} f_1 f_2 (1-f_3)(1-f_4)\times \\ (2\pi)^4\delta^4(P_1+P_2-P_3-P_4-K_a)\frac{1}{4}\sum_{\text{spins}}|\mathcal{M}|^2 \; ; \end{aligned} \tag{A.4}$$

where the factor 4 eliminates the double counting of identical fermions. In a non-degenerate enviroment we consider (in the non-relativistic approximation) Maxwell-Boltzmann energy distributions, neglecting the Pauli blocking factors $1 - f_{3,4}$

$$\begin{aligned} f_{\mathbf{p}} &= \frac{n_B}{2}\left(\frac{2\pi}{m_N T}\right)^{3/2} e^{-\mathbf{p}^2/2m_N T} \; ; \\ 2\int \frac{d^3\mathbf{p}}{(2\pi)^3} f_{\mathbf{p}} &= n_B \; . \end{aligned} \tag{A.5}$$

In the bremsstrahlung process the typical axion energy will be $\omega_a = \mathbf{p}^2/2m_N \ll |\mathbf{p}|$, then the Dirac delta can be approximated as

$$\delta^4(P_1+P_2-P_3-P_4-K_a) \approx \delta(E_1+E_2-E_3-E_4-\omega_a)\delta^3(\mathbf{p}_1+\mathbf{p}_2-\mathbf{p}_3-\mathbf{p}_4) \; . \tag{A.6}$$

With these approximations Eq. (A.4) becomes

$$\begin{aligned} Q_a = \int \frac{d\omega_a}{(2\pi)^2}\omega_a^2 \int \prod_{i=1}^{4} \frac{d^3\mathbf{p}_i}{2m_N(2\pi)^3} f_1 f_2 (2\pi)^4 \delta(E_1+E_2-E_3-E_4-\omega_a)\times \\ \delta^3(\mathbf{p}_1+\mathbf{p}_2-\mathbf{p}_3-\mathbf{p}_4)\frac{1}{4}\sum_{\text{spins}}|\mathcal{M}|^2 \; . \end{aligned} \tag{A.7}$$

Integrating over one of the $\mathbf{p}_i$ we can remove the delta over the momenta

$$\begin{aligned} Q_a =& \frac{1}{16 m_N^4 (2\pi)^{10}} \int d\omega_a \omega_a^2 \int \prod_{i=1}^{3} d^3\mathbf{p}_i \left(\frac{n_B}{2} \left(\frac{2\pi}{m_N T} \right)^{3/2} \right)^2 \times \\ & e^{-\mathbf{p}_1^2/2m_N T} e^{-\mathbf{p}_2^2/2m_N T} \delta(E_1 + E_2 - E_3 - E_4 - \omega_a) \sum_{\text{spins}} |\mathcal{M}|^2 \; . \end{aligned} \tag{A.8}$$

In the center of mass reference frame we can write

$$\mathbf{p}_{1/2} = \mathbf{p}_0 \pm \mathbf{p} \qquad \mathbf{p}_{3/4} = \mathbf{p}_0 \pm \mathbf{q} \tag{A.9}$$

and then

$$\begin{aligned} Q_a =& \frac{1}{8 m_N^4 (2\pi)^{10}} \int d\omega_a \omega_a^2 \int d^3\mathbf{p}_0 d^3\mathbf{p} d^3\mathbf{q} \left(\frac{n_B}{2} \left(\frac{2\pi}{m_N T} \right)^{3/2} \right)^2 \times \\ & e^{-\mathbf{p}_0^2/m_N T} e^{-\mathbf{p}^2/m_N T} \delta \left(\frac{\mathbf{p}^2}{m_N} - \frac{\mathbf{q}^2}{m_N} - \omega_a \right) \sum_{\text{spins}} |\mathcal{M}|^2 \; ; \end{aligned} \tag{A.10}$$

where we inserted a factor 2 from the Jacobian. Integrating over $\mathbf{p}_0$ using Eq. (A.5) we obtain

$$\begin{aligned} & \int d^3\mathbf{p}_0 \, e^{-\mathbf{p}_0^2/m_N T} = (2\pi)^3 \left(\frac{m_N T}{4\pi} \right)^{3/2} \; ; \\ Q_a =& \frac{n_B^2}{32 m_N^4 (2\pi)^4} \int d\omega_a \omega_a^2 \int d^3\mathbf{p} d^3\mathbf{q} \left(\frac{1}{4\pi m_N T} \right)^{3/2} \\ & e^{-\mathbf{p}^2/m_N T} \delta \left(\frac{\mathbf{p}^2}{m_N} - \frac{\mathbf{q}^2}{m_N} - \omega_a \right) \sum_{\text{spins}} |\mathcal{M}|^2 \; . \end{aligned} \tag{A.11}$$

Introducing the new variables

$$\begin{aligned} u^2 &= \frac{\mathbf{p}^2}{m_N T} \qquad & d|\mathbf{p}| &= \sqrt{m_N T} du \; ; \\ v^2 &= \frac{\mathbf{q}^2}{m_N T} \qquad & d|\mathbf{q}| &= \sqrt{m_N T} dv \; ; \\ x &= \frac{\omega_a}{T} \qquad & d\omega_a &= T \, dx \; . \end{aligned} \tag{A.12}$$

The delta becomes

$$\delta \left(\frac{\mathbf{p}^2}{m_N} - \frac{\mathbf{q}^2}{m_N} - \omega_a \right) = \delta(u^2 - v^2 - |x|) \frac{1}{T} \; ; \tag{A.13}$$

and the energy-loss rate

$$Q_a = \frac{n_B^2 T^3 \sqrt{T}\sqrt{\pi}}{32 \times 8 m_N^{5/2} \pi^4} \int_0^{+\infty} dx\, x^2 \int du\, dv\, u^2 v^2 e^{-u^2} \delta(u^2 - v^2 - |x|) \sum_{\text{spins}} |\mathcal{M}|^2 \,. \tag{A.14}$$

Introducing the functions

$$\begin{aligned}
\Gamma_\sigma &= 4\sqrt{\pi}\alpha_\pi^2 n_B \sqrt{T} m_N^{-5/2} \,; \\
s(x) &= 4 \int du\, dv\, u^2 v^2 e^{|x| - u^2} \delta(u^2 - v^2 - |x|) = \\
&= 2 \int du\, dv\, u v^2 e^{|x| - u^2} \delta(u - \sqrt{v^2 + |x|}) = \\
&= 2 \int dv\, \sqrt{v^2 + |x|} v^2 e^{-v^2} = \int dy \sqrt{y^2 + y|x|} e^{-y} \approx \sqrt{1 + \frac{|x|\pi}{4}} \,;
\end{aligned} \tag{A.15}$$

where $y = v^2$, we obtain

$$Q_a = \frac{n_B T^3}{32 \times 8\pi^4} \frac{\Gamma_\sigma}{16\alpha_\pi^2} \int_0^{+\infty} dx\, x^2 s(x) e^{-x} \sum_{\text{spins}} |\mathcal{M}|^2 \,. \tag{A.16}$$

In the case of axion bremsstrahlung this equation becomes

$$Q_a = \frac{\alpha_a n_B \Gamma_\sigma T^3}{4\pi m_N^2} \int_0^{+\infty} dx\, x^2 s(x) e^{-x} \,. \tag{A.17}$$

A.2 Mixture of protons and neutrons

Eq. (A.1) can be generalized to axions that couple to both protons and neutrons as follows [Raf95]. The direct terms are

$$\begin{aligned}
\sum_{\text{spin}} |\mathcal{M}|^2 =& \frac{16(4\pi)^3 \alpha_\pi^2 \alpha_a}{3 m_N^2} C_{p,n}^2 \\
& \left[\left(\frac{\mathbf{k}^2}{\mathbf{k}^2 + m_\pi^2} \right)^2 + \left(\frac{\mathbf{l}^2}{\mathbf{l}^2 + m_\pi^2} \right)^2 + \frac{\mathbf{k}^2 \mathbf{l}^2 - 3(\mathbf{k} \cdot \mathbf{l})^2}{(\mathbf{k}^2 + m_\pi^2)(\mathbf{l}^2 + m_\pi^2)} \right] \,;
\end{aligned} \tag{A.18}$$

and the exchange term is

$$\sum_{\text{spin}} |\mathcal{M}|^2 = \frac{16(4\pi)^3\alpha_\pi^2\alpha_a}{3m_N^2}\left[(C_0^2+C_1^2)\left(\frac{\mathbf{k}^2}{\mathbf{k}^2+m_\pi^2}\right)^2 + \right.$$
$$\left. + (4C_0^2+2C_1^2)\left(\frac{\mathbf{l}^2}{\mathbf{l}^2+m_\pi^2}\right)^2 + 2\,\frac{(C_0^2+C_1^2)\mathbf{k}^2\mathbf{l}^2-(3C_0^2+C_1^2)(\mathbf{k}\cdot\mathbf{l})^2}{(\mathbf{k}^2+m_\pi^2)(\mathbf{l}^2+m_\pi^2)}\right] \; ; \tag{A.19}$$

where $C_0 = (C_p + C_n)/2$ and $C_1 = (C_p - C_n)/2$. Now we will discuss only the exchange term. Introducing the new variables

$$\begin{aligned} u &= \frac{\mathbf{p}^2}{m_N T} & d|\mathbf{p}| &= \sqrt{\frac{m_N T}{u}}\frac{du}{2} \; ; \\ v &= \frac{\mathbf{q}^2}{m_N T} & d|\mathbf{q}| &= \sqrt{\frac{m_N T}{v}}\frac{dv}{2} \; ; \\ x &= \frac{\omega_a}{T} & d\omega_a &= T\,dx \; ; \\ y &= \frac{m_\pi^2}{m_N T} & z &= \frac{\mathbf{p}\cdot\mathbf{q}}{|\mathbf{p}||\mathbf{q}|} \; ; \end{aligned} \tag{A.20}$$

and

$$\begin{aligned} \frac{\mathbf{k}^2}{m_N T} &= u + v - 2z\sqrt{uv} \; ; \\ \frac{\mathbf{l}^2}{m_N T} &= u + v + 2z\sqrt{uv} \; ; \\ \frac{\mathbf{k}\cdot\mathbf{l}}{m_N T} &= u - v \; . \end{aligned} \tag{A.21}$$

The matrix element in Eq. (A.19) can be written as

$$\sum_{\text{spin}} |\mathcal{M}|^2 = \frac{16(4\pi)^3\alpha_\pi^2\alpha_a}{3m_N^2}\left[(C_0^2+C_1^2)\left(\frac{u+v-2z\sqrt{uv}}{u+v-2z\sqrt{uv}+y}\right)^2 + \right.$$
$$+ (4C_0^2+2C_1^2)\left(\frac{u+v+2z\sqrt{uv}}{u+v+2z\sqrt{uv}+y}\right)^2 +$$
$$\left. + 2\,\frac{(C_0^2+C_1^2)[(u+v)^2-4z^2uv]-(3C_0^2+C_1^2)(u-v)^2}{[(u+v+y)^2-4z^2uv]}\right] . \tag{A.22}$$

From Eq. (A.11)

$$\begin{aligned} Q_a =& \frac{n_B^2 T^5}{64 m_N (2\pi)^2} \int dx\, x^2 \int du\, dv\, dz\, \sqrt{uv} \left(\frac{1}{4\pi m_N T}\right)^{3/2} \\ & e^{-u} \delta\left(u - v - |x|\right) \sum_{\text{spins}} |\mathcal{M}|^2 = \\ =& \frac{n_B^2 T^{7/2}}{64 \times 32 m_N^{5/2} \pi^3 \sqrt{\pi}} \int dx\, x^2 \int du\, dv\, dz\, \sqrt{uv} e^{-u} \\ & \delta\left(u - v - |x|\right) \sum_{\text{spins}} |\mathcal{M}|^2 \, . \end{aligned} \tag{A.23}$$

Inserting Eq. (A.22) in Eq. (A.23) we obtain

$$Q_a = \frac{\alpha_\pi^2 \alpha_a n_B^2 T^{7/2}}{6 m_N^{9/2} \sqrt{\pi}} \int dx\, x^2 \int du\, dv\, dz\, \sqrt{uv} e^{-u} \delta\left(u - v - |x|\right) f(u,v,z) \, . \tag{A.24}$$

where $f(u,v,z)$ is the momentum dependent part in Eq. (A.22). Neglecting the pion mass, $y = 0$, Eq. (A.24) can be written as

$$Q_a = \frac{\alpha_a \alpha_\pi^2}{\sqrt{\pi}} \frac{n_B^2 T^{7/2}}{m_N^{9/2}} \frac{128}{105} [3(C_0^2 + C_1^2) I_0 + (4C_0^2 + 2C_1^2) I_0 - (6C_0^2 + 2C_1^2) I_{\mathbf{k}\cdot\mathbf{l}}] \, ; \tag{A.25}$$

where

$$\begin{aligned} I_0 =& \frac{35}{128} \int du\, dv\, dx\, x^2 \sqrt{uv} e^{-u} \delta(u - v - x) = \frac{35}{128} \int dx\, x^2 e^{-x} s_0(x) \, ; \\ I_{\mathbf{k}\cdot\mathbf{l}} =& \frac{35}{128} \int du\, dv\, dx\, x^2 \sqrt{uv} e^{-u} \delta(u - v - x) \frac{1}{2} \int_{-1}^{1} dz\, \frac{(u-v)^2}{(u+v)^2 - 4z^2 uv} = \\ =& \frac{35}{128} \int dv\, dx\, x^4 \sqrt{(v+x)v} e^{-x} e^{-v} \frac{1}{2} \int_{-1}^{1} dz\, \frac{1}{(2v+x)^2 - 4z^2 (v+x) v} = \\ =& \frac{35}{128} \int dv\, dx\, x^4 \frac{\sqrt{(v+x)v}}{2v+x} e^{-x} e^{-v} \\ & \int_{-1}^{1} dz \left(\frac{1}{(2v+x) - 2z\sqrt{v(v+x)}} + \frac{1}{(2v+x) + 2z\sqrt{v(v+x)}} \right) = \\ =& \frac{35}{128} \int dv\, dx\, \frac{x^4}{4(2v+x)} e^{-x} e^{-v} \log\left(\frac{2v + x + 2\sqrt{v(v+x)}}{2v + x - 2\sqrt{v(v+x)}} \right) = \\ =& \frac{35}{128} \int dx\, x^2 e^{-x} s_{\mathbf{k}\cdot\mathbf{l}}(x) \, ; \end{aligned} \tag{A.26}$$

and

$$
\begin{aligned}
s_0(x) &= \int dv\, \sqrt{(v+x)v}e^{-v} \; ; \\
s_{\mathbf{k}\cdot\mathbf{l}}(x) &= \int dv\, \frac{x^2}{4(2v+x)} e^{-v} \log\left(\frac{2v+x+2\sqrt{v(v+x)}}{2v+x-2\sqrt{v(v+x)}}\right) \; .
\end{aligned}
\tag{A.27}
$$

The energy-loss with direct and exchange terms can be written as

$$
Q_a = \frac{\alpha_a \alpha_\pi^2}{\sqrt{\pi}} \frac{n_B^2 T^{7/2}}{m_N^{9/2}} \int dx\, x^2 e^{-x} s(x) \; ; \tag{A.28}
$$

where

$$
\begin{aligned}
s(x) =& \frac{4}{3} Y_p Y_n \left[(7C_0^2 + 5C_1^2) s_0(x) - (6C_0^2 + 2C_1^2) s_{\mathbf{k}\cdot\mathbf{l}}(x)\right] + \\
&+ (Y_p^2 C_p^2 + Y_n^2 C_n^2)(s_0(x) - s_{\mathbf{k}\cdot\mathbf{l}}(x)) \; .
\end{aligned}
\tag{A.29}
$$

A.3 Axion opacity

The axion velocity is [Raf96]

$$
\beta_\omega = v = \frac{p}{\omega} = \frac{\sqrt{\omega^2 - m^2}}{\omega} = \sqrt{1 - \frac{m^2}{\omega^2}} \; . \tag{A.30}
$$

The mean free path for a given energy ω is l_ω and the energy distribution is

$$
B_\omega(T)\, d\omega = \frac{\omega}{e^{\omega/T} - 1} \frac{d^3\mathbf{k}}{(2\pi)^3} = \frac{1}{2\pi^2} \frac{\omega^3}{e^{\omega/T} - 1} d\omega \; . \tag{A.31}
$$

The energy flux is related to the energy gradient [Raf96]:

$$
F_\omega = -\frac{1}{3} \beta_\omega l_\omega \nabla B_\omega \; . \tag{A.32}
$$

The integrated flux is

$$
F = -\frac{1}{3} \int_0^\infty d\omega\, \beta_\omega l_\omega \partial_T B_\omega \nabla T \; ; \tag{A.33}
$$

where $\partial_T = \partial / \partial T$. For photons one defines the Rosseland mean opacity as [Raf96]

$$
\frac{1}{k_\gamma \rho} = -\frac{3F}{\nabla(aT^4)} \; ; \tag{A.34}
$$

where the photon energy density is aT^4 and $a = \pi^2/15$. Similarly we define the axion mean opacity

$$\frac{1}{k_x\rho} = \frac{15}{4\pi^2 T^3}\int_0^\infty d\omega\, l_\omega (1-e^{-\omega/T})^{-1}\partial_T B_\omega \;; \tag{A.35}$$

and the enhancement factor stimulates the production of low-energy bosons. Introducing the variable $x = \omega/T$ and neglecting the term of lower order than x^4e^{2x}, Eq. (A.35) becomes [Raf96]

$$\begin{aligned} \frac{1}{k_x\rho} &= -\frac{15}{8\pi^4}\int_0^\infty dx\, l_x \frac{xe^x}{(e^x-1)}\partial_x \frac{x^3}{e^x-1} = \\ &= -\frac{15}{8\pi^4}\int_0^\infty dx\, l_x \frac{xe^x}{(e^x-1)}\frac{3x^2(e^x-1)-x^3e^x}{(e^x-1)^2} \approx \\ &\approx \frac{15}{8\pi^4}\int_0^\infty dx\, l_x \frac{x^4e^{2x}}{(e^x-1)^3}\;. \end{aligned} \tag{A.36}$$

The energy-loss rate is obtained mediating the term $\omega/\Delta t$ where Δt is a typical axion emission time. Axions escape in a characteristic time $\Delta t \sim l_\omega/\beta_\omega$ and then

$$Q_a \sim \int d\omega\, \omega^2 e^{-\omega/T}\frac{\omega}{l_\omega/\beta_\omega}\;; \tag{A.37}$$

where $\beta_\omega = 1$ for axions. From Eq. (A.35), since $\alpha_a = (C_N m_N/f_a)^2/4\pi$

$$\begin{aligned} Q_a &= \left(\frac{C_N m_N}{f_a}\right)^2 \frac{n_B\Gamma_\sigma T^3}{8\pi^2 m_N^2}\int_0^{+\infty} dx\, x^2 s(x) e^{-x} = \\ &= \frac{T^4}{\pi^2}\int_0^{+\infty} dx\, x^2 e^{-x} x l_x^{-1}\;; \end{aligned} \tag{A.38}$$

we identify the mean free path as

$$l_x^{-1} = \left(\frac{C_N}{2f_a}\right)^2 \frac{n_B\Gamma_\sigma}{T}\frac{s(x)}{2x}\;. \tag{A.39}$$

The Rosseland mean opacity is [Raf96]

$$\begin{aligned} k_a &= \left(\frac{C_N}{2f_a}\right)^2 \frac{\Gamma_\sigma}{Tm_N}\hat{k}\;; \\ \hat{k}^{-1} &= \frac{15}{8\pi^4}\int_0^\infty dx\, \frac{x^4e^{2x}}{(e^x-1)^3}\frac{2x}{s(x)}\;. \end{aligned} \tag{A.40}$$

A.4 Corrections to the axion energy-loss rate

In a recent paper [Cha18] the axion absorption rate is calculated taking into account various corrections. The axion absorption rate would be

$$\Gamma_a = \Gamma_a^{nn} + \Gamma_a^{pn} + \Gamma_a^{np} + \Gamma_a^{pp} \; ; \quad \Gamma_a^{ij} = \frac{C_i^2 Y_i Y_j}{4 f_a^2} \frac{\omega}{2} \frac{n_B^2 \sigma_{np\pi}}{\omega^2} \gamma_f \gamma_p \gamma_h \; ; \tag{A.41}$$

where C_i for $i = n, p$ are the axion-nucleon coupling constants; Y_i for $i = n, p$ are the nucleon number per baryon; $\sigma_{np\pi}$ is the nucleon-nucleon cross section in the OPE approximation with vanishing pion mass, defined as

$$\sigma_{np\pi} = 4\alpha_\pi^2 \sqrt{\frac{\pi T}{m_N^5}} \; . \tag{A.42}$$

The three corrections are:

$$\gamma_f = \frac{1}{1 + (n_B \sigma_{np\pi}/2\omega)^2} \; ; \tag{A.43}$$

to cut-off the infrared divergence in Eq. (A.41); γ_p to account for the pion finite mass and γ_h is the ratio between the structure function in the chiral perturbation theory and the one calculated in the OPE. These factors suppress the emission rate by a factor between 5 and 100 as shown in Fig. (A.1).

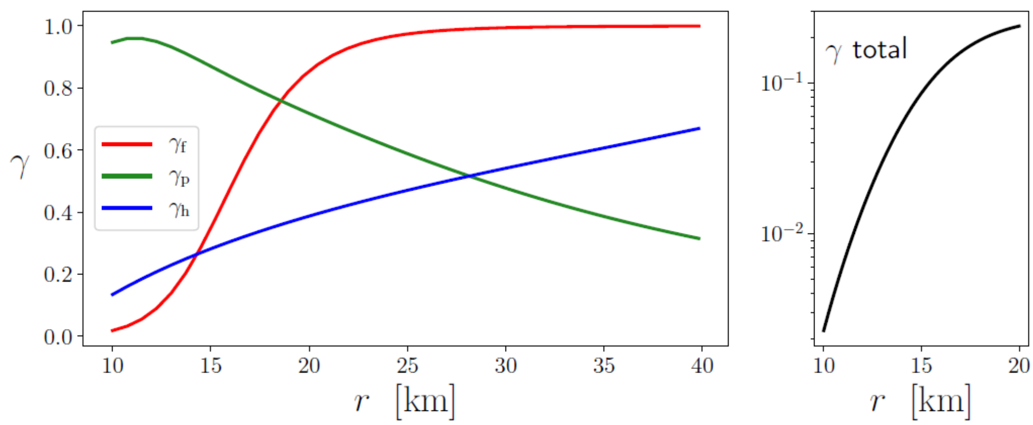

Figure A.1: (Left panel) The correction factors discussed in the text. Near the core the suppression is about two orders of magnitude. (Right panel) Product of the corrections near the core. (Figure taken from [Cha18]).

Appendix B

More on RPA

B.1 RPA equations in angular momentum coupling

We consider two reference systems rotated by the Euler angles α, β, γ. The rotation matrix $D(\alpha, \beta, \gamma)$ is an operator defined by the operation

$$\mathbf{r}' = D(\alpha, \beta, \gamma)\mathbf{r} = e^{i\gamma J_z} e^{i\beta J_y} e^{i\alpha J_x} \mathbf{r} \ . \tag{B.1}$$

Two rotated eigenstates of $\mathbf{J}^2$ and J_z are $|jm\rangle$ and $|jm'\rangle$, which differ only for the J_z eigenvalues. The matrix element of the rotation matrix between these states is

$$\langle jm'|D(\alpha, \beta, \gamma)|jm\rangle = D^j_{m'm}(\alpha, \beta, \gamma) \ . \tag{B.2}$$

An irreducible spherical operator of rank k is a set of $2k+1$ operators transforming under a rotation as [Sch80]

$$D(\alpha, \beta, \gamma) T^k_q D^\dagger(\alpha, \beta, \gamma) = \sum_{q'=-k}^{k} T^k_{q'} D^k_{q'q}(\alpha, \beta, \gamma) \ . \tag{B.3}$$

Eq. (3.60) can be explicitly written in the angular momentum basis because the nuclear states are eigenstates of $\mathbf{J}^2$ and J_z operators. In this basis, Eq. (3.56) becomes [Sch80]

$$
\begin{aligned}
Q^{\dagger}_{J,M}(j_p, j_h) &= \sum_{ph} \left[X^{J,M}_{ph} a^{\dagger}_{j_p m_p} (-1)^{j_h+m_h} a_{j_h -m_h} - Y^{J,M}_{ph} a^{\dagger}_{j_h m_h} (-1)^{j_p+m_p} a_{j_p -m_p} \right] \; ; \\
X^{J,M}_{ph} &= \sum_{m_p m_h} \langle j_p m_p j_h m_h | JM \rangle X_{ph} \; ; \\
Y^{J,M}_{ph} &= \sum_{m_p m_h} \langle j_p m_p j_h m_h | J-M \rangle (-1)^{J-M} Y_{ph} \; .
\end{aligned}
\tag{B.4}
$$

This operator is a spherical tensor of rank J and $2J+1$ components indicated by M. Eq. (3.60) becomes [Sch80]

$$
\begin{aligned}
&(\epsilon_p - \epsilon_h - \omega) X^{J,M}_{ph} + \sum_{p'h'} (v^{J}_{ph,p'h'} X^{J,M}_{p'h'} + u^{J}_{ph,p'h'} Y^{J,M}_{p'h'}) = 0 \; ; \\
&(\epsilon_p - \epsilon_h + \omega) Y^{J,M}_{ph} + \sum_{p'h'} ({v^{*}}^{J}_{ph,p'h'} Y^{J,M}_{p'h'} + {u^{*}}^{J}_{ph,p'h'} X^{J,M}_{p'h'}) = 0 \; ;
\end{aligned}
\tag{B.5}
$$

where

$$
\begin{aligned}
&v^{J}_{ph,p'h'} = \sum_{K} (-1)^{j_h + j_{p'} + K} \sqrt{2K+1} \left\{ \begin{array}{ccc} j_p & j_h & J \\ j_{p'} & j_{h'} & K \end{array} \right\} \\
&\left[\langle j_p j_{h'} K || V || j_h j_{p'} K \rangle - (-1)^{j_h + j_{p'} - K} \langle j_p j_{h'} K || V || j_{p'} j_h K \rangle \right] \; ; \\
&u^{J}_{ph,p'h'} = (-1)^{j_{h'} - j_{p'} - J} v^{J}_{ph,h'p'} \; ;
\end{aligned}
\tag{B.6}
$$

introducing the 6-j Wigner symbol.

B.2 Continuum RPA

The RPA can be further extended including excitations to the continuum. We call Continuum RPA (CRPA) this formulation of the RPA. The creation operator in Eq. (3.56) can be generalized as

$$
\begin{aligned}
Q^{\dagger}_{\nu} = \sum_{ph} \Bigg[& \sum_{\epsilon_p > \epsilon_F}^{0} \left(X^{\nu}_{ph}(\epsilon_p) a^{\dagger}_p a_h - Y^{\nu}_{ph}(\epsilon_p) a^{\dagger}_h a_p \right) + \\
& + \int_0^{\infty} d\epsilon_p \left(X^{\nu}_{ph}(\epsilon_p) a^{\dagger}_p a_h - Y^{\nu}_{ph}(\epsilon_p) a^{\dagger}_h a_p \right) \Bigg] \; ;
\end{aligned}
\tag{B.7}
$$

where the energy ϵ_p is a continuous variable. In this case we rewrite Eq. (3.60) considering also continuum transitions. Eq. (3.60) is replaced by an integral system of equations [Sch80]:

$$
\begin{aligned}
&(\epsilon_p - \epsilon_h - \omega) X^{\nu}_{ph}(\epsilon_p) + \sum_{p'h'} (v_{ph,p'h'} X^{\nu}_{p'h'} + u_{ph,p'h'} Y^{\nu}_{p'h'}) + \\
&+ \sum_{p'h'} \int d\epsilon_{p'} \left(v_{ph,p'h'} X^{\nu}_{p'h'}(\epsilon_{p'}) + u_{ph,p'h'} Y^{\nu}_{p'h'}(\epsilon_{p'}) \right) = 0 \; ; \\
&(\epsilon_p - \epsilon_h + \omega) Y^{\nu}_{ph}(\epsilon_p) + \sum_{p'h'} (v^{*}_{ph,p'h'} Y^{\nu}_{p'h'} + u^{*}_{ph,p'h'} X^{\nu}_{p'h'}) + \\
&+ \sum_{p'h'} \int d\epsilon_{p'} \left(v^{*}_{ph,p'h'} Y^{\nu}_{p'h'}(\epsilon_{p'}) + u^{*}_{ph,p'h'} X^{\nu}_{p'h'}(\epsilon_{p'}) \right) = 0 \; .
\end{aligned}
\tag{B.8}
$$

The integration on $\epsilon_{p'}$ is extended to infinity. We introduce the new variables $f_{[p]h}(r)$ and $g_{[p]h}(r)$, called “channel functions”

$$
\begin{aligned}
f_{[p]h}(r) &= \sum_{\epsilon_p > \epsilon_F}^{0} X_{ph}(\epsilon_p) R_p(r, \epsilon_p) + \int_0^{\infty} d\epsilon_{p'} X_{ph}(\epsilon_{p'}) R_p(r, \epsilon_{p'}) \; ; \\
g_{[p]h}(r) &= \sum_{\epsilon_p > \epsilon_F}^{0} Y_{ph}(\epsilon_p) R_p(r, \epsilon_p) + \int_0^{\infty} d\epsilon_{p'} Y_{ph}(\epsilon_{p'}) R_p(r, \epsilon_{p'}) \; .
\end{aligned}
\tag{B.9}
$$

The radial wavefunctions $R_p(r, \epsilon_p)$ are determined by solving the one-body Schrödinger equation

$$
h_p R_p(r, \epsilon_p) = \epsilon_p R_p(r, \epsilon_p) \; ; \tag{B.10}
$$

and they are normalized as

$$
\sum_{\epsilon_\alpha} R^{*}_{\alpha}(r, \epsilon_\alpha) R_\alpha(r', \epsilon_\alpha) + \int d\epsilon_\alpha R^{*}_{\alpha}(r, \epsilon_\alpha) R_\alpha(r', \epsilon_\alpha) = \delta(r - r') \; . \tag{B.11}
$$

Multiplying Eq. (B.8) by $R_\alpha(r,\epsilon_\alpha)$, integrating, summing and using Eq. (B.11) we obtain

$$
\begin{aligned}
&(h_0-\epsilon_h-\omega)f^{J\omega}_{[p]h}(r) = -\sum_{[p']h'}\int dr' r'^2 \left[R^*_{h'}(r')R_h(r)f^{J\omega}_{[p']h'}(r')\langle ph|V|p'h'\rangle + \right.\\
&-R^*_{h'}(r')R_h(r')f^{J\omega}_{[p']h'}(r)\langle ph|V|h'p'\rangle + R_h(r)R_{h'}(r')g^{*\ J\omega}_{[p']h'}(r')\langle pp'|V|hh'\rangle +\\
&\left.-R_h(r')R_{h'}(r)g^{*\ JE}_{[p']h'}(r')\langle pp'|V|h'h\rangle\right] + BST\ ;
\end{aligned}
$$

$$
\begin{aligned}
&(h_0-\epsilon_h+\omega)g^{J\omega}_{[p]h}(r) = -\sum_{[p']h'}\int dr' r'^2 \left[R^*_{h'}(r')R_h(r)g^{J\omega}_{[p']h'}(r')\langle ph|V|p'h'\rangle + \right.\\
&-R^*_{h'}(r')R_h(r')g^{J\omega}_{[p']h'}(r)\langle ph|V|h'p'\rangle + R_h(r)R_{h'}(r')f^{*\ J\omega}_{[p']h'}(r')\langle pp'|V|hh'\rangle +\\
&\left.-R_h(r')R_{h'}(r)f^{*\ JE}_{[p']h'}(r')\langle pp'|V|h'h\rangle\right] + BST\ ;
\end{aligned}
$$

$$
\begin{aligned}
&BST = \sum_{[p']h'}\sum_{\epsilon_p<\epsilon_F}\int dr_1 r_1^2\int dr_2 r_2^2 R_p(r)R_p(r_1)^*\\
&\left\{R^*_{h'}(r_2)\left[R_h(r_1)f_{[p']h'}(r_2)\langle ph|V|p'h'\rangle + \right.\right.\\
&\left.-R_h(r_2)f_{[p']h'}(r_1)\langle ph|V|h'p'\rangle\right] + g^*_{[p']h'}(r_2)\left[R_h(r_1)R_{h'}(r_2)\langle pp'|V|hh'\rangle + \right.\\
&\left.\left.-R_{h'}(r_1)R_h(r_2)\langle pp'|V|h'h\rangle\right]\right\}\ .
\end{aligned}
\tag{B.12}
$$

We solve Eq. (B.12) each time imposing that a particle is emitted in a channel defined by the quantum numbers p_0, h_0. The asymptotic behaviour of the solutions must be the same of the free scattering. The numerical techniques used to solve these equations are described in detail in [Co11].

B.3 Interaction potential

A very general expression of the interaction potential depends from spin $\boldsymbol{\sigma}$ and isospin $\boldsymbol{\tau}$ operators [Sch80]

$$\begin{aligned} V(r_{12}) &= v_1(r_{12}) + v_2(r_{12})\boldsymbol{\tau}_1 \cdot \boldsymbol{\tau}_2 + v_3(r_{12})\boldsymbol{\sigma}_1 \cdot \boldsymbol{\sigma}_2 + \\ &+ v_4(r_{12})(\boldsymbol{\tau}_1 \cdot \boldsymbol{\tau}_2)(\boldsymbol{\sigma}_1 \cdot \boldsymbol{\sigma}_2) + v_5(r_{12})S_{12}(\hat{r}_{12}) + v_6(r_{12})S_{12}(\hat{r}_{12})\boldsymbol{\tau}_1 \cdot \boldsymbol{\tau}_2 + \\ &+ [v_\rho(r_{12}) + v_{\rho,\tau}(r_{12})(\boldsymbol{\tau}_1 \cdot \boldsymbol{\tau}_2)][\rho(r_1)\rho(r_2)]^{\alpha/2} \ ; \end{aligned} \tag{B.13}$$

where

$$S_{12}(\hat{r}) = 3(\boldsymbol{\sigma}_1 \cdot \hat{r})(\boldsymbol{\sigma}_2 \cdot \hat{r}) - \boldsymbol{\sigma}_1 \cdot \boldsymbol{\sigma}_2 \ . \tag{B.14}$$

Bibliography

[Abe11] K. Abe *et al.*, “Letter of Intent: The Hyper-Kamiokande Experiment — Detector Design and Physics Potential —,” arXiv:1109.3262 [hep-ex].

[Ang12] M. Anguiano, M. Grasso, G. Co’, V. De Donno and A. M. Lallena, “Tensor and tensor-isospin terms in the effective Gogny interaction,” Phys. Rev. C **86** (2012) 054302 [arXiv:1210.5333 [nucl-th]].

[Arc13] M. Archidiacono, S. Hannestad, A. Mirizzi, G. Raffelt and Y. Y. Y. Wong, “Axion hot dark matter bounds after Planck,” JCAP **1310** (2013) 020 [arXiv:1307.0615 [astro-ph.CO]].

[Asz09] S. J. Asztalos *et al.* [ADMX Collaboration], “A SQUID-based microwave cavity search for dark-matter axions,” Phys. Rev. Lett. **104** (2010) 041301 [arXiv:0910.5914 [astro-ph.CO]].

[Aya14] A. Ayala, I. Domínguez, M. Giannotti, A. Mirizzi and O. Straniero, “Revisiting the bound on axion-photon coupling from Globular Clusters,” Phys. Rev. Lett. **113** (2014) no.19, 191302 [arXiv:1406.6053 [astro-ph.SR]].

[Bea98] J. F. Beacom and P. Vogel, “Mass signature of supernova muon-neutrino and tau-neutrino neutrinos in Super-Kamiokande,” Phys. Rev. D **58** (1998) 053010 [hep-ph/9802424].

[Bea03] J. F. Beacom and M. R. Vagins, “GADZOOKS! Antineutrino spectroscopy with large water Cherenkov detectors,” Phys. Rev. Lett. **93** (2004) 171101 [hep-ph/0309300].

[Ber91] J. F. Berger, M. Girod and D. Gogny, "Time-dependent quantum collective dynamics applied to nuclear fission," Comput. Phys. Commun. **63** (1991) 365.

[Cap18] F. Capozzi, E. Lisi, A. Marrone and A. Palazzo, "Current unknowns in the three neutrino framework," arXiv:1804.09678 [hep-ph].

[Cha18] J. H. Chang, R. Essig and S. D. McDermott, "Supernova 1987A Constraints on Sub-GeV Dark Sectors, Millicharged Particles, the QCD Axion, and an Axion-like Particle," arXiv:1803.00993 [hep-ph].

[Co11] G. Co, V. De Donno, M. Anguiano and A. M. Lallena, "Effective tensor forces and neutron rich nuclei," J. Phys. Conf. Ser. **267** (2011) 012022 [arXiv:1009.3364 [nucl-th]].

[Co18] G. Co', M. Anguiano, V. De Donno and A. M. Lallena, "Matter distribution and spin-orbit force in spherical nuclei," Phys. Rev. C **97** (2018) no.3, 034313 [arXiv:1712.05186 [nucl-th]].

[Dea11] A. De Angelis, G. Galanti and M. Roncadelli, "Relevance of axion-like particles for very-high-energy astrophysics," Phys. Rev. D **84**, 105030 (2011) Erratum: [Phys. Rev. D **87**, no. 10, 109903 (2013)] [arXiv:1106.1132 [astro-ph.HE]].

[Dig00] A. S. Dighe and A. Y. Smirnov, "Identifying the neutrino mass spectrum from the neutrino burst from a supernova," Phys. Rev. D **62** (2000) 033007 [hep-ph/9907423].

[Din81] M. Dine, W. Fischler and M. Srednicki, "A Simple Solution to the Strong CP Problem with a Harmless Axion," Phys. Lett. **104B** (1981) 199.

[Ehr10] K. Ehret *et al.*, "New ALPS Results on Hidden-Sector Lightweights," Phys. Lett. B **689** (2010) 149 [arXiv:1004.1313 [hep-ex]].

[Eng90] J. Engel, D. Seckel and A. C. Hayes, "Emission and detectability of hadronic axions from SN1987A," Phys. Rev. Lett. **65** (1990) 960.

[Fis] http://ift.uni.wroc.pl/ fischer/.

[Fis16] T. Fischer, S. Chakraborty, M. Giannotti, A. Mirizzi, A. Payez and A. Ringwald, "Probing axions with the neutrino signal from the next galactic supernova," Phys. Rev. D **94** (2016) no.8, 085012 [arXiv:1605.08780 [astro-ph.HE]].

[Fog04] G. L. Fogli, E. Lisi, A. Mirizzi and D. Montanino, "Probing supernova shock waves and neutrino flavor transitions in next-generation water-Cerenkov detectors," JCAP **0504** (2005) 002 [hep-ph/0412046].

[For13] J. A. Formaggio and G. P. Zeller, "From eV to EeV: Neutrino Cross Sections Across Energy Scales," Rev. Mod. Phys. **84** (2012) 1307 [arXiv:1305.7513 [hep-ex]].

[Gal17] A. Gallo Rosso, F. Vissani and M. C. Volpe, "What can we learn on supernova neutrino spectra with water Cherenkov detectors?," JCAP **1804** (2018) no.04, 040 doi:10.1088/1475-7516/2018/04/040 [arXiv:1712.05584 [hep-ph]].

[Gor09] S. Goriely, S. Hilaire, M. Girod and S. Peru, "First Gogny-Hartree-Fock-Bogoliubov Nuclear Mass Model," Phys. Rev. Lett. **102** (2009) 242501.

[Ike07] M. Ikeda *et al.* [Super-Kamiokande Collaboration], "Search for Supernova Neutrino Bursts at Super-Kamiokande," Astrophys. J. **669** (2007) 519 [arXiv:0706.2283 [astro-ph]].

[Ira11] I. G. Irastorza *et al.*, "Towards a new generation axion helioscope," JCAP **1106** (2011) 013 [arXiv:1103.5334 [hep-ex]].

[Ira18] I. G. Irastorza and J. Redondo, "New experimental approaches in the search for axion-like particles," arXiv:1801.08127 [hep-ph].

[Jeu77] J. P. Jeukenne, A. Lejeune and C. Mahaux, "Optical-model potential in finite nuclei from Reid's hard core interaction," Phys. Rev. C **16** (1977) 80.

[Kak93] M. Kaku, "Quantum Field Theory: A Modern Introduction," Oxford University Press (1993).

[Kei02] M. T. Keil, G. G. Raffelt and H. T. Janka, "Monte Carlo study of supernova neutrino spectra formation," Astrophys. J. **590** (2003) 971 [astro-ph/0208035].

[Kim86] J. E. Kim, "Light Pseudoscalars, Particle Physics and Cosmology," Phys. Rep. **150** (1987) 1.

[Kol92] E. Kolbe, K. Langanke, S. Krewald and F. K. Thielemann, "Inelastic neutrino scattering on C-12 and O-16 above the particle emission threshold," Nucl. Phys. A **540** (1992) 599.

[Lah13] R. Laha and J. F. Beacom, "Gadolinium in water Cherenkov detectors improves detection of supernova ν_e," Phys. Rev. D **89** (2014) 063007 [arXiv:1311.6407 [astro-ph.HE]].

[Lan95] K. Langanke, P. Vogel and E. Kolbe, "Signal for supernova muon-neutrino and tau-neutrino neutrinos in water Cherenkov detectors," Phys. Rev. Lett. **76** (1996) 2629 [nucl-th/9511032].

[Lej80] A. Lejeune, "Low-energy optical model potential in finite nuclei from Reid's hard core interaction," Phys. Rev. C **21** (1980) 1107.

[Lun04] C. Lunardini and A. Y. Smirnov, "Neutrinos from SN1987A: Flavor conversion and interpretation of results," Astropart. Phys. **21** (2004) 703 [hep-ph/0402128].

[Mcf66] L. McFadden and G. R. Satchler, "Optical-model analysis of the scattering of 24.7 MeV alpha particles," Nucl. Phys. **84** (1966) 177.

[Mes67] A. Messiah, "Quantum mechanics" Vol. 1, North-Holland Publishing Company (1967).

[Mir05] A. Mirizzi and G. G. Raffelt, "New analysis of the sn 1987a neutrinos with a flexible spectral shape," Phys. Rev. D **72** (2005) 063001 [astro-ph/0508612].

[Mir16] A. Mirizzi, I. Tamborra, H. T. Janka, N. Saviano, K. Scholberg, R. Bollig, L. Hudepohl and S. Chakraborty, "Supernova Neutrinos: Production, Oscillations and Detection," Riv. Nuovo Cim. **39** (2016) no.1-2, 1 [arXiv:1508.00785 [astro-ph.HE]].

[Pat16] C. Patrignani *et al.* [Particle Data Group], "Review of Particle Physics," Chin. Phys. C **40** (2016) no.10, 100001.

[Pec77a] R. D. Peccei and H. R. Quinn, "CP Conservation in the Presence of Instantons," Phys. Rev. Lett. **38** (1977) 1440.

[Pec77b] R. D. Peccei and H. R. Quinn, "Constraints Imposed by CP Conservation in the Presence of Instantons," Phys. Rev. D **16** (1977) 1791.

[Pec06] R. D. Peccei, "The Strong CP problem and axions," Lect. Notes Phys. **741** (2008) 3.

[Pes95] M. E. Peskin and D. V. Schroeder, "An introduction to Quantum Field Theory," Perseus Book Publishing (1995).

[Raf95] G. Raffelt and D. Seckel, "A selfconsistent approach to neutral current processes in supernova cores," Phys. Rev. D **52** (1995) 1780 [astro-ph/9312019].

[Raf96] G. Raffelt, "Stars as Laboratories for Fundamental Physics," University of Chicago Press (1996).

[Rau00] T. Rauscher and F. K. Thielemann, "Astrophysical reaction rates from statistical model calculations," Atom. Data Nucl. Data Tabl. **75** (2000) 1 [astro-ph/0004059].

[Rau15] Rauscher, T., computer code SMARAGD, version 0.9.3s (2015).

[Sch80] P. Ring and P. Schuck, "The nuclear many-body problem", Springer-Verlag Berlin (1980).

[Sch11] K. Scholberg, "Supernova neutrino detection in water Cherenkov detectors," J. Phys. Conf. Ser. **309** (2011) 012028.

[Shi80] M. A. Shifman, A. I. Vainshtein and V. I. Zakharov, "Can Confinement Ensure Natural CP Invariance of Strong Interactions?," Nucl. Phys. B **166** (1980) 493.

[Sik84] P. Sikivie, "Experimental Tests of the Invisible Axion," Phys. Rev. Lett. **51** (1983) 1415 Erratum: [Phys. Rev. Lett. **52** (1984) 695].

[Str06] A. Strumia and F. Vissani, "Neutrino masses and mixings and...," hep-ph/0606054.

[Tom03] R. Tomas, D. Semikoz, G. G. Raffelt, M. Kachelriess and A. S. Dighe, "Supernova pointing with low-energy and high-energy neutrino detectors," Phys. Rev. D **68** (2003) 093013 [hep-ph/0307050].

[Tur88] M. S. Turner, "Axions from SN 1987a," Phys. Rev. Lett. **60** (1988) 1797.

[Vog01] P. Vogel, "Future galactic supernova neutrino signal: What can we learn?," Prog. Part. Nucl. Phys. **48** (2002) 29 [nucl-th/0111016].

[Wat08] H. Watanabe *et al.* [Super-Kamiokande Collaboration], "First Study of Neutron Tagging with a Water Cherenkov Detector," Astropart. Phys. **31** (2009) 320 [arXiv:0811.0735 [hep-ex]].

[Wei78] S. Weinberg, "A New Light Boson?," Phys. Rev. Lett. **40** (1978) 223.

[Wil78] F. Wilczek, "Problem of Strong p and t Invariance in the Presence of Instantons," Phys. Rev. Lett. **40** (1978) 279.